

UNIVERSITÀ DI ROMA LA SAPIENZA  
DIPARTIMENTO DI SCIENZE DI BASE E APPLICATE  
PER L'INGEGNERIA

TESI DI DOTTORATO

---

# The beam coupling impedance model of CERN Proton Synchrotron

---

*Coordinator:*

Prof. Luigi PALUMBO

*Author:*

Serena PERSICHELLI

*Advisors:*

Prof. Mauro MIGLIORATI

Dr. Benoit SALVANT

Prof. Vittorio VACCARO

Dottorato di Ricerca in Elettromagnetismo e Modelli Matematici per l'Ingegneria  
Ciclo XXVII

April 2015





*C'è chi meglio degli altri realizza la sua vita.  
È tutto in ordine dentro e attorno a lui.  
Per ogni cosa ha metodi e risposte.  
È lesto a indovinare il chi il come il dove  
e a quale scopo.  
Appone il timbro a verità assolute,  
getta i fatti superflui nel tritadocumenti,  
e le persone ignote  
dentro appositi schedari.  
Pensa quel tanto che serve,  
non un attimo in più,  
perché dietro quell'attimo sta in agguato il dubbio.  
E quando è licenziato dalla vita,  
lascia la postazione  
dalla porta prescritta.  
A volte un po' lo invidia  
- per fortuna mi passa.*

Wisława Szymborska



# *Estratto*

## **The beam coupling impedance model of CERN Proton Synchrotron**

by Serena PERSICHELLI

L'attività di ricerca descritta in questo lavoro di tesi riguarda lo sviluppo di un modello di beam coupling impedance per il CERN Proton Synchrotron (PS), nel contesto del progetto LHC Injector Upgrade. I risultati dello studio hanno permesso una migliore comprensione dei limiti di instabilità della macchina, aiutando a prevedere gli effetti dell'aumento di corrente del fascio previsto dal progetto di upgrade di LHC. La conoscenza del modello di impedenza permette inoltre di migliorare la stabilità dei fasci iniettati nella catena di accelerazione dell'LHC, in previsione degli aumenti di energia delle collisioni programmati per gli esperimenti di fisica delle particelle. Per determinare i modelli di beam coupling impedance longitudinali e trasversi del Proton Synchrotron, i dispositivi installati nella macchina, e considerati le più importanti sorgente di impedenza, sono stati individuati e studiati. I dispositivi sono successivamente stati modellizzati con appositi CAD 3D per effettuare simulazioni elettromagnetiche. In alcuni casi è stato inoltre possibile effettuare misure RF su banco, al fine di confrontare l'impedenza simulata con quella misurata. Infine, le impedenze dei vari dispositivi analizzati sono state sommate per ottenere un andamento totale dell'impedenza (longitudinale e trasversale) in funzione della frequenza. Tale andamento rappresenta il modello di impedenza teorico della macchina. Il modello teorico è stato confrontato con le misure, con l'obiettivo di verificarne l'accuratezza rispetto al caso reale. I risultati ottenuti hanno mostrato un buon accordo sia sul piano longitudinale che trasversale, ed hanno permesso di stabilire un preciso budget di impedenza per il PS, raggiungendo così gli obiettivi del progetto di ricerca assegnato. In questo lavoro viene inoltre descritto lo sviluppo di un modello elettromagnetico teorico per la stima dell'impedenza longitudinale generata da un fascio di particelle quando incontra una brusca discontinuità (step) tra due camere a vuoto di sezione ellittica cofocali. L'obiettivo è quello di ottenere un modello da ricondurre al caso reale del PS, nel quale sono presenti un centinaio di transizioni brusche tra camere di sezione circolare ed ellittica. Inoltre è stata sviluppata una nuova espansione della funzione di Green nello spazio libero in coordinate ellittiche.



# Contents

<b>Estratto</b>	<b>iv</b>
<b>Contents</b>	<b>vi</b>
<b>List of Figures</b>	<b>ix</b>
<b>List of Tables</b>	<b>xiii</b>
<b>Introduction</b>	<b>2</b>
<b>I The longitudinal and transverse beam coupling impedance models of the CERN Proton Synchrotron</b>	<b>6</b>
<b>1 Beam coupling impedance in particle accelerators</b>	<b>8</b>
1.1 Beam coupling impedance concept . . . . .	8
1.2 Wakefield and impedance of a resonance . . . . .	12
<b>2 The CERN Proton Synchrotron</b>	<b>16</b>
2.1 Description of the machine . . . . .	17
2.1.1 Kicker magnets and septa . . . . .	18
2.1.2 RF cavities . . . . .	21
2.1.2.1 40 and 80 MHz cavities . . . . .	22
2.1.2.2 10 MHz cavities . . . . .	23
2.1.2.3 200 MHz cavities . . . . .	23
2.1.3 Beam chambers and vacuum instrumentation . . . . .	25
2.1.3.1 The PS beam chamber and its features . . . . .	25
2.1.3.2 Vacuum pumps and valves . . . . .	27
2.1.3.3 Flanges . . . . .	28
2.2 PS as LHC injector: the upgrade program . . . . .	31
2.3 Beams in the CERN PS . . . . .	32
2.3.1 PS beam spectra . . . . .	33
<b>3 The PS transverse impedance model</b>	<b>36</b>
3.1 Tune shift measurements for transverse impedance determination . . . . .	36
3.1.1 Chromaticity . . . . .	38
3.1.2 Control of the working point . . . . .	38
3.2 Tune shift measurements at zero chromaticity . . . . .	39

3.2.1	Injection energy . . . . .	39
3.2.2	Intermediate energies . . . . .	39
3.2.3	Extraction energy . . . . .	41
3.3	Tune shift measurements with chromaticity scan . . . . .	43
3.4	Transverse impedance budget from simulations . . . . .	43
3.4.1	Indirect Space charge and resistive wall . . . . .	44
3.4.2	Kicker magnets . . . . .	45
3.4.3	RF cavities . . . . .	46
3.4.4	Vacuum equipment . . . . .	47
<b>4</b>	<b>The PS longitudinal impedance model</b>	<b>52</b>
4.1	Measurements of quadrupole synchrotron frequency . . . . .	52
4.1.1	Quadrupole synchrotron frequency measurement setup . . . . .	53
4.1.2	Longitudinal impedance from measurements . . . . .	54
4.2	Longitudinal impedance budget from simulations . . . . .	59
4.2.1	Space charge . . . . .	59
4.2.2	Resistive wall . . . . .	59
4.2.3	Kickers . . . . .	60
4.2.4	Vacuum equipment . . . . .	60
4.2.5	RF cavities . . . . .	62
<b>5</b>	<b>Impedance studies of machine elements installed during LS1</b>	<b>66</b>
5.1	Dummy septum . . . . .	66
5.1.1	Introduction and context . . . . .	66
5.1.2	Dummy septum design . . . . .	67
5.1.3	Impedance aspects . . . . .	68
5.1.4	Impedance simulations . . . . .	69
5.1.5	Coupled bunch instability evaluation . . . . .	71
5.1.6	Contribution to the total Proton Synchrotron Impedance budget . . . . .	73
5.1.7	Mode damping proposals . . . . .	73
5.1.8	RF impedance measurements . . . . .	75
5.2	Finemet loaded longitudinal damper . . . . .	77
5.2.1	Introduction . . . . .	77
5.2.2	Longitudinal impedance calculation . . . . .	78
5.2.2.1	Connection Lines Effect on the Impedance . . . . .	81
5.2.3	Transverse impedance calculation . . . . .	82
5.3	Tune Stripline Beam Position Monitor . . . . .	83
5.3.1	Introduction . . . . .	83
5.3.2	Impedance calculation . . . . .	84
5.4	Conclusions . . . . .	86
<b>II</b>	<b>Electromagnetic field and beam coupling impedance of elliptical beam chambers and step transitions in particle accelerators</b>	<b>88</b>
<b>6</b>	<b>Green functions in elliptical vacuum chambers</b>	<b>90</b>
6.1	Theory and applications of Mathieu functions . . . . .	91
6.1.1	The wave equation in elliptical coordinates . . . . .	91

---

6.1.2	Solution of the Mathieu equations . . . . .	94
6.1.3	Calculation of eigenfrequencies . . . . .	97
6.2	Primary fields in elliptical coordinates . . . . .	100
6.2.1	Direct field (primary field) . . . . .	101
6.2.2	Indirect field (Scattered field) . . . . .	104
6.2.3	Total field in elliptic coordinates . . . . .	106
<b>7</b>	<b>Beam coupling impedance of elliptical-elliptical step transitions</b>	<b>110</b>
7.1	Fields and impedance of a circular step transition . . . . .	110
7.2	Tapers . . . . .	113
7.3	Simulations with realistic dimensions of the PS pipe . . . . .	115
7.4	Analytical determination of the impedance of a step transitions between two elliptical beam tubes . . . . .	116
7.4.1	Representation of the fields . . . . .	117
7.4.2	Equation 1 (electric field): projection with TM modes . . . . .	119
7.4.3	Equation 2 (electric field): projection with TE modes . . . . .	121
7.4.4	Equation 3 (magnetic field): projection with TM modes . . . . .	123
7.4.5	Equation 4 (magnetic field): projection with TE modes . . . . .	125
7.5	Known coefficients of the system . . . . .	126
7.5.1	Equation 1 (electric field) . . . . .	126
7.5.2	Equation 2 (electric field) . . . . .	127
7.5.3	Equation 3 (magnetic field) . . . . .	127
7.5.4	Equation 4 (magnetic field) . . . . .	128
7.5.5	Mode Matching system summary . . . . .	128
7.6	Longitudinal coupling impedance calculation . . . . .	130
	<b>Conclusions</b>	<b>131</b>
	<b>A Simil-Green formula</b>	<b>136</b>
	<b>B Primary field components</b>	<b>138</b>
	<b>C Scattered field components</b>	<b>140</b>
	<b>Acknowledgements</b>	<b>142</b>

# List of Figures

1.1	Flow chart of the beam coupling impedance concept. . . . .	9
1.2	Scheme of source (S) and test (T) particle for impedance calculation. . . .	10
1.3	A parallel RLC circuit schematic. . . . .	12
2.1	Proton Synchrotron complex layout. . . . .	17
2.2	Design of kickers KFA28 (left) and KFA13 (right). KFA28 is designed with frame shape ferrite and an aluminium insert; KFA13 is designed C-shape ferrite with longitudinal segmentation. . . . .	19
2.3	Magnetic septum SMH16. . . . .	20
2.4	Design of the 40 MHz (right) and 80 MHz (left) cavities for simulations. . .	22
2.5	Design of the 10 MHz cavity for simulations. . . . .	24
2.6	Model of the 200 MHz cavities for simulations. . . . .	25
2.7	200 MHz cavity tuners (left) a the magnetic coupler for the fundamental mode (right). . . . .	25
2.8	Mechanical drawings of two more common PS vacuum chambers. CDD reference: PS VCS0024, STDVFCON0063. . . . .	26
2.9	Mechanical models horizontal misaligned 43 of section: front view (left) and upper view (right). CDD reference: PS VCBCG0001. . . . .	26
2.10	3D model of the horizontally misaligned PS SS60 where are installed three flanges, a VVS and a bellow. . . . .	27
2.11	Horizontal and vertical physical apertures of the PS vacuum chamber. . .	27
2.12	Sketch of two vacuum pump connections with the beam pipe. . . . .	28
2.13	Picture of a PS sector valve. . . . .	28
2.14	3D model for simulations of a SPS 273 flange installed in the PS. . . . .	29
2.15	Flange disk with ceramic layer (left); one of the isolated PS flange provided by RF bypass installed in the ring (right). . . . .	30
2.16	Mechanical models of the PS type collar (left) and SPS type collar (right). CDD references: 8095.0277.1B . . . . .	30
2.17	Single bunch LHC INDIV spectrum measured at C171 (flat top), $6 \cdot 10^{10}$ ppb, $4\sigma = 80$ ns. . . . .	33
2.18	Single bunch LHC INDIV spectrum measured at C432 (transition), $6 \cdot 10^{10}$ ppb. . . . .	33
2.19	Single bunch LHC INDIV spectrum measured at C1254 (6 ms before extraction), $6 \cdot 10^{10}$ ppb. . . . .	33
2.20	Single bunch TOF spectrum measured at C300 (flat top), $94 \cdot 10^{10}$ ppb, $4\sigma = 90$ ns. . . . .	33
2.21	Multi bunch LHC50 spectrum measured at C198 (after first injection), intensity $6.7 \cdot 10^{12}$ ppb, 6 bunches in $h = 7$ . . . . .	34

2.22	Multi bunch LHC50 spectrum measured at C1398 (after second injection), intensity $6.7 \cdot 10^{12}$ ppb, 6 bunches in $h = 7$ .	34
2.23	Multi bunch LHC50 spectrum measured at C1505 (end of flat bottom), intensity $6.7 \cdot 10^{12}$ ppb, 18 bunches in $h = 21$ .	34
2.24	Multi bunch LHC50 spectrum measured at C1625 (5 ms before transition), intensity $6.7 \cdot 10^{12}$ ppb, 18 bunches in $h = 21$ .	34
2.25	Multi bunch LHC50 spectrum measured at C2205 (flat bottom), intensity $6.7 \cdot 10^{12}$ ppb, 18 bunches in $h = 21$ .	34
2.26	Multi bunch LHC50 spectrum measured at C2454 (6 ms before extraction), intensity $6.7 \cdot 10^{12}$ ppb, 36 bunches in $h = 48$ .	34
3.1	Magnetic field applied along the cycle used for tune shift measurements at 2 GeV.	40
3.2	Vertical tune shift as a function of beam intensity measured at 2 GeV.	40
3.3	Vertical tune shift as a function of beam intensity measured at 7.25 GeV.	41
3.4	Vertical tune shift as a function of beam intensity measured at 13.09 GeV.	41
3.5	Magnetic field applied along the cycle used for tune shift measurements at 25 GeV.	42
3.6	Vertical tune shift as a function of beam intensity measured at 25.48 GeV.	42
3.7	Imaginary part of the effective vertical impedance scan with chromatic frequency at different energies.	44
3.8	Total vertical impedance of the PS space charge and resistive wall calculated at 2 GeV for the round chamber case.	45
3.9	Total horizontal impedance of the PS kickers simulated with CST Particle Studio.	46
3.10	Total vertical impedance of the PS kickers simulated with CST Particle Studio.	46
3.11	Imaginary part of the vertical impedance for the 10, 40 and 80 MHz cavities simulated with CST Particle Studio (CST output convention is negative for positive transverse impedances).	47
3.12	Imaginary part of the vertical impedance of bellows (273 elements), vacuum pumps (100 elements) and sector valves (10 elements) simulated with CST Particle Studio.	48
3.13	Imaginary part of the vertical impedance of PS metallic not isolated flanges simulated with CST Particle Studio.	48
3.14	Horizontal and vertical dipolar and quadrupolar components of the PS wake function.	50
3.15	Horizontal and vertical dipolar and quadrupolar components of the PS impedance model.	50
4.1	Longitudinal quadrupole beam transfer function (BTF) measurement setup.	53
4.2	Amplitude and phase of the quadrupole BTF for a bunch of $9 \cdot 10^{10}$ particles kept by 95 kV at 40 MHz.	54
4.3	Quadrupole frequency shift and linear fit with Gaussian distribution function for the first set of measurements.	57
4.4	Quadrupole frequency shift and linear fit with Gaussian distribution function for the second set of measurements.	57
4.5	Quadrupole frequency shift and linear fit with parabolic line density for the first set of measurements.	58

4.6	Quadrupole frequency shift and linear fit with parabolic line density for the second set of measurements. . . . .	58
4.7	Resistive wall impedance for the PS vacuum chamber. . . . .	60
4.8	Total longitudinal impedance of the PS kickers. . . . .	60
4.9	Real part of longitudinal impedance of a vacuum pump. . . . .	61
4.10	Imaginary part of longitudinal impedance of a vacuum pump. . . . .	61
4.11	Real part of longitudinal impedance of a bellow. . . . .	61
4.12	Imaginary part of longitudinal impedance of a bellow. . . . .	61
4.13	Real part of longitudinal impedance of a step transition. . . . .	61
4.14	Imaginary part of longitudinal impedance of a step transition. . . . .	61
4.15	Amplitude of $S_{12}$ of the fundamental mode of the 200 Mhz cavity with reversed diodes measured with VNA. . . . .	63
4.16	Amplitude of $S_{12}$ of the fundamental mode of the 200 Mhz cavity with short circuited diodes measured with VNA. . . . .	63
4.17	Longitudinal wake potential of a 2.3 ns Gaussian bunch given by the total simulated impedance budget. . . . .	64
5.1	Dummy septum simplified model used for CST simulations (left) and dummy septum mechanical model with blade in nominal position with respect to the orbiting beam (right). . . . .	67
5.2	Dummy septum tank and motor allocation. . . . .	68
5.3	Inside view with BTV, blade and screen installed. . . . .	68
5.4	Inside view with blade and support table installed. . . . .	68
5.5	Beam Screen before with sliding fingers before installation. . . . .	68
5.6	Longitudinal beam coupling impedance at extraction evaluated with CST Particle Studio 2012. . . . .	70
5.7	Longitudinal coupling impedance at extraction evaluated with CST Particle Studio after the insertion of sliding contacts between the screen and the support table. . . . .	74
5.8	Comparison between longitudinal impedance evaluated with CST Particle Studio with and without ferrite. . . . .	75
5.9	Magnetic field lines on a transversal cut in the dummy septum with the ferrite block insertion. . . . .	75
5.10	Measurement setup for dummy septum impedance measurements. On the left, a suco box connected to the septum flange and welded to the stretched wire through a matching resistor; on the right, the flange with three holes to allow different position for the wire. . . . .	76
5.11	The $S_{21}$ transmission coefficient measured for three positions of the wire respect to the extraction blade. . . . .	77
5.12	The $S_{21}$ transmission coefficient measured at extraction compared with CST Microwave Studio simulation in frequency domain. . . . .	77
5.13	CST model of the one cell prototype of the Finemet® loaded longitudinal damper. . . . .	79
5.14	Comparison between Finemet® measured and fitted dispersive parameters $\mu_1$ and $\mu_2$ . . . . .	79
5.15	Longitudinal impedance of the single cell damper. . . . .	80
5.16	CST model of the six cells Finemet® loaded longitudinal damper. . . . .	80
5.17	Longitudinal impedance of the six cells damper. . . . .	81

5.18	Measured longitudinal impedance of the single cell as seen by the beam when going through one gap connected to the amplifiers with 4 ns cables.	81
5.19	Comparison between the dipolar impedance of the longitudinal damper and the sum of the horizontal impedances of the PS kickers.	82
5.20	Longitudinal damper after installation in SS01 of the PS ring.	83
5.21	3D model of the stripline beam position monitor used for implemented in CST Microwave Studio.	84
5.22	Pickup before installation.	84
5.23	Longitudinal coupling impedance of the stripline beam position monitor calculated with CST Particle Studio.	85
5.24	Transverse coupling impedance of the stripline beam position monitor calculated with CST Particle Studio.	86
6.1	Elliptic Cylindrical Coordinates. The $\varphi$ coordinates are the asymptotic angle of confocal hyperbolic cylinders symmetrical about the x-axis. The $\mu$ coordinates are confocal elliptic cylinders centered on the origin.	92
6.2	Angular and radial even Mathieu functions and their derivative calculated for the mode $TM_{01}^e$ for the main beam chamber of the PS.	98
6.3	Angular and radial odd Mathieu functions and their derivative calculated for the odd mode $TE_{11}^s$ for the main beam chamber of the PS.	98
6.4	Perspective view (right) and contour plot (left) of a bouncing ball mode $TM_{0,4}^e$ .	99
6.5	Perspective view (right) and contour plot (left) of a whispering gallery mode $TM_{12,1}^e$ .	99
6.6	Green functions (direct component of the source field) in free space calculated with Eq. 6.43 (black line) Eq. 6.64 (red line).	105
6.7	PS parameters dependency of the primary field calculated in function of the elliptical coordinate $\varphi$ for a given value of $\mu_0$ .	108
7.1	Step-out discontinuity in a beam pipe.	110
7.2	Longitudinal coupling impedance for a 1 cm length Gaussian bunch passing into a step-in transition calculated with CST Particle Studio.	112
7.3	Longitudinal coupling impedance for a 1 cm length Gaussian bunch passing into a step-out transition calculated with CST Particle Studio.	112
7.4	Symmetric step discontinuity in a beam pipe.	113
7.5	Longitudinal beam coupling impedance of a symmetric step discontinuity.	113
7.6	Step in discontinuity with a gradual smooth taper.	114
7.7	Longitudinal beam coupling impedance of 10 cm length tapered transition between two circular tubes of radius a=2 cm and b=4 cm, excited by a bunch of $\sigma=1$ cm.	115
7.8	Longitudinal beam coupling impedance of a step transition between an elliptic beam pipe (major semi-axis 7.3 cm, minor semi-axis 3.5 cm) of and a circular beam pipe (radius=10 cm).	116
7.9	Step-out transition system between two elliptical waveguides.	117

# List of Tables

2.1	Main parameters of the PS machine for the 25 ns bunch spacing. . . . .	18
2.2	Geometry of PS kickers. . . . .	20
2.3	Values of unloaded Q and shunt impedance designed for the different work conditions of the single 200 MHz cavity. . . . .	25
3.1	Beam parameters for tune shift measurements at kinetic energy of 2 GeV. . . . .	40
3.2	Beam parameters for tune shift measurements at kinetic energy of 7.25 GeV. . . . .	41
3.3	Beam parameters for tune shift measurements at kinetic energy of 13.09 GeV. . . . .	41
3.4	Beam parameters for tune shift measurements at kinetic energy of 25.48 GeV. . . . .	42
3.5	Imaginary part of the vertical effective impedance measured at different energies at zero chromaticity. . . . .	43
3.6	Indirect space charge and resistive wall contributions to the total vertical effective impedance at different kinetic energies for round chamber and parallel plates. . . . .	45
3.7	Effective horizontal and vertical impedances calculated for vacuum equipment. . . . .	48
3.8	Contribution to the vertical effective impedance budget measured at 2 GeV of the machine elements. . . . .	49
4.1	RF cavities fundamental mode resonance parameters. . . . .	62
4.2	Contributions of the machine elements included in the longitudinal coupling impedance budget. . . . .	64
5.1	Main parameters of CST Particle Studio simulations for the longitudinal coupling impedance simulation. . . . .	70
5.2	Resonant parameters of the first ten eigenmodes. . . . .	71
5.3	PS-LIU parameters (25 ns bunch spacing) considered for coupled bunch calculations. . . . .	72
5.4	Coupled bunch instability growth rates evaluated for different beam position inside the septum. . . . .	72
5.5	Main parameters of CST Particle Studio simulations for the single cell damper. . . . .	79
5.6	Main parameters of CST Particle Studio simulations for the six cells Finemet® loaded longitudinal damper. . . . .	80
5.7	Main parameters of CST Particle Studio transverse simulations for the six cells longitudinal damper. . . . .	82
5.8	Main parameters of CST Particle Studio simulations for the longitudinal impedance simulation of the beam position monitor. . . . .	85

---

7.1	Comparison between loss factors $k$ in the step-in and step-out case for different bunch lengths $\sigma_b$ (values calculated with CST Particle Studio). . . . .	111
7.2	Loss factors $k$ of a structure with two symmetric step transitions calculated with different bunch lengths $\sigma_b$ with CST Particle Studio. . . . .	113
7.3	Comparison between loss factors $k$ expressed in V/pC for a bunch with different lengths $\sigma_b$ passing by an abrupt discontinuity or a smooth one (values calculated with CST Particle Studio). . . . .	114



# Introduction

The research activity described in this thesis work is mainly dedicated to developing a longitudinal and a transverse beam coupling impedance model for the CERN Proton Synchrotron (PS), in the framework of the Large Hadron Collider (LHC) Injector Upgrade (LIU) project. The study allows a better understanding of the instability threshold of the machine, helping predicting the effects of the current increase planned for the upgrade program. Furthermore, the knowledge of the machine beam coupling impedance model allows improving the stability of beams injected into the LHC chain, in prevision for the particle collision energy increase in program for LHC physics experiments.

In order to build the beam coupling impedance models of the Proton Synchrotron, several accelerator devices installed in the machine, and considered as significant sources of impedance, have been identified and studied. The devices have been modeled with 3D Computer-Aided Design (CAD) software in order to perform electromagnetic simulations. In some cases, RF bench measurements have also been performed, in order to cross-check the result from simulations. Finally, the impedances of the devices have been summed together, obtaining a total impedance (longitudinal and transverse) as a function of the frequency, describing the theoretical impedance model (longitudinal and transverse) of the machine. The theoretical model has been compared with beam based measurements. Experimental results show a good agreement both on the longitudinal and transverse plane, allowing to establish a precise impedance budget for the PS.

The second part of this thesis work is focused on the development of a novel elliptical coordinates expansion of the electromagnetic field produced by the interaction of a particle beam traveling inside a tube of elliptical cross section. In order to match the elliptical coordinates system, we needed to introduce a set of functions, called *Mathieu functions*. A novel analytical formula (based on of the mode matching theory) for the evaluation of the longitudinal beam coupling impedance of a step transition between two semi-infinite elliptical waveguides, has also been developed.

## **Electromagnetic simulations**

Several devices have been simulated in order to estimate the beam coupling impedance produced by the interaction between particle beams and vacuum chambers in circular accelerator machines. The beam coupling impedance is defined as the Fourier transform of the wake field produced by the interaction of a charge with the surrounding environment. When possible, the simulated impedance has been compared with theoretical models available in literature. The examined devices include eleven injection and extraction kicker magnets with different geometries and several types of RF cavities and mechanical components of the beam chamber (vacuum pumps and valves, flanges, bellows). All devices have been checked during dedicated machine surveys; lately, mechanical models on paper, when available, have been retrieved in order to help the building of a 3D model for simulations.

During the LHC complex Long Shutdown (LS1) and the previous months, some new machine devices to be installed at the beginning of 2014 have been studied. The aim of these studies was to assess the impact of the new elements on the impedance budget. Several months have been dedicated to the study of the impedance of a new dummy extraction septum. The mechanical design stages have been followed up. The insertion of sliding contacts for high order modes damping has been proposed and accepted in the final design of the installed device. Bench measurements took place in order to test the performance of the sliding contacts before installation. The dummy septum is currently working in the machine under nominal operation beam conditions, without impedance or heating related issues.

Impedance studies have been carried out for the new longitudinal damper loaded with Finemet®, a dispersive material for high order modes damping. Also in this case, the simulated impedance has been compared with the results of bench measurements, showing a good agreement and no major issues foreseen from the impedance point of view. The damper is currently installed in the machine, where one of the cells has been connected to the amplifier for tests. At last, the impedance of the new PS stripline pickup has been studied. The device is currently installed and has been used for the tune shift measurements described in the thesis.

## **Beam based measurements**

To estimate the longitudinal impedance of the PS, two beam based measurement campaigns have been carried out at the beginning of 2012. Measurements consist in acquiring an observable called incoherent quadrupolar synchrotron frequency shift. Such a parameter is proportional to the imaginary part of the longitudinal effective impedance through a constant that depends on machine characteristics. The two measurement campaigns

highlighted that the measured longitudinal impedance exhibits a 90% agreement with respect to the longitudinal impedance calculated with theoretical simulations.

In order to measure the imaginary part of the transverse effective impedance of the machine, two campaigns took place in 2012-2013 (before the LHC complex Long Shutdown) and in 2014 (after the LHC complex Long Shutdown). The first campaign allowed a preliminary knowledge of the transverse impedance, showing a 65% agreement with the theoretical model. The second measurement campaign was mainly focused on the investigation of the dependency of the impedance model on a machine parameter called chromaticity. On the longitudinal plane measurements were performed only for extraction energy, whereas on the transverse plane, measurements were repeated for injection, extraction and two intermediate energies.

Finally, measurements of the PS beam spectrum and shape have been performed with RF instrumentation, both for the single and the multi bunch case. This campaign aimed at obtaining a reference for impedance resonance modes of the machine devices, considered potentially harmful. Therefore, resonances falling inside the beam spectrum (that can be sources of heating and power loss) can be identified.

### **Green function in elliptical coordinates and the mode matching technique**

During the PS impedance studies, difficulties in the calculation of the beam coupling impedance of a step transition between two elliptical waveguides of different cross-section, have been encountered. This particular structure encounters some problems when simulated with 3D software, and theoretical methods were not available to solve this specific problem. Due to the high number (about one hundred) of step transitions between circular and elliptical vacuum pipes currently present in the PS, a theoretical model based on the mode matching technique was developed.

Before approaching this problem, we developed a novel expansion in elliptical coordinates of the field generated by a particle beam traveling in the center of an elliptical chamber. The solution, expressed in separate function of elliptical variables, has been calculated separating the contribution of the Green function in free space (direct field) and the field scattered by the charge on the elliptical boundary (indirect field). The Green function expressed in elliptical coordinates matches the analogous solution in circular coordinates available in literature, and is rapidly convergent thanks to the chosen expansion of the Mathieu functions. The field generated by the step transition between two elliptical waveguides, can be calculated superimposing the field of the charge previously expanded in elliptical coordinates, and the radiated field from the discontinuity. Expressing the radiated field as the product of a modal function for a modal coefficient, and imposing the condition of continuity of the tangential electric and magnetic fields at the interface,

we obtain a set of linear equations for the unknown modal coefficients. Because of the functional form of the modal modes, the problem reduces determining a set of modal amplitudes associated with the field expansions in the two regions, where the beam field represents the known coefficients of the system. The solution of this *matching system* allows to calculate the amplitude of the radiated electric field. The longitudinal impedance consists in the Fourier transform of the field itself. The matching system has been implemented in Matlab, even if a library of elliptical Mathieu functions is not available. In addition, the study of the solutions of Mathieu equations, the eigenvalue problem and the implementation in Matlab of the elliptical functions have been performed.

## Part I

# The longitudinal and transverse beam coupling impedance models of the CERN Proton Synchrotron



# Chapter 1

## Beam coupling impedance in particle accelerators

### 1.1 Beam coupling impedance concept

In order to understand the main goal of this thesis work, we need to introduce a common problem for all the accelerators, that is the beam instability generated by unwanted physical phenomena, limiting the beam current and the luminosity of the collisions. Instabilities act negatively on the operation and performance of machines, causing the loss of part or the totality of the beam and compromising the success of experiments and collisions.

One of the main cause of beam instability is the electromagnetic interaction between the particle beam and the external environment, represented by the vacuum chamber. The study of this phenomena leads to the introduction of a new concept, that is the *beam coupling impedance* in particle accelerators [1] [2] [3]. This concept allows for useful stability predictions that lead to correctly design the machine parameters and improve performances.

To approach the concept of beam coupling impedance, let us consider the loop diagram in Fig. 1.1. An external noise field represents a forcing term that enters into the beam dynamic equation (region 1): the noise field can modulate an unperturbed particle beam, producing a variation in the beam current. This perturbation in the beam can be considered a further source of electromagnetic fields (region 2): perturbation represents a new forcing term entering the equation of beam dynamic, and creates a new disturbance in the current which is added to the first one. This may create a loop process that can lead to degradation or loss of the beam, unless a stabilization mechanism intervenes. The

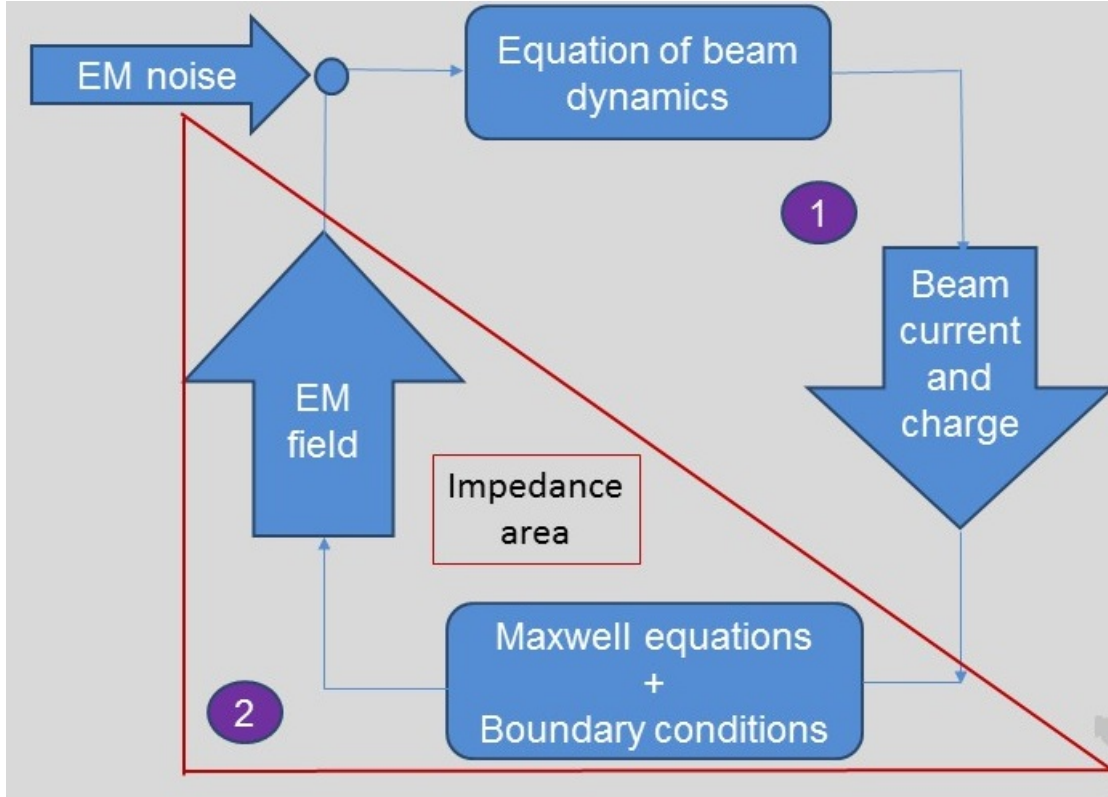


FIGURE 1.1: Flow chart of the beam coupling impedance concept.

beam coupling impedance can be defined as the transfer function between a possible perturbation in the beam current and the electromagnetic field produced by the interaction between the beam itself and the accelerator devices. It is calculated as the integral of the perturbed electric field along the orbit of the beam, divided by the value of the perturbing current:

$$Z_L = \int_0^{2\pi R} \frac{\mathbf{E}_p \cdot d\mathbf{l}}{I_p}. \quad (1.1)$$

Observing region 1 in Fig. 1.1, we understand that, in order to preserve the stability of the beam, the longitudinal beam coupling impedance must satisfy the following relationship

$$Z_L < K \frac{\Delta_p^2}{I_0}, \quad (1.2)$$

where  $\Delta_p$  is the pulse dispersion of the beam,  $I_0$  is the current of the beam and  $K$  is a known constant that depends on the parameters of the accelerator. Experiments and collisions in modern circular machines require high collimated beams (small  $\Delta_p$ ) and high intensities (high  $I_0$ ): for this reason the beam coupling impedance budget of any new machine must be considered during preliminary studies. In particular, when designing a new machine or when the installation of a new device on an existing machine is needed, one should carefully evaluate its contribution to the beam coupling impedance of the machine. For

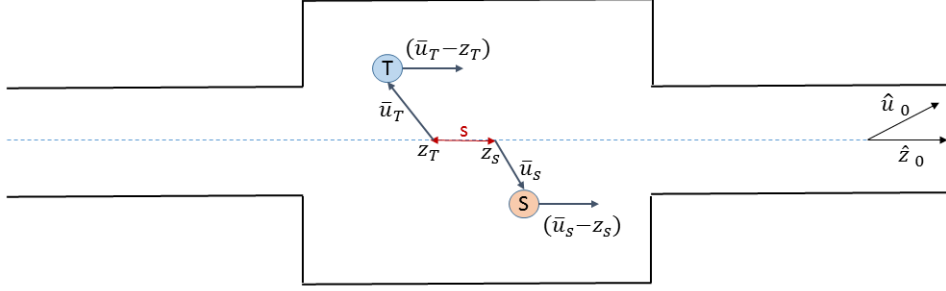


FIGURE 1.2: Scheme of source (S) and test (T) particle for impedance calculation.

a better understanding of the beam coupling impedance concept, let us consider a beam circulating inside an accelerator device as shown in Fig. 1.2. The interaction between the beam and the surrounding environment can be represented by the superposition of two terms: the external fields  $E^{ext}$  and  $H^{ext}$  generated, for instance, by the RF cavities, and the induced (or wake) fields  $E^{wake}$  and  $H^{wake}$ , generated by the interaction of the beam with the vacuum chamber. Figure 1.2 shows a source particle (S) and a test particle (T) that are traveling along the axis of a beam chamber, crossing a discontinuity inside the chamber itself. The source particle excites an electromagnetic field that acts back on the test particle. To describe the problem, we can adopt a cylindrical coordinate system, where  $\hat{u} = u\hat{u}_0$  is the transverse coordinate and  $\hat{z} = z\hat{z}_0$  is the longitudinal coordinate. The test particle is positioned in  $(\hat{u}_T, z_T)$ , and is following at a distance  $s$  the source particle in position  $(\hat{u}_S, z_S = \beta ct)$ , where  $\beta$  is the relativistic factor and  $c$  the speed of light. To have an information about the scattered field impact on longitudinal and transverse dynamics, we can calculate the change in transverse and longitudinal momentum of the test particle, if the velocity of the source and the test particle is constant along the device. The change of momentum is given by [4]:

$$\Delta \bar{p}(\bar{u}_S, \bar{u}_T, s) = \int_{-\infty}^{+\infty} \bar{F}(\bar{u}_S, \bar{u}_T, z_T = z_S - s, z_S) dt, \quad (1.3)$$

where  $\bar{F} = q(\bar{E} + \beta\mu_0 c \hat{z}_0 \times \bar{H})$  is the Lorentz force,  $\mu_0$  the vacuum permeability and  $q$  the particle charge. The projection components of the momentum variation in the longitudinal and transverse plane are given by

$$\Delta p_l(\bar{u}_S, \bar{u}_T, s) = \int_{-\infty}^{+\infty} E_l(\bar{u}_S, \bar{u}_T, z_T) dt \quad (1.4)$$

and

$$\Delta p_t(\bar{u}_S, \bar{u}_T, s) = q \int_{-\infty}^{+\infty} \hat{u}_0 \cdot E_t(\bar{u}_S, \bar{u}_T, z_T, z_S) + \mu_0 \beta \hat{z}_0 \times H_t(\bar{u}_S, \bar{u}_T, z_T, z_S) dt, \quad (1.5)$$

where  $z_S = \beta ct$  and  $z_T = z_S - s$ . Finally, we can define the longitudinal wake function as

$$W_l(\bar{u}_S, \bar{u}_T, s) = -\frac{\beta c}{qQ} \Delta p_l(\bar{u}_S, \bar{u}_T, s), \quad (1.6)$$

and the transverse wake function as

$$W_t(\bar{u}_S, \bar{u}_T, s) = -\frac{\beta c}{qQ} \Delta p_t(\bar{u}_S, \bar{u}_T, s), \quad (1.7)$$

where  $q$  is the charge of the test particle and  $Q$  is the charge of the source particle. Equations 1.6 and 1.7 represent the Green function response to a beam impulse excitation, and they are usually referred as *wakefields*.

If we consider the effects of wakefields on the longitudinal beam motion, we could neglect, as first order approximation, the transverse test and source positions, and consider particles aligned on the closed orbit, i.e.  $\bar{u}_S = 0$  and  $\bar{u}_T = 0$ . Expanding the transverse wakefield along test and source transverse position, we observe the effect of wakefields on the transverse beam motion [4]:

$$W_t(\bar{u}_S, \bar{u}_T, s) \approx W_t(\bar{0}, \bar{0}, s) + \Delta_t W_t(\bar{0}, \bar{u}_T, s) \bar{u}_S + \Delta_t W_t(\bar{u}_S, \bar{0}, s) \bar{u}_T. \quad (1.8)$$

The first term of the expansion is zero when the wakefield integration path corresponds to the geometrical symmetry axis of the device, which happens for axi-symmetric structures. The second term is called *driving* (or dipolar) wakefield, since the test particle is driven by the source particle displacement and feels a transverse force independently from its position. The third term is called *detuning* (or quadrupolar) wakefield, since the test particle feels a transverse detuning force linearly proportional to its displacement. Finally, the beam coupling longitudinal and transverse impedance is defined as the Fourier transform of the longitudinal and transverse wakefield, respectively:

$$Z_l(\bar{u}_S, \bar{u}_T, \omega) = \int_{-\infty}^{+\infty} W_l(\bar{u}_S, \bar{u}_T, s) e^{\frac{j\omega s}{\beta c}} \frac{ds}{\beta c} \quad (1.9)$$

$$Z_t(\bar{u}_S, \bar{u}_T, \omega) = -j \int_{-\infty}^{+\infty} W_t(\bar{u}_S, \bar{u}_T, s) e^{\frac{j\omega s}{\beta c}} \frac{ds}{\beta c}. \quad (1.10)$$

The longitudinal and transverse wakefields can be also be expressed in term of the impedance, as follow:

$$Z_l(\bar{u}_S, \bar{u}_T, s) = \frac{1}{2\pi} \int_{-\infty}^{+\infty} W_l(\bar{u}_S, \bar{u}_T, s) e^{\frac{-j\omega s}{\beta c}} d\omega \quad (1.11)$$

$$Z_t(\bar{u}_S, \bar{u}_T, s) = \frac{j}{2\pi} \int_{-\infty}^{+\infty} W_t(\bar{u}_S, \bar{u}_T, s) e^{\frac{-j\omega s}{\beta c}} d\omega. \quad (1.12)$$

The choice of using the wakefield concept instead of the beam coupling impedance, can be more suitable depending on the case under study.

## 1.2 Wakefield and impedance of a resonance

Accelerator devices like cavities, collimators, beam instrumentation etc., may support the excitation of parasitic or trapped modes. These modes generate resonances that can be described as parallel RLC circuits. An example of such a circuit is shown in Fig. 1.3, where  $I$  the beam current,  $R$  is the shunt impedance,  $C$  is the capacitance and  $L$  is the inductance. Such a system can be represented by the following homogeneous differential

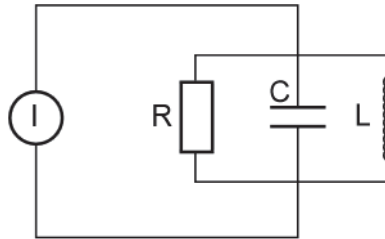


FIGURE 1.3: A parallel RLC circuit schematic.

equation [5]

$$\ddot{V} + \frac{\omega_r}{Q} \dot{V} + \omega_r^2 V = \frac{\omega_r R_s}{Q} \dot{I}, \quad (1.13)$$

where  $\omega_r$  is the angular frequency of the resonance and  $Q$  is the quality factor. The solution of the above equation is a damped oscillation

$$V(t) = e^{-\alpha t} \left[ A \cos \left( \omega_r \sqrt{1 - \frac{1}{4Q^2}} t \right) + B \sin \left( \omega_r \sqrt{1 - \frac{1}{4Q^2}} t \right) \right], \quad (1.14)$$

where  $\alpha$  is the damping rate and  $A$  and  $B$  are the amplitudes of the oscillation. We can now calculate the response of a resonance, modelled as a RLC circuit, to an impulsive

current  $I(t) = q\delta(t)$ . The charge  $q$  induces the following voltage on the capacitor

$$V(0^+) = \frac{\omega_r R_s}{Q} q, \quad (1.15)$$

resulting in energy stored in the capacitor, which must be equal to the energy lost by the charge. This energy is given by

$$U = \frac{1}{2} V(0^+) q = kq^2. \quad (1.16)$$

We introduce the parasitic mode *loss factor*  $k$  that represents the energy loss normalized by the point charge  $q$ , and is given by (electric convention)

$$k = \frac{\omega_r R_s}{2Q}. \quad (1.17)$$

After imposing starting conditions, we obtain that the voltage in the resonant circuit, excited in  $t = 0$  by an impulsive current, becomes

$$V(t) = 2qke^{-\alpha t} \left( \cos \left( \omega_r \sqrt{1 - \frac{1}{4Q^2}} t \right) - \frac{\sin \left( \omega_r \sqrt{1 - \frac{1}{4Q^2}} t \right)}{2Q \sqrt{1 - \frac{1}{4Q^2}}} \right). \quad (1.18)$$

This voltage induced by the source charge, is seen by the test charge  $q'$ , passing in the cavity at the time  $t$  and gaining or losing the energy  $U = q'V(t)$ . This energy, divided by the two charges, is the wake potential of a point charge, and it is approximated by

$$w(t) = 2ke^{-\alpha t} \left( \cos \left( \omega_r \sqrt{1 - \frac{1}{4Q^2}} t \right) - \frac{\sin \left( \omega_r \sqrt{1 - \frac{1}{4Q^2}} t \right)}{2Q \sqrt{1 - \frac{1}{4Q^2}}} \right). \quad (1.19)$$

When  $Q \gg 1$  (high quality resonance), the wake potential is simply given by

$$w(t) \approx 2ke^{-\alpha t} \cos(\omega_r t). \quad (1.20)$$

In order to compute the coupling impedance of a resonance, we consider now an harmonic excitation  $I = \hat{I} \cos(\omega t)$ , which is described by the following differential equation:

$$\ddot{V} + \frac{\omega_r}{Q} \dot{V} + \omega_r^2 V = -\frac{\omega_r R_s}{Q} \hat{I} \omega \sin(\omega t). \quad (1.21)$$

The solution is given by

$$V(t) = \hat{I} R_s \frac{\cos(\omega t) - Q \frac{\omega_r^2 - \omega^2}{\omega_r \omega} \sin(\omega t)}{1 - Q^2 \left( \frac{\omega_r^2 - \omega^2}{\omega_r \omega} \right)^2}. \quad (1.22)$$

The cosine term (in phase with the current and has the meaning of an energy gain) is called *resistive*, while the sine term (out of phase with respect to the current and has the meaning of an energy loss) is called *reactive*. The coupling impedance of the resonance is calculated as the ratio between the voltage and the current, and has a resistive part given by

$$Z_r(\omega) = R_s \frac{1}{1 + Q^2 \left( \frac{\omega_r^2 - \omega^2}{\omega_r \omega} \right)^2}, \quad (1.23)$$

while the reactive part is given by

$$Z_i(\omega) = R_s \frac{Q \frac{\omega_r^2 - \omega^2}{\omega_r \omega}}{1 + Q^2 \left( \frac{\omega_r^2 - \omega^2}{\omega_r \omega} \right)^2}. \quad (1.24)$$

In complex notation, the longitudinal coupling impedance is then given by

$$Z_L(\omega) = \frac{R_s}{1 + jQ \left( \frac{\omega_r^2 - \omega^2}{\omega_r \omega} \right)}. \quad (1.25)$$

In case of a short range wake field, assuming  $Q \approx 1$ , the longitudinal impedance given by Eq. 1.25 can also be used as simplified impedance model for the whole machine, the so called *broad band impedance*. This formula, characterized by a small number of parameters, allows for analytical evaluation of single bunch stability limits or instability growth rates, as shown in Chapter 5.



## Chapter 2

# The CERN Proton Synchrotron

The CERN accelerator complex comprises a chain of linear and circular machines that accelerate protons and ions to increasingly higher energies. In the last element of this acceleration chain, particle beams are accelerated up to the energy of 4 TeV, but the complex includes also several experiments that need beams at lower energies. At the beginning of the proton accelerating chain, LINAC 2 accelerates the beam to the energy of 50 MeV, injecting it in a circular machine called Proton Synchrotron Booster (PSB), which accelerates the protons to 1.4 GeV. After that, the beam is accelerated by the Proton Synchrotron (PS) at the energy of 25 GeV and by the Super Proton Synchrotron (SPS) to the energy of 450 GeV. The protons are finally transferred to the two beam pipes of the Large Hadron Collider (LHC), where the two beams circulate clockwise and anticlockwise, respectively. When the nominal energy of 7 TeV is reached, the beams collide in four detectors – ALICE, ATLAS, CMS and LHCb – where the total energy at the collision point can reach 8 TeV. The CERN accelerator complex includes the Antiproton Decelerator (AD) and the Online Isotope Mass Separator (ISOLDE) facility, and feeds the Compact Linear Collider (CLIC) test area, as well as the neutron time-of-flight facility (nTOF). Protons are not the only particles accelerated in the LHC. Lead ions for the LHC enter into LINAC 3 before being collected and accelerated in the Low Energy Ion Ring (LEIR), then following the injection scheme as the protons to reach high energy.

This thesis work is focused on the study of the CERN Proton Synchrotron: in this chapter, a brief description of the main machine parameters and types of beam is provided. Moreover, in order to introduce the devices that have been studied in Chapters 3 and 4, in the framework of the determination of the beam coupling impedance models, a short description of machine elements like magnets, cavities, vacuum equipments, is also provided.

## 2.1 Description of the machine

The CERN Proton Synchrotron was built in 1959 [6]. At that time, it was the first circular proton machine providing strong focusing and accelerating particle beams at the energy of 24 GeV. At the beginning of its activities, the PS was the only circular accelerator at CERN. The injection, at the energy of 50 MeV, was provided by the linear accelerator LINAC 1. The PS Booster was built only at the end of the 70s, in order to work as PS injector. The PS operation as LHC injector started in 2008, when a particle beam circulated into the 26 km ring for the first time. After more than 50 years of reliable operation, the PS is still considered a fundamental scientific tool for beam dynamics studies and experiments. Today we consider part of the PS accelerator complex also the two linear accelerators LINAC 2 and LINAC 3, and three smaller circular machines, namely PS Booster, LEIR (Low Energy Ions Ring), and Antiproton Decelerator (AD). A sketch of the complex is shown in Fig. 2.1, while in table 2.1 some important parameters of the PS are summarized.

The PS is a circular machine with a diameter of 628 m, made of 100 straight sections

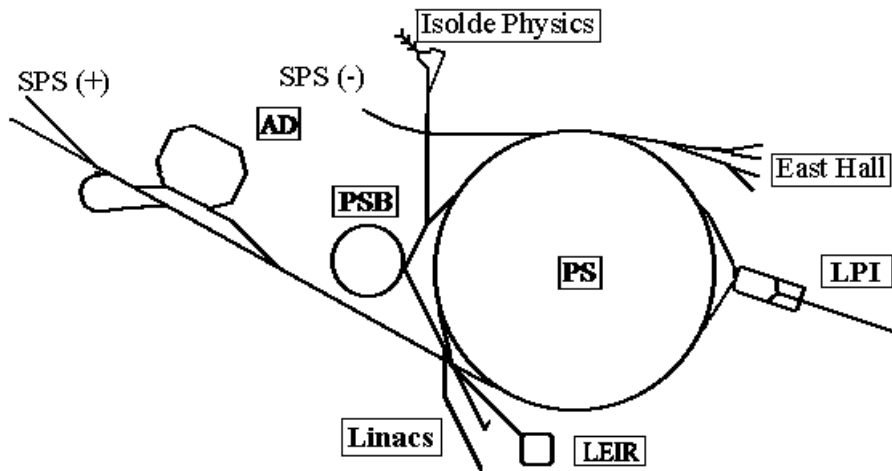


FIGURE 2.1: Proton Synchrotron complex layout.

and 100 magnet units [6]. The main magnet system consists of 100 combined function magnet units (MU), each composed of a focusing (F) half-unit and a defocusing (D) half-unit. A half-unit comprises five adjacent magnet blocks, each 417 mm long; the single MU is then made by ten blocks (five focusing and defocusing), excited by the same coil. Accelerating cavities, beam diagnostic devices and injection and extraction elements are installed in straight sections, that are placed between two subsequent magnet units. Moreover, correction magnetic lenses are also usually placed in the straight sections between two main magnet units. The use of the combined function magnets requires special pole profiles to provide a correct bending and focusing of the particle beam. In order to introduce a current distribution that generates additional low amplitude

TABLE 2.1: Main parameters of the PS machine for the 25 ns bunch spacing.

Machine parameter	Injection	Top
Circumference [m]	628.32	628.32
Kinetic energy [GeV]	1.3892	25.0787
Momentum [GeV/c]	2.13	26
Gamma	2.4806	27.7286
Beta	0.915145	0.999349
Revolution frequency [Hz]	436647.3424	476824.1330
RF frequency [MHz]	3.0565	10.0133
Harmonic number	7	21
Synchrotron frequency [Hz]	600	230
$Q_s$	0.00137	0.00048
Working point ( $Q_x, Q_y$ )	6.21, 6.24	6.21, 6.24
Gamma transition	6.1	6.1
RMS bunch length [cm]	1206.6413	26.8142

magnetic field for main field distortion compensation, the so-called *Pole Face Windings* (PFW) are placed on the magnet poles. These correction devices, together with the Figure-of-Eight Loop (F8L), act along the whole main magnet unit, providing a way to control the betatron tune and the chromaticity. Quadrupolar and octupolar distortions are corrected with lenses installed in the straight section, while PFW are dedicated to correct sextupolar field components resulting from saturation and the leakage field at high field levels. In the following sections, a brief description of some important devices installed in the machine (and considered in the computation of the PS impedance model in Chapter 3 and 4), is given. Also a short description of the main types of PS beams, together with some beam spectra measurement results, are provided.

### 2.1.1 Kicker magnets and septa

Injection and extraction systems are used to insert beams in the expected trajectory with the correct phase space parameters, while minimizing the beam losses. A septum is a device that can separate two regions in cavity-like structure, creating two regions of homogeneous (electric or magnetic) field [7]. In this way a septum provides a space separation of circulating and injected/extracted beam. On the contrary, a kicker magnet provides a separation of beam to be injected and extracted based on time selection [8]. Septa provide slower field rise and fall times, but stronger field than kicker magnets. The latter provide fast field rise and fall times, but relatively weak fields. In the PS, a combination of septa and kicker magnets is used for injection and extraction of beams, using several techniques like single-turn injection and extraction. In the single-turn (fast) injection, a septum deflects the beam into the closed orbit in the center of the kicker, while the kicker compensates for the remaining angle. The kicker field must rise from zero to

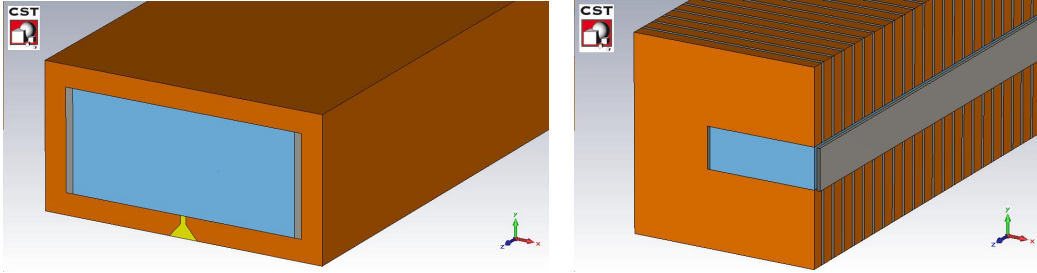


FIGURE 2.2: Design of kickers KFA28 (left) and KFA13 (right). KFA28 is designed with frame shape ferrite and an aluminium insert; KFA13 is designed C-shape ferrite with longitudinal segmentation.

full field in the time interval between the beam is circulating and the start of injection; the field falls from full field to zero between the end of injection and the circulating beam. Single-turn (fast) extraction is the process of ejecting a particle beam into a transfer line or a beam dump, at the appropriate time. It is based on time selection of the beam to be extracted, meaning that the kicker magnet deflects the entire beam into the septum in a single turn. The extracted beam passes through the homogeneous field region of the septum, while the circulating beam, before extraction, is in the field-free region of the septum (space separation of circulating and extracted beam). The septum then deflects the entire kicked beam into the transfer line.

Fast kicker in the PS are magnets, based on ferrite-loaded transmission line, with a rectangular-shaped aperture. The magnetic flux density in the aperture  $B_v$  of the kicker is given by

$$B_v = \mu_0 \left( \frac{NI}{V_a} \right), \quad (2.1)$$

where  $\mu_0$  is the permeability in free space,  $N$  is the number of turns,  $I$  is magnet current, and  $V_a$  is the distance between the inner edges of the ferrite. Beams in high intensity accelerators are, in general, very sensitive to longitudinal and transverse beam coupling impedance coming from kickers, due to their ferrite yoke. In particular, heating of the ferrite beyond the Curie temperature could be provoked by the coupling impedance. The longitudinal impedance can be significantly reduced by serigraphy of ferrites, insertion of beam screens within the kicker magnet aperture and the use of striplines instead of a ferrite loaded magnet. The following kickers are currently installed in the PS machine [9]:

- injection kicker KFA45 in SS45: delay line design, the ferrite is split longitudinally in eight cells. Each cell is 25 mm long: 20 mm of ferrite and 5 mm of aluminium.
- extraction kicker KFA71/79 in SS71 and SS79: delay line design, the ferrite is split longitudinally in nine cells. Each cell is 24 mm long: 19 mm of ferrite and 5 mm of aluminium (see Fig. 2.2 on the right).

- CT extraction kicker BFA9/21 (pedestal and staircase) in SS9 and SS21: lumped magnets, i.e., the ferrite is not split longitudinally in many cells.
- injection kicker for ions KFA28 in SS28: lumped magnets, i.e., the ferrite is not split longitudinally in many cells. An aluminium insert is added to reduce the impedance seen by the beam (see Fig. 2.2 on the left).
- multi-turn extraction kickers KFA13 and KFA21 in SS13 and SS21: similar to extraction kicker KFA71/79 (see Fig. 2.2 on the right);
- multi-turn extraction kicker KFA4 in SS4: delay line design, the ferrite is split longitudinally in twenty-four cells. Each cell is 24 mm long: 19 mm of ferrite and 5 mm of aluminium. The modules have been retrieved from the extraction kickers for leptons.

In Table 2.2 the geometrical parameters of the eleven PS kickers are summarized.  $a$  and  $b$  are the horizontal and vertical aperture,  $h$  is the height of the ferrite and  $L$  is the longitudinal size of the kicker. In particle accelerators we can distinguish between

TABLE 2.2: Geometry of PS kickers.

	a [mm]	b [mm]	h [mm]	L [m]
PI.KFA04 (A)	56	37	40	0.615
PE.KFA13 (A)	73.5	26.5	100	0.666
PE.KFA21 (A)	73.5	26.5	100	0.666
PI.KFA45 (A)	75	26.5	40	0.884
PE.KFA71 (A)	73.5	26.5	100	1.998
PE.KFA79 (A)	73.5	26.5	100	0.666
PI.KFA28 (B)	79.5	35	15	0.925
PE.BFA09P (B)	79	26.25	20	0.54
PE.BFA21P (B)	79	26.25	20	0.54
PE.BFA09S (C)	79	26.25	20	0.54
PE.BFA21S (C)	79	26.25	20	0.54

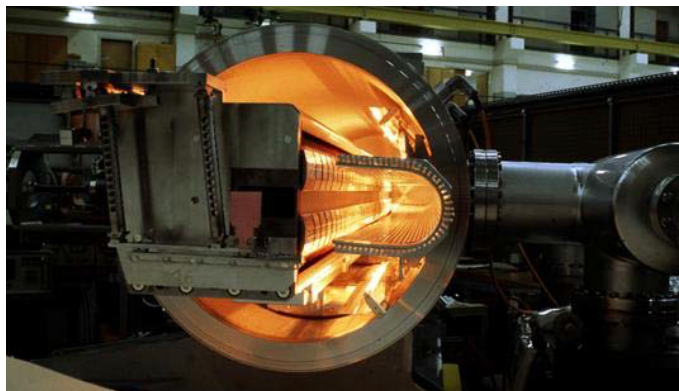


FIGURE 2.3: Magnetic septum SMH16.

electrostatic septa and magnetic septa. An electrostatic septum is a DC device with very thin (typically in the order of  $100\ \mu\text{m}$ ) separation between the zero field and high field regions. A magnetic septum is either a pulsed or DC dipole magnet with a thin (typically in the order of 2-20 mm) separation between the zero field and high field regions. Ten septa, with different purposes, are currently installed in the PS machine:

- Magnetic septum SMH16 for proton ejection to SPS;
- Electrostatic septum SEH23 for proton extraction to East Hall;
- Magnetic septum SMH26 for ion injection from LEIR and antiproton ejection towards LEAR;
- Electrostatic septum SEH31 for proton extraction towards SPS.
- Magnetic septum SMH42 for proton injection from the Booster;
- Magnetic septum SMH57 for slow extraction to East Hall;
- Magnetic septum SMH58 for electron ejection to SPS;
- Magnetic septum SMH61 for slow extraction to East Hall;
- Magnetic septum SMH74 for electron injection from LPI;
- Magnetic septum SMH92 for positron injection from LPI.

In Fig. 2.3 the magnetic septum SMH16 is shown: the maximum field is 1.2 T for a pulsed current of 28.5 kA, while the fringe field is less than 1/1000 of the gap field at a 50 mm distance from the septum conductor. Due to the very high level of radiation produced by the septum SMH16, a protection septum has been installed during LS1 in the straight section 15; the design of this device is discussed in details in Chapter 5.

### 2.1.2 RF cavities

In order to generate bunch trains for LHC, the PS is equipped with several RF systems for longitudinal beam manipulations, operating at the frequencies of 10, 20, 40, 80 and 200 MHz. The combined use of a 10 MHz system (working on harmonic 21) and a 20 MHz system (working on harmonic 42), followed by a 40 MHz system (working on harmonic 84) and a 80 MHz system (working on harmonic 168) allows to produce the desired beam pattern and filling scheme. The nominal filling scheme for LHC requires bunch trains of 25 ns bunch spacing [10]; four bunches are sent from the PSB and captured on four consecutive buckets on  $h=7$  in the PS. On the following cycle, two more bunches are

provided (*double batch filling*). The 25 ns bunch spacing is then generated at extraction, when the bunches are shorter than 5 ns to fit the SPS 200 MHz RF system. This is achieved just before PS ejection at 25 GeV by debunching and rebunching the beam on  $h=84$ , followed by bunch rotation. An alternative method that allows to avoid the process of debunching and rebunching, consists in changing the number of bunches by using multiple splitting: captured on  $h=7$  in the PS, the bunches are split in three at 1.4 GeV (*triple splitting*) and accelerated on  $h=21$ . At 25 GeV, each bunch is split twice in two (*double splitting*) by the 20 MHz system, so that finally 72 bunches are created on harmonic 84. Finally the 80 MHz systems shorten the bunches to 4 ns, in order to fit into the SPS 200 MHz buckets. The change from the debunching-rebunching scheme to the multiple splitting required the installation of a 20 MHz RF system.

The 75 ns bunch spacing scheme was used in the early period of operation of LHC, to minimize the electron cloud effects. The six bunches were split into two at injection energy, providing 12 bunches in  $h=14$ . Acceleration is done on this harmonic up to 25 GeV. At this energy, bunches are again split into two from the 13.3 MHz system (24 bunches in  $h=28$ ). The RF system on  $h=84$  ( $3 \times 28$ ) reduces to zero the voltage at  $h=28$ . Just before extraction, bunches are rotated by modulating the voltages at 40 and 80 MHz ( $h=84$  and  $h=168$ ) like for the nominal LHC beam.

### 2.1.2.1 40 and 80 MHz cavities

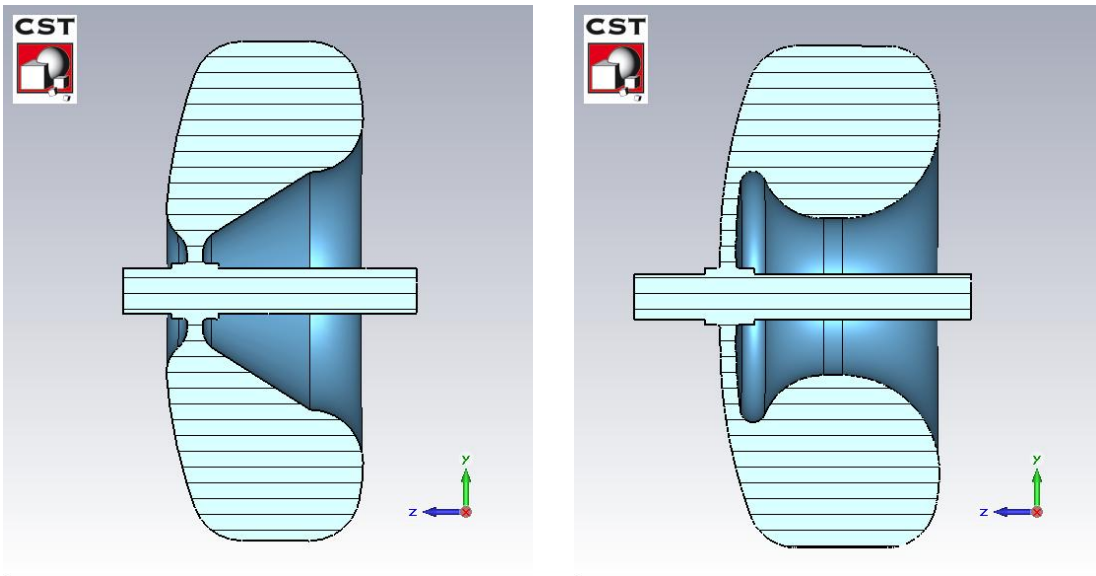


FIGURE 2.4: Design of the 40 MHz (right) and 80 MHz (left) cavities for simulations.

The 40 MHz cavity has been designed and built at CERN as part of the preparation of the PS as injector for LHC [11], with the aim of providing a bunch spacing of 25 ns. The cavity was designed with an  $R/Q$  of  $33 \Omega$  and an unloaded  $Q$  of 18200. It is provided

of a mushroom shaped gap electrode which makes capacitive coupling possible, and two tuners for regulation of the resonance frequency and compensation of slow temperature and atmospheric pressure variations. The shape of the cavity is shown in Fig. 2.4 on the right.

While the requested bunch spacing is obtained with the 40 MHz system, the nominal bunch length is obtained using the 80 MHz systems. Two 80 MHz cavities were installed and commissioned during 1998 as part of the preparation of the PS as injector for LHC [12]. The mechanical design is similar to that of the 40 MHz cavity with many common parts. In contrast to the 40 MHz, the 80 MHz cavity, equipped with a cooling water circuits, was designed to enable long pulse operation. An R/Q of  $56 \Omega$  with an unloaded Q of 22600, has been designed. A magnetic coupling loop was adopted since the gap electrode is much smaller than the 40 MHz, and a capacitive antenna would have been excessively long. The tuners of the 80 MHz cavity, for resonance frequency regulation, are capacitively coupled piston. The shape of the cavity is shown in Fig. 2.4 on the left.

### 2.1.2.2 10 MHz cavities

The PS 10 MHz system [13] includes eleven cavities located in straight sections 11, 36, 46, 51, 56, 66, 76, 81, 86, 91 and 96, for a total of ten cavities plus an additional spare (located in SS11). Working at frequencies from 2.8 MHz to 10.01 MHz, the cavities are needed to form the bunches after injection, accelerate them to the desired energy and perform bunch splitting and rotation before extraction. Every cavity is split into two resonators (sections), in order to deal with the voltage limit (10 kV) for the gap relays that are used to shorten the accelerating gap outside the RF pulse. As a consequence, a single 10 MHz cavity consists of two ferrite loaded  $1/4$  wave lines, with a capacitive gap at the input end. The ferrite rings are made of Ferroxcube 4E1 ( $\mu = 14$ ) and provided with a water-cooled copper disks. Each cavity has a total of nineteen rings, with a 440 mm outer diameter, 250 mm inner diameter, and 33.3 mm thickness. The cavity ferrite loss resistance is very high for low level signals at LF (3 MHz), providing a cavity unloaded Q of 130, that is reduced to 30 when connected to the amplifier. Tuning is performed by a PLC that moves two variable vacuum capacitors, connected in parallel to the gaps. The design of the cavity is shown in Fig. 2.5.

### 2.1.2.3 200 MHz cavities

The decision to build the SPS, taken in 1972, significantly increased the requirements on the PS, which was requested to deliver high-intensity beam bunched at the SPS frequency of 200 MHz. In this context, the 200 MHz system was built to be used as pre-modulation

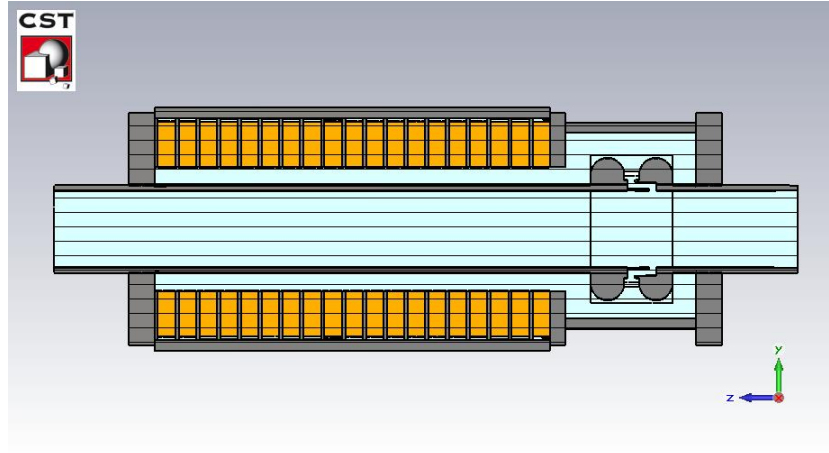


FIGURE 2.5: Design of the 10 MHz cavity for simulations.

of the extracted beam [14]. In this framework, tests with beam quickly revealed an unacceptable longitudinal blow-up during debunching, due to longitudinal microwave instability. It was soon realized, however, that the newly installed 200 MHz cavities could provide a mitigation to that problem [6]. It was observed that, driving some 200 MHz cavities with a phase modulated signal at an harmonic of the accelerating RF frequency, the longitudinal emittance of the bunches could be blown up in a controlled way during the early part of the acceleration cycle. In this way, it was possible to keep the beam below the instability threshold. The longitudinal emittance of the bunches in the CERN PS must be increased before transition crossing to avoid beam loss due to a fast vertical instability [15]. This controlled blow-up is essential for all high-intensity beams in the PS, including those for transfer to the LHC. The 200 MHz system is made of six cavities located in SS06 (see Fig. 2.6). Each cavity is equipped with two magnetic loops (see Fig. 2.7 on the right) and three PIN diodes lines terminated by a  $50\ \Omega$  load, which allow their  $Q$  and shunt impedance to be reduced by more than an order of magnitude (diodes are either open, which terminates the line with the  $50\ \Omega$  in parallel, or closed, which can be modeled as a short circuit). The designed  $R/Q$  is  $28.5\ \Omega$ . Table 2.3 summarizes the values of unloaded  $Q$  and shunt impedance designed for the different work conditions of the single 200 MHz cavity. Before applying RF power and getting voltage across the gap, damping is suppressed by short-circuiting the resistive loads with PIN diodes. When driven by the RF amplifier, the equivalent impedance of the cavity is minimized by adjusting the length of the feeder line. Each cavity is equipped with four cylindrical tuners for resonance frequency regulation (see Fig. 2.7 on the left).

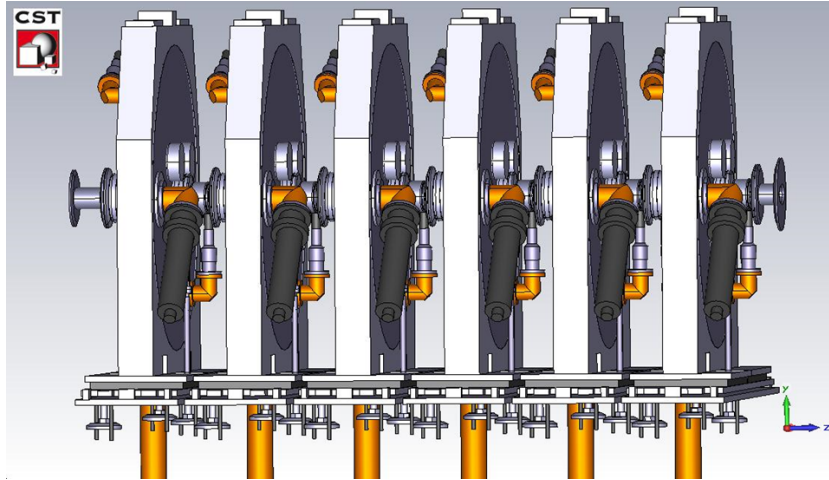


FIGURE 2.6: Model of the 200 MHz cavities for simulations.

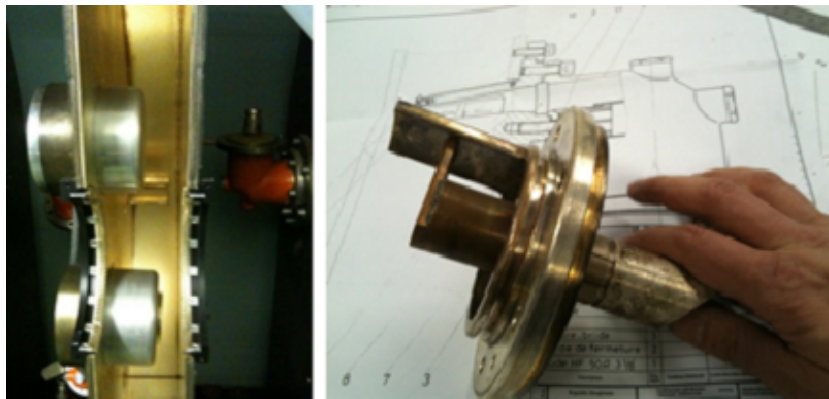


FIGURE 2.7: 200 MHz cavity tuners (left) a the magnetic coupler for the fundamental mode (right).

TABLE 2.3: Values of unloaded Q and shunt impedance designed for the different work conditions of the single 200 MHz cavity.

	$Q_0$	$R_s$ [ $k\Omega$ ]
Naked cavity	1900	54140
Operational cavity	1000	28500
Terminated with 1 line 50 $\Omega$	328	9350
Terminated with 2 line 50 $\Omega$	200	5700
Terminated with 3 line 50 $\Omega$	130	3700

### 2.1.3 Beam chambers and vacuum instrumentation

#### 2.1.3.1 The PS beam chamber and its features

The typical beam chamber in the PS has an elliptical cross-section of vertical half-aperture 35 mm and horizontal axis half-aperture of 73 mm (Fig. 2.8 on the left). Another common beam chamber geometry presents a rectangular-like shape, also called *racetrack*, with vertical half-aperture of 36 mm and horizontal half-aperture of 92 mm (Fig. 2.8 on the

right). In this type of chambers the beam is usually circulating in the geometrical center

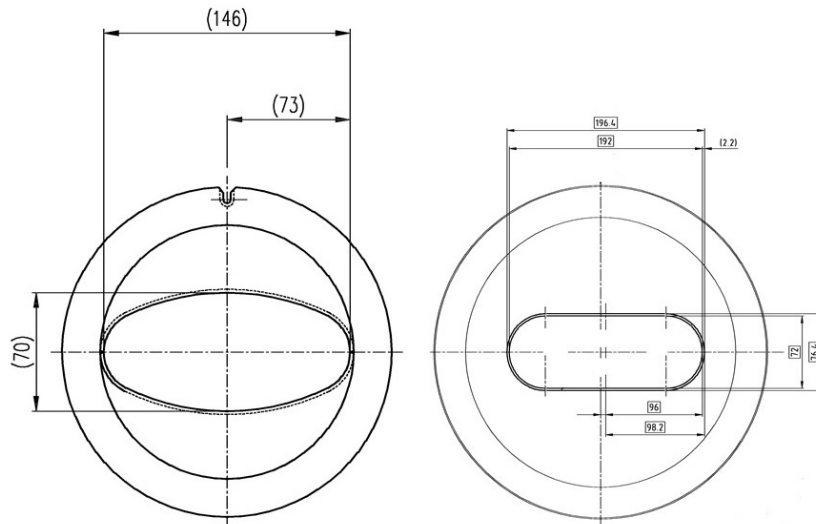


FIGURE 2.8: Mechanical drawings of two more common PS vacuum chambers. CDD reference: PS VCS0024, STDVFCON0063.

of the tube, while in sections where the beam is injected and extracted the beam chamber has usually a larger horizontal aperture and an asymmetric elliptical cross section, which allows the beam to move on the horizontal axis of the tube. For example, in PS sections 43, 60 and 62 we can find some example of asymmetric beam chambers that allows injection and extraction of particle beams. A particular feature of only these three straight sections of the PS are the horizontally not aligned beam chambers, which result in potential coupling impedance related issues. An example is shown in Fig. 2.9. Different types

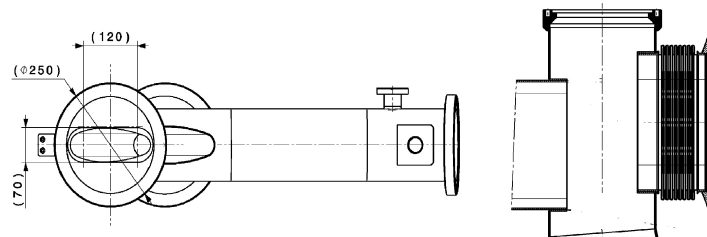


FIGURE 2.9: Mechanical models horizontal misaligned 43 of section: front view (left) and upper view (right). CDD reference: PS VCBCG0001.

of beam chamber are usually connected in the straight sections with bellows and flanges. Bellows are used in accelerator vacuum system to perform several functions, like fixing transverse offset in beam line hardware, providing flexibility for installation of devices, reducing stress on vacuum joints, providing expansion or contraction during thermal cycles. Depending on the purpose, bellows present a certain number of undulations, a maximum extended length and a minimum compressed length. In the PS about 230 unshielded bellows are currently installed, matching beam tubes of different cross-sections. Devices

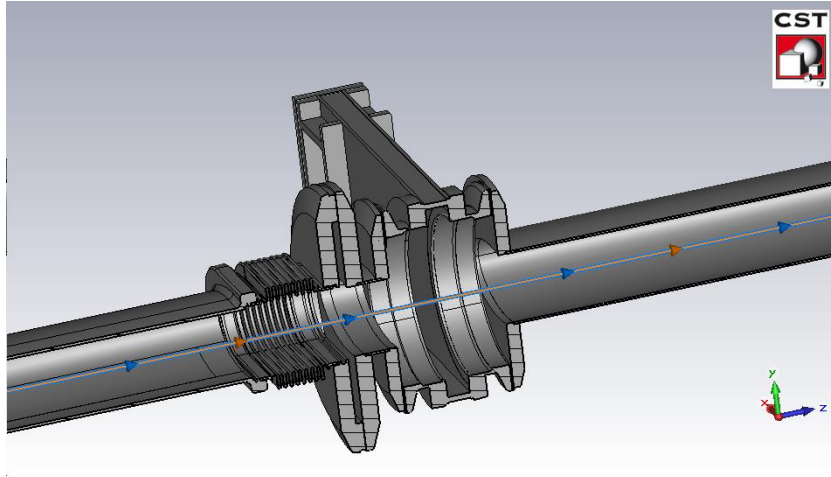


FIGURE 2.10: 3D model of the horizontally misaligned PS SS60 where are installed three flanges, a VVS and a bellow.

like kickers, cavities, instrumentation and septa usually have a circular tank, connected to a elliptical or rectangular beam pipe through flanges, which result in a *step transition*. This is clearly visible from the horizontal and vertical apertures plot shown in Fig. 2.11.

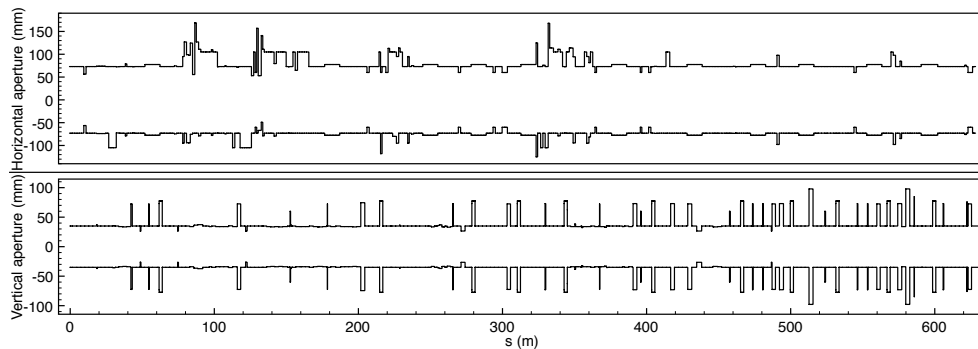


FIGURE 2.11: Horizontal and vertical physical apertures of the PS vacuum chamber.

### 2.1.3.2 Vacuum pumps and valves

When the PS was designed and built, the vacuum system consisted of 100 pumping groups (one for each straight section), each one composed of a rotary pump and an oil diffusion pump [16]. The pressures reached at that time were in the order of  $10^{-4}$  Pa. Due to the problems caused on the beam by the heavy hydrocarbon molecules, in the late '60s, the change to ion pumps was made. After mid '80s, when all 100 magnets received new vacuum chambers made of vacuum fired 316L+N stainless steel, it was possible to get an average pressure of  $10^{-6}$  Pa under static conditions. The pumps currently installed in the PS are made of a circular tube intercepting transversally the beam chamber, as shown in Fig. 2.12. In particular, the beam chamber is entering inside the vacuum pumps for few

millimeters on both sides. A sketch of two vacuum pump connections with the beam pipe is shown in Fig. 2.12 [17]. For each of the ten sectors of the PS, a sector gate valve (VVS) is installed, in order to prevent leak propagation and allow mechanical interventions. To avoid leaks, an interlock signal is sent to the VVS controller when several pressure readings rise above a given threshold in the same vacuum sector; the valve will then confine the leakage in the vacuum sector. A picture of a PS VVS is shown in Fig. 2.13.

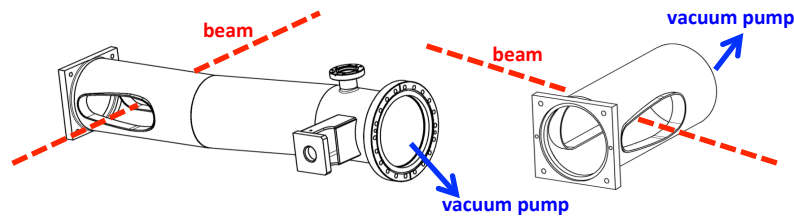


FIGURE 2.12: Sketch of two vacuum pump connections with the beam pipe.



FIGURE 2.13: Picture of a PS sector valve.

### 2.1.3.3 Flanges

For several particle accelerator devices like RF cavities, septa or beam instrumentation, the vacuum chamber is connected to the ground, creating a loop between the vacuum chamber and its ground connection. Fast variation of the magnetic field in circular machine may therefore induce currents in the loops, that are source of unwanted field disturbances, and can provoke harmful effects on the beam orbit. In the PS machine, in the late '80, low energy current loops of several tens of Amperes have been detected, resulting in the loss of 50-100% of the beam [18]. Most of the time is practically impossible to avoid the ground connections thus, to overcome the problem, the vacuum chamber of a given

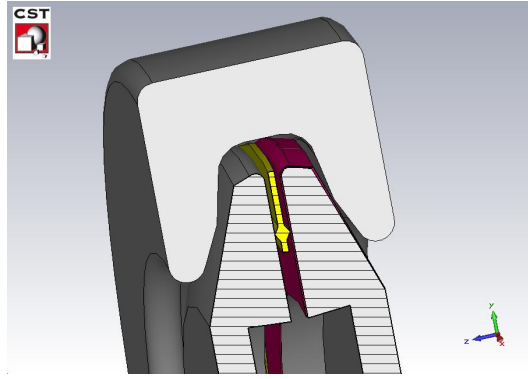


FIGURE 2.14: 3D model for simulations of a SPS 273 flange installed in the PS.

sector can be interrupted (one sector for each ground connection) and reconnected with an isolated flange [19]. By flange we mean two thin circular metallic plates, kept at a few millimeters distance by an external collar. The plates, pierced with a hole of the dimension of the beam chamber, is then welded at the interruption of the chamber. The isolation is obtained with a thin ceramic layer (0.2 mm width) placed on one of the two plates. The *isolated* flange forms a capacitor, which inserted in series with the ground loop, constitutes a parallel RLC equivalent circuit. In this circuit, the low frequency inductance  $L$  is given by the beam line and earth leads, the capacitance  $C$  is given by the thin insulating ceramic and the flange electrodes, and the resistor  $R$  represents all the loss mechanisms in the circuit (conductor resistance, eddy current and hysteresis losses in the portion of the beam line going through magnets and radiation) [20]. The measured values for the equivalent circuit are  $C=1000$  pF,  $L=10$   $\mu$ H,  $R=100$   $\Omega$ , yielding to a resonant frequency of 1.5 MHz with  $Q=1$  [18]. Such a resonator is traversed by the beam image current flowing along the vacuum chamber, leading to beam coupling impedance and related instabilities. To decrease the impact of these unwanted effects, a so-called RF-bypass [21] consists of a large capacitor  $C_1 = 0.4$   $\mu$ F in series with a small resistor  $R_1 = 1$   $\Omega$ , was connected in parallel to each flange. The effect of the RF by-pass is to shift the resonant frequency to a much lower value (100 kHz), reducing the coupling impedance of the device. In general, the PS beam pipe is grounded on the downstream side of the magnet. All the 100 PS straight sections have two isolated flanges upstream and downstream of the magnet unit: looking from the inside of the ring, the upstream flange separates the element from the ground of the straight section magnet and the downstream flange disconnects the main magnet from the next straight section. Not all the 200 flanges are provided with an RF bypass: in general, the downstream flange has always an RF bypass to separate its DC-wise from the next main magnet. However if the beam pipe of a straight section is floating with respect to ground, the upstream flange connection is short-circuited by a metallic part. Otherwise, if the beam pipe of a straight section is already grounded (for example where there is a cavity), the flanges on either side have an RF bypass.



FIGURE 2.15: Flange disk with ceramic layer (left); one of the isolated PS flange provided by RF bypass installed in the ring (right).

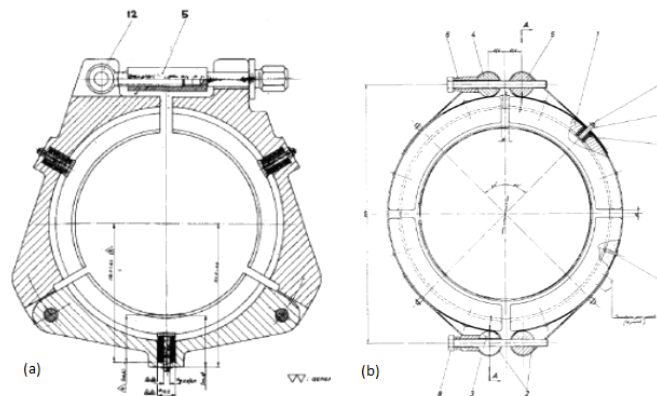


FIGURE 2.16: Mechanical models of the PS type collar (left) and SPS type collar (right).  
CDD references: 8095.0277.1B

More flanges, not isolated and not provided with RF bypass or short circuit, are welded in the straight sections to connect devices to the beam chamber, and are usually referred as *metallic*. Five different types of flanges, for a total of 259 elements, are currently installed in the machine:

- PS 195, 179 elements, external diameter 195 mm;
- PS 250, 56 elements, external diameter 250 mm;
- SPS 273, 9 elements, external diameter 332 mm;
- SPS 159, 8 elements, external diameter 206 mm;
- SPS 219, 7 elements, external diameter 266 mm;

PS and SPS flanges type can be distinguished thanks to the shape of the external collar [22], which is round in the case of the SPS and triangular in the case of PS, as shown in Fig. 2.16. The two plates of every type of isolated or metallic flange are separated by

an aluminium gasket of 2.5 mm width; the two plates are then connected together by the metallic collar, as shown in Fig. 2.14. This design creates a cavity-like structure of 2.5 mm length. In addition, some flanges type present an additional hollow in the inside part of the plates: as shown in Fig. 2.14, SPS 273 presents a step of 7.5 mm on each disk, generating an internal cavity of 17.5 mm length. The type PS 195 includes a step of 1 mm each disk, creating a cavity of 4.5 mm length. For isolated flanges, the ceramic layer is also covering a part of the external surface of the disk. The collar pushing together the two plates is in contact with the isolator itself on one side, and not with metal. Thus leaves some of the electromagnetic fields generated by the interaction of the beam with the cavity radiating outside the structure. The RF bypass is then installed in the proper way to intercept this radiation.

## 2.2 PS as LHC injector: the upgrade program

The LHC injectors upgrade (LIU) project [23] [24], started in 2010, has the objective of providing reliable beams with the challenging characteristics required by the High Luminosity LHC [25] until at least 2030, having as final goal the reduction of the statistical error in the measurements at the interaction points of LHC. For a given event at the LHC interaction points, if  $N$  is the number of observations, the error is proportional to  $1/\sqrt{N}$ . An increase of the number of observations would improve the statistical significance of the data. In this framework, the High Luminosity LHC project is aimed at establishing the necessary changes in the machine in order to improve collisions statistics. In particular we can define a parameter called *luminosity*  $L$  that depends on beam parameters as follows [26]:

$$L = \frac{N_p^2 n_b f_{rev} \gamma}{4\pi \sqrt{(\epsilon_x \beta_x \epsilon_y \beta_y)}} F, \quad (2.2)$$

where  $N_p$  is the number of protons per bunch,  $n_b$  the number of bunches,  $f_{rev}$  the revolution frequency,  $\sqrt{\epsilon_j \beta_j}$  the transverse beam dimension at the interaction point and  $F$  a factor due to the crossing angle between the colliding beam trajectories. An increase in the luminosity has the effect of increasing the number of events, according to

$$L = \frac{N_e}{\sigma_e}, \quad (2.3)$$

where  $N_e$  is the number of collisions per second and  $\sigma_e$  is the event cross-section.

At the beginning of 2012, a peak luminosity of  $6 \cdot 10^{33} \text{ cm}^{-2}\text{s}^{-1}$  was reached in the LHC at the energy of 4 TeV: the final goal of the HL-LHC [27] is to achieve a value of  $10^{35} \text{ cm}^{-2}\text{s}^{-1}$ , ten times more than the design value of the LHC. This requirement can only be reached by performing an upgrade of the total LHC injector chain. As a consequence, the LHC

Injectors Upgrade (LIU) project was started in order to consider the necessary changes and their possible implementations in the different machines of the chain.

During the PS upgrade, that consists in increased luminosity producing high intensity and high brightness beams, some major issues have been encountered. At the injection energy of 1.4 GeV, unwanted effects from space charge were observed. The first four bunches injected from PSB are kept at injection energy for 1.2 seconds, and since the beam encounters several resonances, this results in transverse emittance blow up. One of the main purposes of the LIU project becomes the increase of the PS injection energy from 1.4 GeV to 2 GeV, that would reduce consistently the space charge effects. Other major issues in the machine are the *Head-Tail* instability, that may determine beam loss effects, and the vertical *TMCI* instability, that may arise at transition crossing for high intensity beams. Electron cloud is also of concern, since their formation was observed soon before ejection at 26 GeV, but without any effect on beam quality.

### 2.3 Beams in the CERN PS

Several types of operational and LHC-type beams are prepared in the PS machine:

- AD: 26 GeV/c proton beam sent to the Antiproton Decelerator target;
- TOF: 20.3 GeV/c beam towards the n-TOF (neutron-Time Of Flight) facility beam line with very high nominal intensity ( $7.5E12$  ppb);
- SFTPRO: 14 GeV/c beam provided to SPS Fixed Target PROton physic;
- EASTA/EASTB/EASTC: beams dedicated to specific experiments for the North target of the East area.
- LHCINDIV: typical beam required in the commissioning filling patterns and MD for the LHC, 26 GeV/c;
- LHC25/LHC50/LHC75: Provide the LHC with 25-50-75 ns bunch spaced physics beam, 26 GeV/c.

Particle beams are injected, accelerated and extracted during one or more magnetic cycle basic periods, whose duration in the PS is a multiple of 1.2 seconds. The proton beam is usually kept on a flat bottom plateau, experiencing a constant magnetic field for a period of at least 30 ms, in order to reach an equilibrium state in the transverse and longitudinal planes, compensating for possible injection errors [28]. The beam is then accelerated to be extracted toward the SPS or a specific experiment thanks to a magnetic field rate  $dB/dt$  of about 21 G/ms.

### 2.3.1 PS beam spectra

RF measurement of beam spectra have been performed in order to have a better knowledge of the characteristics of the PS beams in relation with parameters used for impedance calculation. In this section the measurements performed for single bunch beams (TOF and LHC50) and for multibunch beams (LHCINDIV) are showed. The aim of this measurement campaign was to collect beam spectra in different timing of the PS magnetic cycle, to have a reference for heating and power loss calculation. Spectra have been acquired with a signal analyzer, measuring at the same time the main beam parameters and the bunch length  $4\sigma$ . Measurements revealed that high order modes in PS devices can be a potential source of heating related issues, only if they are falling inside the main lobe of the beam spectrum. For instance, at extraction energy, only the parasitic modes with a frequency that is lower than about 150 MHz should represent potential sources of power loss.

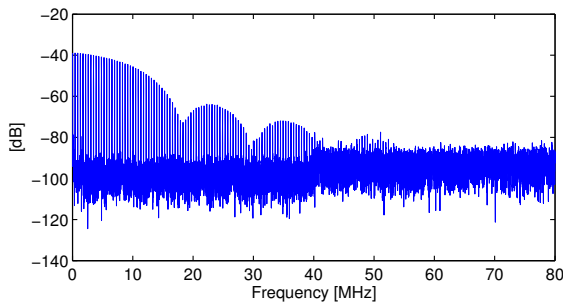


FIGURE 2.17: Single bunch LHC INDIV spectrum measured at C171 (flat top),  $6 \cdot 10^{10}$  ppb,  $4\sigma = 80$  ns.

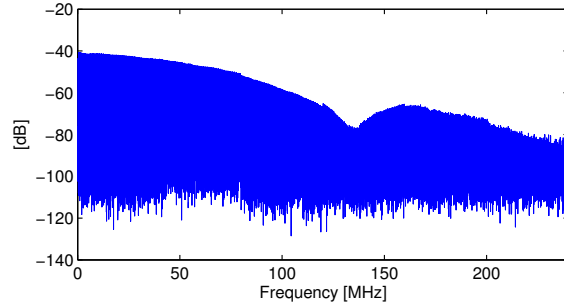


FIGURE 2.18: Single bunch LHC INDIV spectrum measured at C432 (transition),  $6 \cdot 10^{10}$  ppb.

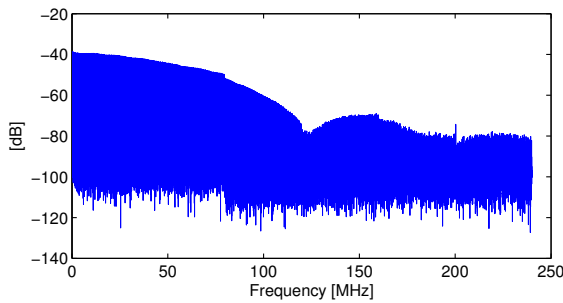


FIGURE 2.19: Single bunch LHC INDIV spectrum measured at C1254 (6 ms before extraction),  $6 \cdot 10^{10}$  ppb.

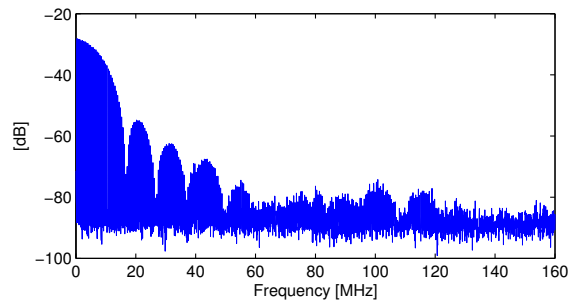


FIGURE 2.20: Single bunch TOF spectrum measured at C300 (flat top),  $94 \cdot 10^{10}$  ppb,  $4\sigma = 90$  ns.

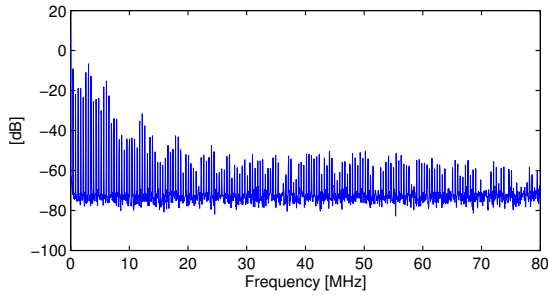


FIGURE 2.21: Multi bunch LHC50 spectrum measured at C198 (after first injection), intensity  $6.7 \cdot 10^{12}$  ppb, 6 bunches in  $h = 7$ .

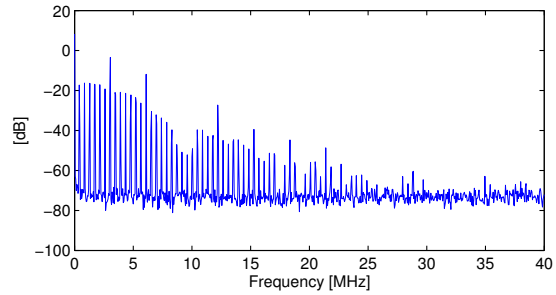


FIGURE 2.22: Multi bunch LHC50 spectrum measured at C1398 (after second injection), intensity  $6.7 \cdot 10^{12}$  ppb, 6 bunches in  $h = 7$ .

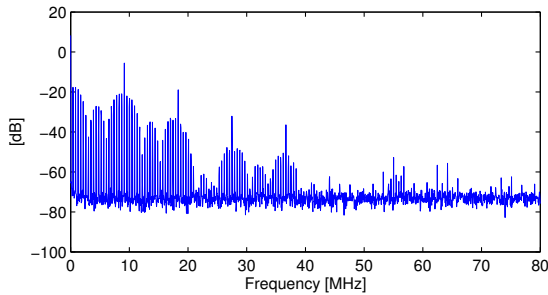


FIGURE 2.23: Multi bunch LHC50 spectrum measured at C1505 (end of flat bottom), intensity  $6.7 \cdot 10^{12}$  ppb, 18 bunches in  $h = 21$ .

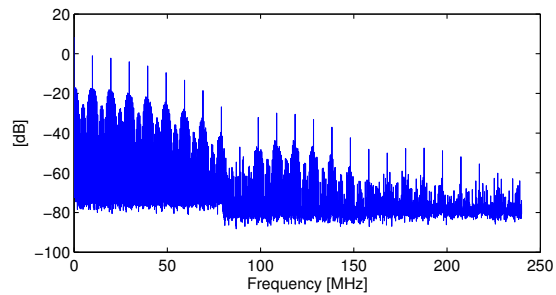


FIGURE 2.24: Multi bunch LHC50 spectrum measured at C1625 (5 ms before transition), intensity  $6.7 \cdot 10^{12}$  ppb, 18 bunches in  $h = 21$ .

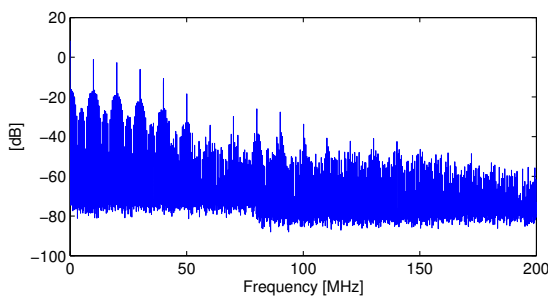


FIGURE 2.25: Multi bunch LHC50 spectrum measured at C2205 (flat bottom), intensity  $6.7 \cdot 10^{12}$  ppb, 18 bunches in  $h = 21$ .

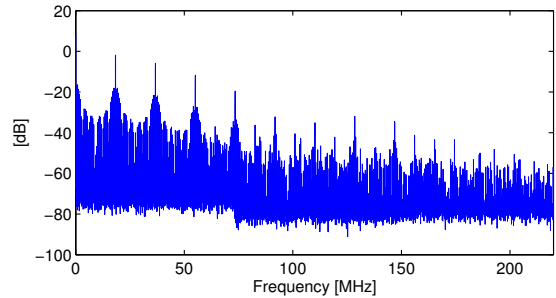


FIGURE 2.26: Multi bunch LHC50 spectrum measured at C2454 (6 ms before extraction), intensity  $6.7 \cdot 10^{12}$  ppb, 36 bunches in  $h = 48$ .



## Chapter 3

# The PS transverse impedance model

For the future operation at higher intensities and beam brightness required by the LIU project, it is of fundamental importance to detect the main sources of impedance in the machine and estimate with precision the transverse coupling impedance model. Some transverse instabilities that, kept under control, are not critical for the operation, have been observed in the machine: for example, the transverse damper currently installed in the PS is sufficient to damp the injection instabilities, and transition crossing should also be possible without major issues. However, a careful follow-up of the transverse impedance of the machine allows the possibility to accelerate high-intensity beams with lower longitudinal emittance through transition, and to minimize the interplay with space charge at injection energy.

### 3.1 Tune shift measurements for transverse impedance determination

Measuring the betatron coherent frequency shift with intensity, gives informations on the total reactive transverse impedance according to Sacherer's theory [29]. The number of betatron oscillation per turn of the bunch center of mass is called coherent betatron tune, and it is defined as

$$Q_0 = \frac{\omega_\beta}{\omega_0}, \quad (3.1)$$

where  $\omega_0$  is the machine revolution frequency and  $\omega_\beta$  is the betatron frequency. If the tune is an integer number, the particles follow the same trajectory every turn, and the amplitude of the betatron oscillations will increase resonantly until the particles are lost

by hitting the vacuum pipe. For example, the LHC is designed to collide protons with a betatron tune of 59.31: every turn the particles perform 59 (integer tune) full betatron oscillation and a further 0.31 of a period (fractional tune). When the trajectory repeats every two turns (1/2 integer resonance) or every three turns (1/3 integer resonance), these resonances become weaker the order.

The transverse horizontal and vertical tunes  $Q_x$  and  $Q_y$  can be measured in the PS with a Base Band Tune system based on diode detectors, known as the BBQ [30]. High amplitude short pulses obtained from a beam position monitor (BPM) are sent to diode detector which converts the modulation of the BPM pulses, related to beam oscillations, into a signal in the audio frequency range. This signal is then processed in order to obtain the tune content. BBQ measurements are performed on a single circulating bunch of particles. The transverse position of the bunch is acquired every turn by the BPM, while the tune is obtained from a Fast Fourier Transform (FFT) on the transverse motion of the beam centroid. To perform tune measurements, a chirp signal is emitted to excite the beam. Varying the intensity of the bunch, that correspond to the total number of proton (ppb), allows to observed a tune shift that is linear with the intensity. The intrinsic error of this technique is proportional to  $1/N_{turns}$ , with  $N_{turns}$  the number of turns during which the beam position has been measured with the BPM. The beam position can be acquired with two different monitors, one of that is described in details in Chapter 5.

For a Gaussian bunch of r.m.s. bunch length  $\sigma_z$  traveling with velocity  $v = \beta c$ , the coherent tune shift  $\Delta Q$  is proportional to the imaginary part of the transverse effective impedance  $Z_t^{eff}$  by [31]

$$\Delta Q = -\frac{\beta e I_0}{4\sigma_z \sqrt{\pi} \omega_0^2 \gamma Q_0 m_0} \text{Im}[Z_t^{eff}], \quad (3.2)$$

where  $I_0$  is the bunch current,  $Q_0$  is the zero current betatron tune,  $\gamma$  is the relativistic factor,  $e$  the particle charge,  $\omega_0$  the angular revolution frequency and  $m_0$  the particle mass at rest. The effective transverse impedance is defined as the impedance weighted by the transverse bunch spectrum centered at the chromatic frequency  $\omega_\xi$ :

$$Z_t^{eff} = \frac{\sum_{p=-\infty}^{\infty} Z_t(\omega') h(\omega' - \omega_\xi)}{\sum_{p=-\infty}^{\infty} h(\omega' - \omega_\xi)}, \quad (3.3)$$

where  $\omega' = \omega_0(p + Q_0)$  with  $p$  an integer,  $\omega_\xi = \omega_0 Q_0 \xi/\eta$ , with  $\xi$  the chromaticity and  $\eta$  the slippage factor, and the power spectrum of the Gaussian zero azimuthal bunch mode is  $h(\omega) = \exp(-\omega^2 \sigma_z^2/c^2)$ . If the bunch length does not change with intensity, Eq. 3.2 predicts a tune shift linear with bunch intensity, with a slope proportional to the imaginary part of the transverse total effective impedance. The detail of the theory of transverse bunched beam instabilities and the beam-impedance interaction developed by Sacherer can be found in [29] and [31].

### 3.1.1 Chromaticity

The tune variation  $\Delta Q/Q$  with the momentum is a machine parameter called *chromaticity* and it is defined as

$$\xi = \frac{\Delta Q/Q}{\Delta p/p}, \quad (3.4)$$

where  $p$  is the particle momentum in the closed orbit and  $\Delta p$  is the momentum deviation. For circular machine, chromaticity could have a negative impact on beam dynamics, introducing tune spread and unwanted effects like head-tail instabilities. It was observed that, above transition, head-tails instability growth rate are usually faster for negative than for positive chromaticity values, vanishing for zero chromaticity. Therefore circular machine like the PS usually operates, above transition, with zero or slightly positive chromaticity. We can also define *natural* chromaticity the effect that is only due to the elements of the linear lattice like quadrupoles. Natural chromaticity of a strong focusing circular accelerator is always negative and cannot be zero.

Horizontal and vertical chromaticities in the PS can be measured by acquiring the tune shift while varying  $\Delta p/p$ . In practice, introducing a radial offset, a momentum offset is generated, leading to a variation of the revolution frequency of the beam. The tune can be written as a Taylor series of  $\Delta p/p$

$$Q(\Delta p/p) = Q_0 + Q' \Delta p/p + \frac{Q''}{2!} (\Delta p/p)^2 + \dots + \frac{Q^n}{n!} (\Delta p/p)^n, \quad (3.5)$$

where  $Q_0$  is the unperturbed tune and  $Q^n$  are the higher order terms of the tune spread. The chromaticity is calculated applying a polynomial fit on the measured data: from the linear term we can calculate the linear chromaticity as

$$\xi = \frac{Q'}{Q_0}. \quad (3.6)$$

### 3.1.2 Control of the working point

While performing beam based measurements, choosing a good working point [32] is an essential aspect in order to obtain stable beams and reliable operation in general. In the case of the PS, bending and focusing of the beam is provided by the main magnet units; the working point, in absence of any auxiliary magnets or coils, is determined by the momentum of the beam. The bare machine at 2 GeV is working in linear condition (natural working point), with measured tunes of  $Q_x = 6.253$  and  $Q_y = 6.285$ , and chromaticities of  $\xi_x = -0.83$  and  $\xi_y = -1.12$ . Since there is no freedom in the choice of the parameters, the machine usually does not operate in this configuration. In order to correct the effects of linear and second order chromaticity in circular machines, the magnetic field higher order

components are needed to be kept under control. Dedicated magnets and auxiliary windings, such as the PFW in the PS (see Chapter 2), usually play this role. The PS PFW, consisting of four extra auxiliary coils per magnet mounted on the iron poles (two coils for the focusing and two for the defocusing yoke) are used to control the working point and chromaticity. In addition, the figure-of-eight loop creates opposite fields in the two yokes. In this way, the horizontal and vertical tunes, horizontal and vertical chromaticities, and eventually another parameter (for example the non linear horizontal chromaticity), can be controlled by five parameters. The relationship between the current variation in the circuit and the parameter was calculated from the measurement of the working point variation with respect to a programmed variation of the PFW or figure-of-eight loop currents. The matrix describing the effects of the five currents is available for the PS machine.

## 3.2 Tune shift measurements at zero chromaticity

### 3.2.1 Injection energy

An upgrade of the extraction energy from the PS Booster from 1.4 GeV to 2 GeV is planned for the next years with the aim of reducing direct space charge effects in the PS. This should enable to increase the beam brilliance throughout the LHC injector chain so that the LHC can reach the higher luminosities goals that should be reached by the LIU and HL-LHC project. For this reason, tune shift measurements have been performed at the energy of 2 GeV [33]. The single bunch beam parameters are summarized in Table 3.1. The measured vertical tune shift as a function of the beam intensity is shown in Fig 3.2. The tune is decreasing when the beam intensity increases in the bunch: following Sacherer [29] equation, the effective impedance (including the indirect space charge) creates this defocusing effect. The vertical tune shift  $\Delta Q_y$  is more significant than the horizontal tune shift  $\Delta Q_x$  due to the elliptical shape of the PS beam chamber, making difficult a correct estimation of the horizontal effective impedance. For this reason we are going to show only the results of the measurement of vertical tune shifts. The measurements have been performed in several MD sessions, with a dedicated PS MD beam provided by a long plateau at the kinetic energy of 2 GeV, as shown in Fig. 3.1. The beam coming for the PS Booster is always a TOF-type beam, that allows very high values of intensity.

### 3.2.2 Intermediate energies

In order to have a better understanding of the transverse effective beam coupling impedance and the indirect space charge contributions, two intermediate energies of 7 and 13 GeV

TABLE 3.1: Beam parameters for tune shift measurements at kinetic energy of 2 GeV.

Kinetic energy [GeV]	2
Lorentz factor $\gamma_{rel}$	3.13
Slip factor $\eta$	-0.075
Harmonic number	8
Full bunch length $4\sigma$ [ns]	120

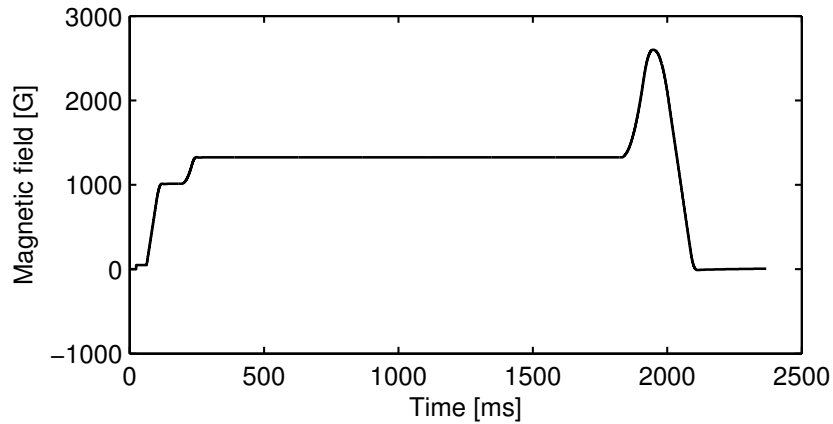


FIGURE 3.1: Magnetic field applied along the cycle used for tune shift measurements at 2 GeV.

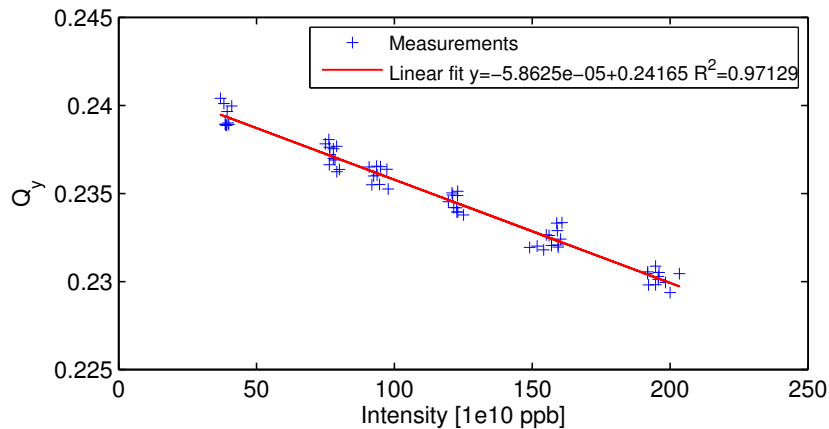


FIGURE 3.2: Vertical tune shift as a function of beam intensity measured at 2 GeV.

have been considered for tune shift measurements. The single bunch beams parameters are summarized in Tables 3.2 and 3.3. The measured vertical tune shifts as a function of the beam intensity are shown in Fig. 3.3 and 3.4. The measurements have been performed in several MD sessions on a dedicated MD cycle with several long plateaux at different energies.

TABLE 3.2: Beam parameters for tune shift measurements at kinetic energy of 7.25 GeV.

Kinetic energy [GeV]	7.25
Lorentz factor $\gamma_{rel}$	8.72
Slip factor $\eta$	-0.013
Harmonic number	8
Full bunch length $4\sigma$ [ns]	55

TABLE 3.3: Beam parameters for tune shift measurements at kinetic energy of 13.09 GeV.

Kinetic energy [GeV]	13.09
Lorentz factor $\gamma_{rel}$	14.95
Slip factor $\eta$	0.022
Harmonic number	8
Full bunch length $4\sigma$ [ns]	155

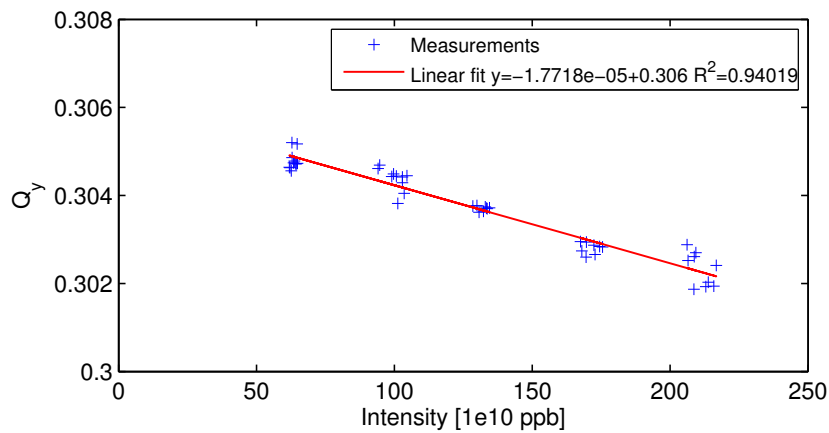


FIGURE 3.3: Vertical tune shift as a function of beam intensity measured at 7.25 GeV.

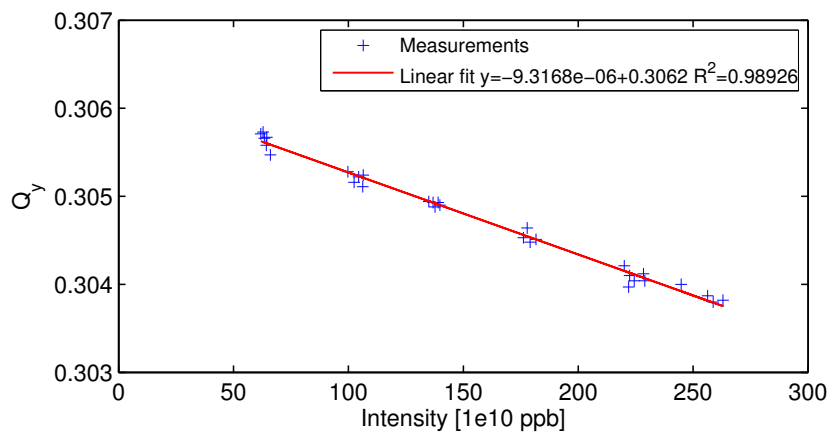


FIGURE 3.4: Vertical tune shift as a function of beam intensity measured at 13.09 GeV.

### 3.2.3 Extraction energy

In order to have a better understanding of indirect space charge contribution, the extraction energy of 25 GeV have been considered for tune shift measurements. In Table 3.4

TABLE 3.4: Beam parameters for tune shift measurements at kinetic energy of 25.48 GeV.

Kinetic energy [GeV]	25.48
Lorentz factor $\gamma_{rel}$	28.16
Slip factor $\eta$	0.052
Harmonic number	8
Full bunch length $4\sigma$ [ns]	45

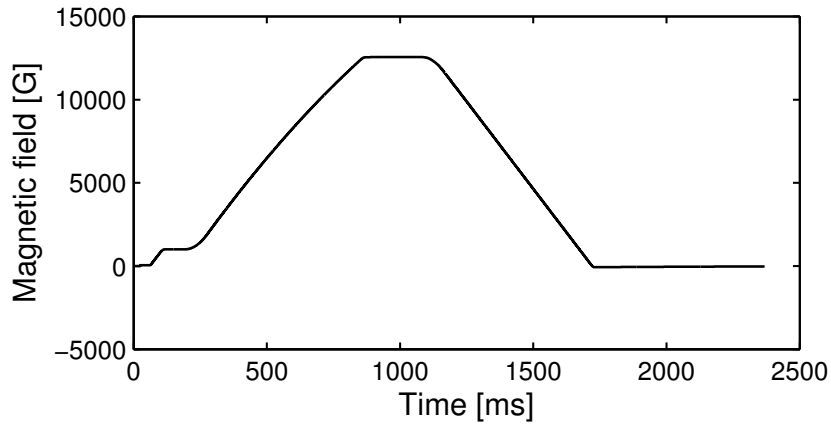


FIGURE 3.5: Magnetic field applied along the cycle used for tune shift measurements at 25 GeV.

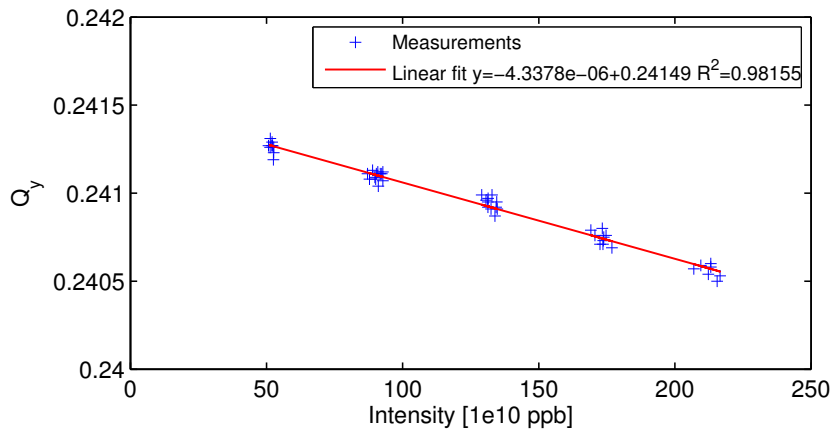


FIGURE 3.6: Vertical tune shift as a function of beam intensity measured at 25.48 GeV.

are summarized the single bunch beam parameters. The measured vertical tune shift as a function of the beam intensity is shown in Fig. 3.6. The measurements have been performed during several MD sessions on a dedicated MD cycle, cloned by the standard AD cycle, provided by a long extraction energy plateau, as shown in Fig. 3.5. The beam coming for the PS Booster is always a TOF-type, that allows very high values of intensity. In Table 3.5 are finally summarized the imaginary part of the vertical effective impedance measured at different energies and zero chromaticity.

TABLE 3.5: Imaginary part of the vertical effective impedance measured at different energies at zero chromaticity.

$E_{kin}$ [GeV]	$Z_y^{eff}$ [ $M\Omega/m$ ]	$4\sigma$ [ns]	$\xi_y$
2	$8.19 \pm 0.18$	120	-0.12
7.25	$3.51 \pm 0.13$	55	-0.02
13.09	$3.06 \pm 0.12$	55	-0.02
25.48	$2.23 \pm 0.05$	45	0.02

### 3.3 Tune shift measurements with chromaticity scan

Several MD sessions have been dedicated to investigate the changing in the imaginary part of the effective impedance with the vertical chromaticity. Measurements of the tune shift with beam intensity have been acquired at four energies, setting different vertical chromaticities on the machine working point. To perform this measurement, a vertical chromaticity value was initially set on the working point application. Vertical and horizontal tunes and horizontal chromaticity were kept to fixed value, far from possible resonances. The setting was then remotely sent through the working point application in the CERN control center to the PFW and to the figure-of-eight loop in the ring. A measurement of the vertical chromaticity was performed after each change in the working point to assess the effective value, that may not entirely corresponds to the one set on the working point application. Four sets of measurements were performed at the energies of 2, 7, 13 and 25 GeV. For each energy, about ten values of vertical chromaticity have been set on the working point and lately measured with a dedicated application. The possibility of pushing the chromaticity to values far from zero, as well setting a negative chromaticity for below transition energies, was limited by stability of the beam in the specific cycle and by the beam losses in the machine. After each chromaticity measurements, a tune shift scan with intensity was performed in order to calculate the effective vertical impedance for the given chromaticity. The four sets of tune shifts measurements, acquired of the flat energy plateaux of three different cycles, show the same increasing trend of the vertical effective impedance with the chromatic frequency. This behavior could be explained by the presence of an unidentified machine element with a significant resonance around 100 MHz in the beam coupling impedance. In Fig. 3.7 the impedance scan with chromatic frequency at different energies, is shown, where we can also identify the zero chromaticity impedances presented in the previous section.

### 3.4 Transverse impedance budget from simulations

In addition to impedance measurements, theoretical estimations based on numerical codes or analytical formulas have been performed in order to monitor and compare the impedance

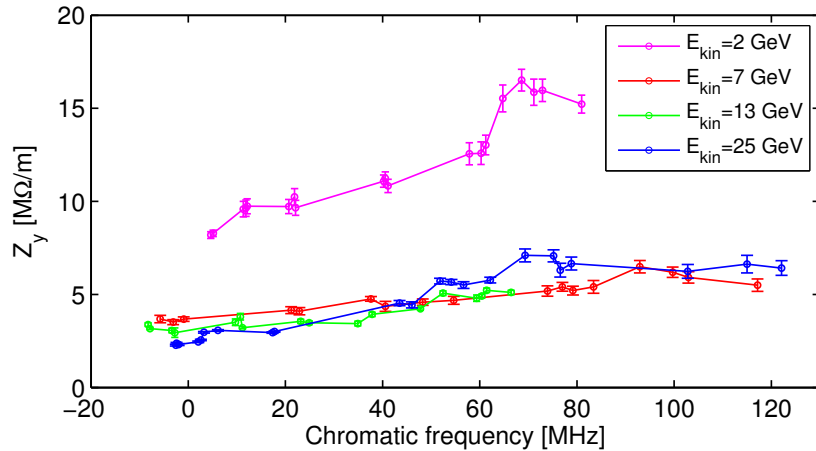


FIGURE 3.7: Imaginary part of the effective vertical impedance scan with chromatic frequency at different energies.

model with the measured impedance budget. The purpose of the study is to obtain an impedance budget that could explain the results from beam based measurements, by summing the transverse impedances of each machine element calculated analytically and with electromagnetic simulations: in this way we can compute the frequency dependence of the total machine impedance, and thereby the total effective impedances that would be expected by the model.

### 3.4.1 Indirect Space charge and resistive wall

The observed difference in the effective impedance in the vertical plane between tune shift measurements at different energies can be explained by the effect of the coherent indirect space charge, induced by a beam inside a perfectly conducting infinitely smooth beam pipe. Calculations were performed with the code described in [34]. A machine made of stainless steel 316 LN (about 70% of the total length) and of Inconel X750 alloy (about 20%) has been considered for resistive wall calculations. Both a round chamber model (35 mm radius) and parallel plates model have been taken into account. The transverse effective impedance obtained for the resistive wall case is very close for the two geometries: 0.29  $M\Omega/m$  for the round chamber and 0.35  $M\Omega/m$  for a parallel plates model. For the parallel plates, on the vertical plane, the dipolar and quadrupolar impedance contributions have the same sign: the total vertical impedance is therefore increased by a factor 1.2 with respect to the round chamber case. Instead, on the horizontal plane, the parallel plates model gives zero total impedance due to the perfect compensation of dipolar and quadrupolar components of the impedance. If we take into account also the indirect space charge contribution, approximating the PS elliptic beam chamber as two parallel plates, the contribution to the imaginary part of the total effective vertical impedance is 6  $M\Omega/m$  at 1.4 GeV and 3.7  $M\Omega/m$  at 2 GeV. If we consider a round chamber of 35 mm radius, the

TABLE 3.6: Indirect space charge and resistive wall contributions to the total vertical effective impedance at different kinetic energies for round chamber and parallel plates.

	1.4 GeV	2 GeV	25 GeV
Flat	6.0 $M\Omega/m$	3.7 $M\Omega/m$	< 0.5 $M\Omega/m$
Round r=35 mm	4.9 $M\Omega/m$	3.0 $M\Omega/m$	< 0.5 $M\Omega/m$

contribution is 4.9  $M\Omega/m$  and 3  $M\Omega/m$  for the two energies. At 25 GeV, the contribution to the impedance of the coherent indirect space charge becomes negligible. In Table 3.6 the results of the indirect space charge and resistive wall contributions are summarized. The total vertical impedance of the PS indirect space charge and resistive wall, calculated at 2 GeV in the round chamber case, is shown in Fig. 3.8. Approximating the elliptical PS chamber with a circular one, we obtain that the indirect space charge and resistive wall contribution explains about 36% of the total effective vertical impedance measured at 2 GeV.

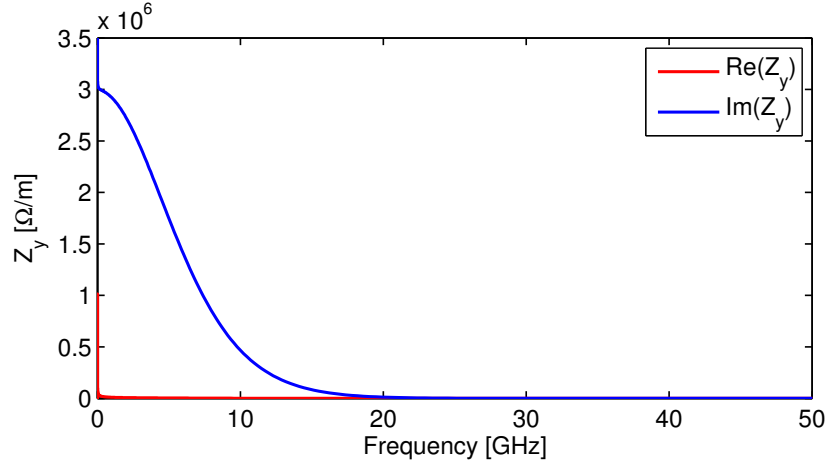


FIGURE 3.8: Total vertical impedance of the PS space charge and resistive wall calculated at 2 GeV for the round chamber case.

### 3.4.2 Kicker magnets

Kicker magnets are predicted to be a very important source of transverse impedance in the PS. CST Particle Studio [35] simulations, and calculations with the Tsutsui theoretical formula [36], have been performed for all the eleven PS kickers, showing very good agreement in the transverse and longitudinal plane. A comparison between simulations and measurements has also been done for the kicker KFA13 [37], revealing a good agreement, in particular on the vertical plane. Summing the total imaginary part of the transverse impedance (dipolar and quadrupolar contribution) obtained with CST Particle Studio for all the PS kickers, we obtain that their contribution to the machine impedance budget, weighted by the  $\beta$  function defined in the lattice and calculated at the energy of 2 GeV, is

less than  $0.03 \text{ M}\Omega/\text{m}$  in the horizontal plane, and about  $1.4 \text{ M}\Omega/\text{m}$  in the vertical plane. Kickers magnets can explain about the 17% of the vertical impedance measured at 2 GeV. In Fig. 3.9 and 3.10 the horizontal and vertical impedance models of the kickers is shown.

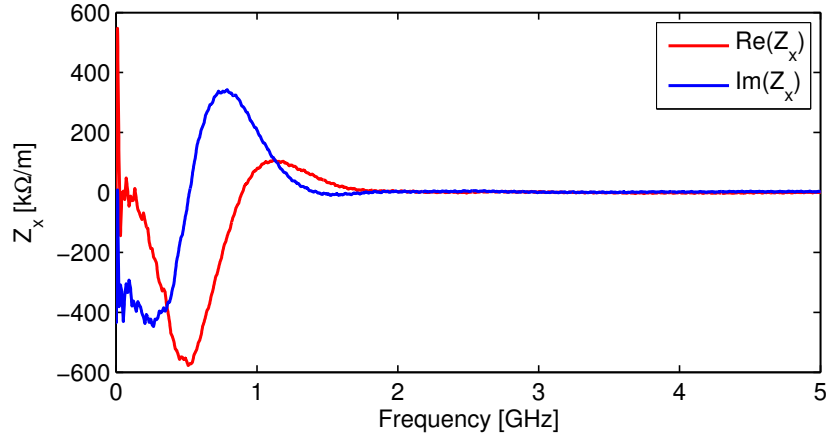


FIGURE 3.9: Total horizontal impedance of the PS kickers simulated with CST Particle Studio.

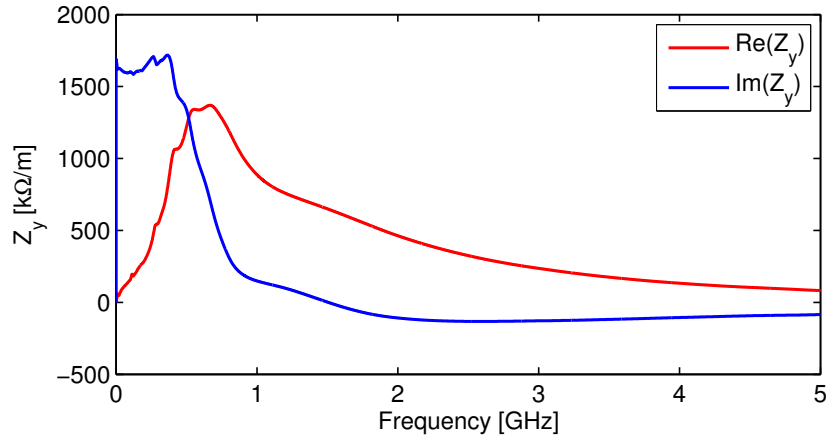


FIGURE 3.10: Total vertical impedance of the PS kickers simulated with CST Particle Studio.

### 3.4.3 RF cavities

Impedance studies and electromagnetic computations have been performed for the cavities installed in the PS. The current impedance budget includes the contribution of the 10 MHz, 40 MHz, 80 MHz, and the 200 MHz cavities, weighted by the  $\beta$  function defined in the lattice. 2D models of the 40 and 80 MHz cavity were first implemented with the code ABCI [38], starting from the design described in [39]. At a later stage, a 3D model

has been realized in CST Particle Studio. The models do not include couplers and tuning system of the cavities. In Fig. 3.11 the low frequency imaginary part of the vertical impedance is shown for the 10, 40 and 80 MHz cavities: the imaginary part is negative in agreement with CST Particle Studio convention. Results from simulations show that RF cavities do not have a strong impact on the transverse impedance and they can explain less than 1% of the vertical impedance measured at 2 GeV. As an output of the impedance studies, 3D models are currently available for the first time for almost all PS cavities.

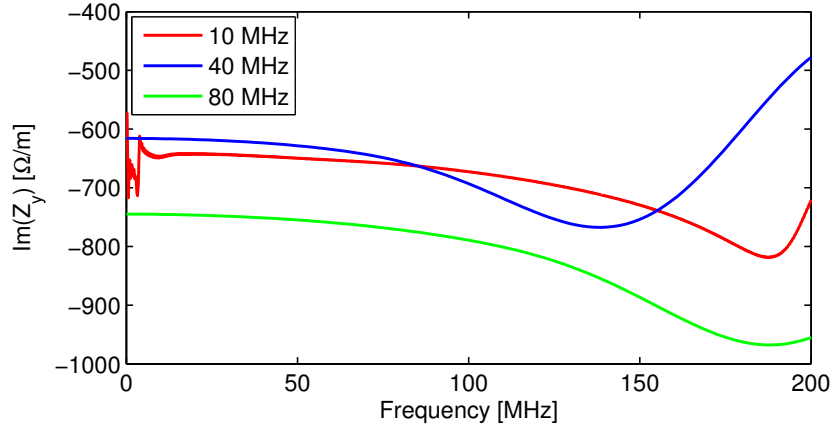


FIGURE 3.11: Imaginary part of the vertical impedance for the 10, 40 and 80 MHz cavities simulated with CST Particle Studio (CST output convention is negative for positive transverse impedances).

#### 3.4.4 Vacuum equipment

Vacuum equipment and features in the PS beam line like pumps, sector valves, bellows, steps and metallic (not isolated) flanges are included in the model as distributed elements, meaning that these impedances are not weighted by the  $\beta$  function defined in the lattice. Currently the impedance budget includes the contribution of many elements, summarized in Table 3.7. Even if the impedance of the single element is predicted to be small, the sum of many distributed elements can explain about 7% of the vertical impedance measured at 2 GeV. In Fig. 3.12 the low frequency imaginary part of the vertical impedance is shown the valves, bellows, pumps and steps, while in Fig. 3.13, the low frequency imaginary part of the vertical impedance for metallic flanges, is shown. The imaginary part is negative in agreement with CST Particle Studio convention.

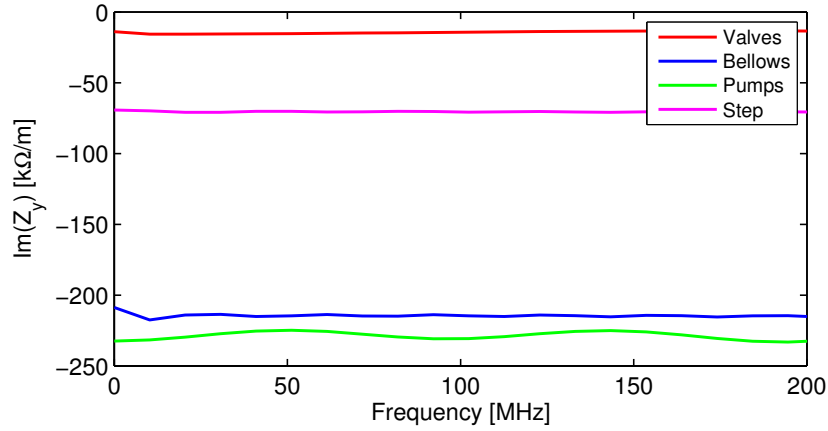


FIGURE 3.12: Imaginary part of the vertical impedance of bellows (273 elements), vacuum pumps (100 elements) and sector valves (10 elements) simulated with CST Particle Studio.

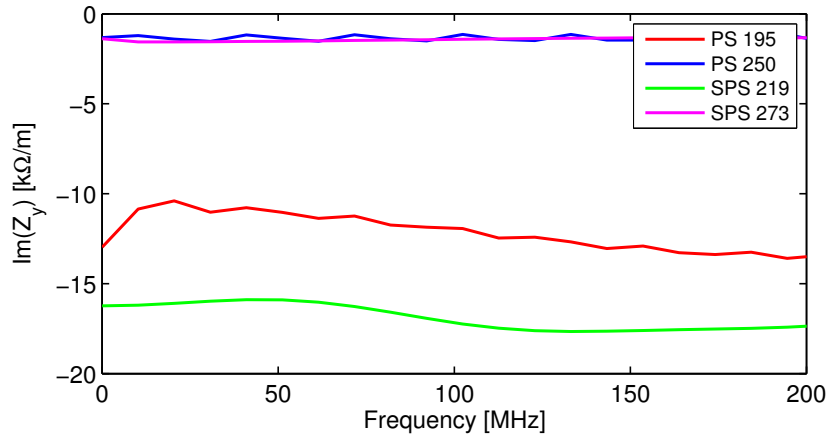


FIGURE 3.13: Imaginary part of the vertical impedance of PS metallic not isolated flanges simulated with CST Particle Studio.

TABLE 3.7: Effective horizontal and vertical impedances calculated for vacuum equipment.

	Number of elements	$Z_x^{eff}$ [ $M\Omega/m$ ]	$Z_y^{eff}$ [ $M\Omega/m$ ]
Vacuum pumps	100	0.003	0.232
Bellows	237	0.011	0.208
Step transitions	60	0.040	0.070
Sector valves	10	0.004	0.015
Metallic flange PS 195	33	0.003	0.010
Metallic flange PS 250	5	0	0.001
Metallic flange SPS 219	2	0.001	0.016
Metallic flange SPS 273	4	0	0.001

## Conclusions

In this chapter we described the PS transverse impedance model evaluated with beam based measurements and numerical simulations. Measurements of the vertical and horizontal tune shift as a function of beam intensity provide a value for the horizontal and

TABLE 3.8: Contribution to the vertical effective impedance budget measured at 2 GeV of the machine elements.

	$Z_y^{eff}$ [ $M\Omega/m$ ]	Percentage
Space charge	3	36 %
Resistive wall	0.3	3.5 %
Kickers	1.4	17%
Vacuum	0.55	6.7%
Cavities	0.8	1 %

vertical imaginary part of the effective impedance at different energies. At zero chromaticity the measured vertical impedance is 8.2  $M\Omega/m$  at injection energy and 2.2  $M\Omega/m$  at extraction energy. This represents the vertical impedance budget of the machine at a given energy. The difference in the two sets of measurements can be explained by the effect of the indirect space charge. A scan of the imaginary part of the vertical impedance with chromaticity has been performed, revealing an increasing trend with chromaticity for all the set of measurements at different energies. These results, if confirmed, would suggest the presence of an undefined machine elements introducing a low frequency resonance, that was not yet predicted with simulations. The measured transverse effective impedance has been compared with numerical simulations, performed for the single machine elements 3D models implemented in CST Particle Studio. Resistive wall and indirect space charge impedance were studied with the help of available analytical and numerical codes. The current impedance model, built during this work and obtained with simulations, accounts for the 65% of the vertical impedance obtained with tune shift measurements at the energy of 2 GeV. The contribution of the elements is summarized in Table 3.8. The 35% missing could come from the isolated flanges connected to RF bypass, from beam instrumentation and/or from electrical and power connections in the machine. The total PS wake functions is shown in Fig. 3.14, while the total transverse impedance model is shown in Fig. 3.15.

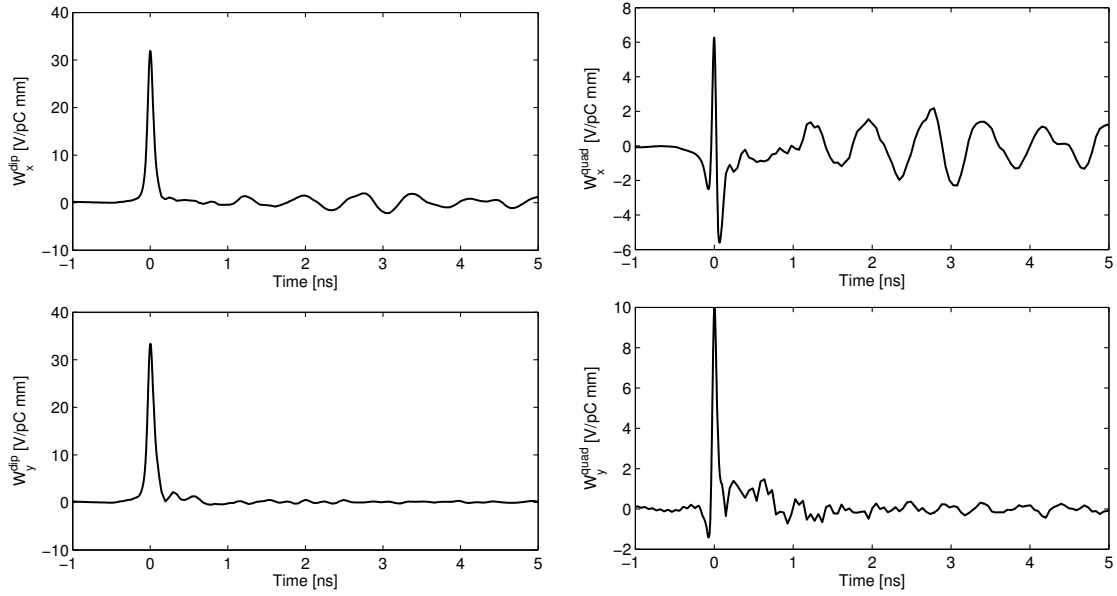


FIGURE 3.14: Horizontal and vertical dipolar and quadrupolar components of the PS wake function.

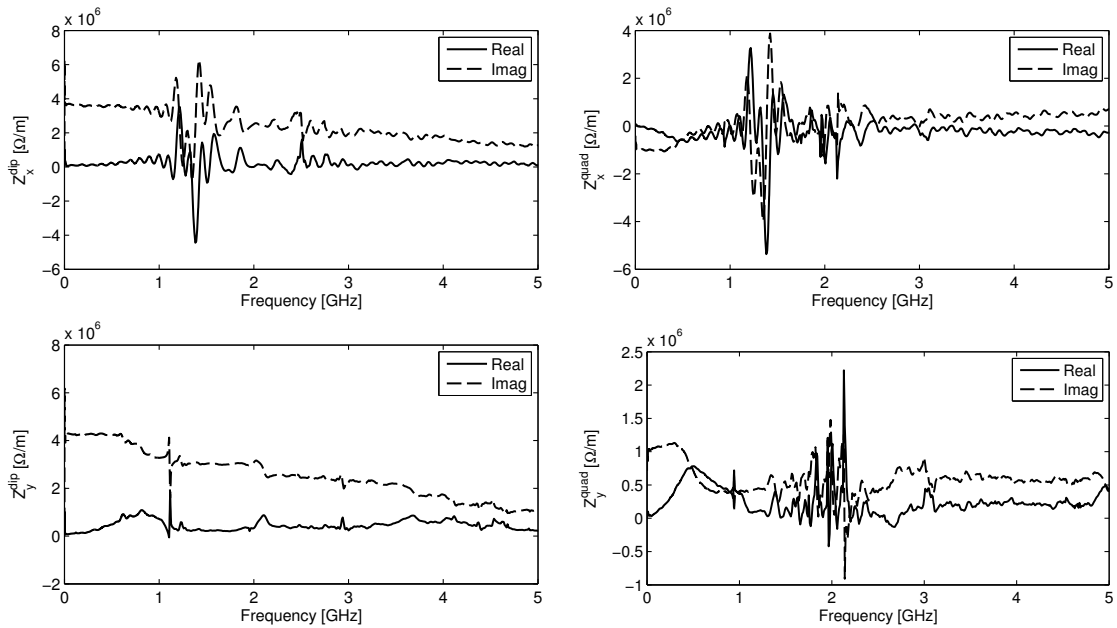


FIGURE 3.15: Horizontal and vertical dipolar and quadrupolar components of the PS impedance model.



## Chapter 4

# The PS longitudinal impedance model

The knowledge of the longitudinal beam coupling impedance model of the PS is of fundamental importance in the frame of the LHC Injector Upgrade program to understand the limitation in terms on longitudinal instabilities of the machine. As in the case of the transverse impedance model determination, shown in Chapter 3, the measured longitudinal coupling impedance can be compared to the theoretical impedance obtained calculating the contributions of each relevant component installed in the machine with simulation and numerical estimations. The determination of the PS longitudinal broadband impedance was addressed for the first time in the late '70, where a measurements campaign, based on longitudinal stability during debunching and on quadrupole beam transfer functions, showed a longitudinal impedance of about  $25 \Omega$  [40] [41]. Nevertheless, this study has been approached again in 2012, when important hardware changes and new devices installations were foreseen in the coming two years. The aim of the 2012 longitudinal impedance studies were in fact to establish an accurate budget to predict the impedance contribution of the new elements to be installed and identify the main sources of longitudinal impedance in the machine.

### 4.1 Measurements of quadrupole synchrotron frequency

Measurements of quadrupole synchrotron frequency at a fixed momentum of 26 GeV/c and single-harmonic of 40 MHz were performed in order to establish the imaginary part of the longitudinal broadband impedance of the PS [17] [42]. A single bunch with an intensity of  $N_p = 4.5 \cdot 10^{11}$  protons was injected from the PS Booster and accelerated in the PS on the harmonic  $h=16$  of the revolution frequency to a momentum of 26 GeV/c. On the

flat-top, the bunch was first synchronized to a fixed revolution frequency of 476.82 kHz, allowing to pulse a higher-harmonic RF cavity at 40 MHz, that is the harmonic  $h=84$  of the revolution frequency. The bunch was handed over from  $h=16$  (7.629 MHz) to  $h=84$  (40.052 MHz) about 150 ms before extraction. This rebucketing to the 40 MHz RF system was completed 140 ms before extraction. Aside from a 5 ms time window for longitudinal emittance measurements, about 130 ms were left under stationary conditions to perform the beam transfer function (BTF) measurement. During that time, the bunch was held with a constant 40 MHz RF voltage of about 50 kV or 100 kV at  $h=84$ .

#### 4.1.1 Quadrupole synchrotron frequency measurement setup

The spectrum of the incoherent quadrupole synchrotron frequency has been obtained by measurement of the longitudinal BTF with the set-up sketched in Fig. 4.1. A bandwidth

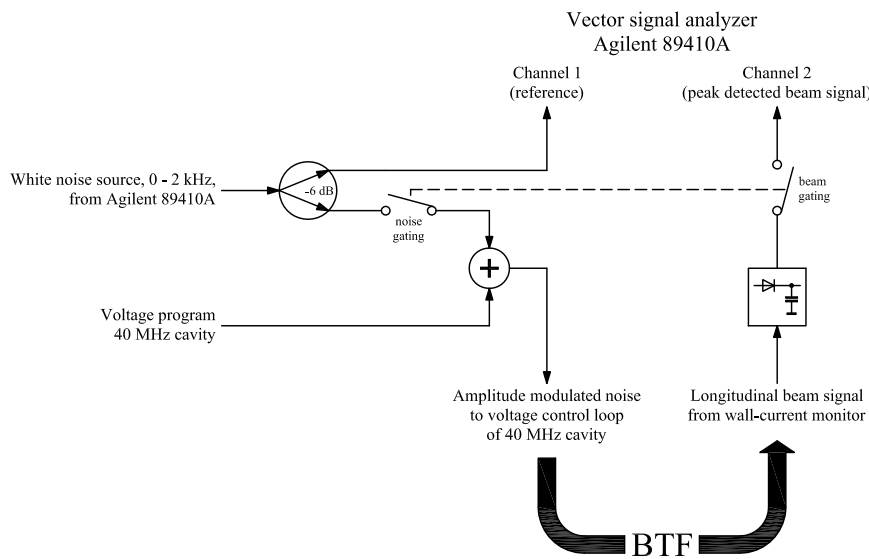


FIGURE 4.1: Longitudinal quadrupole beam transfer function (BTF) measurement setup.

limited white noise (up to 2 kHz) was generated by the internal source of an Agilent 89410A Vector Network Analyser (VNA). The bandwidth was chosen to fully cover the quadrupole synchrotron frequency and to achieve the best possible resolution within the 30 ms time window for the measurements. The noise signal was gated in order to affect only the beam during the well-defined duration of the measurement and was added as an amplitude modulation to the voltage program of the 40 MHz cavity. The peak amplitude of the noise was independent of the voltage in the 40 MHz cavity. A copy of the noise signal used for amplitude modulation was directly fed to the reference channel of the VNA. A combination of a wall current monitor (WCM) followed by a peak detector have been used to measure the longitudinal beam signal. The attenuation of the beam signal was chosen to get optimum signal amplitude to the peak detection circuit and

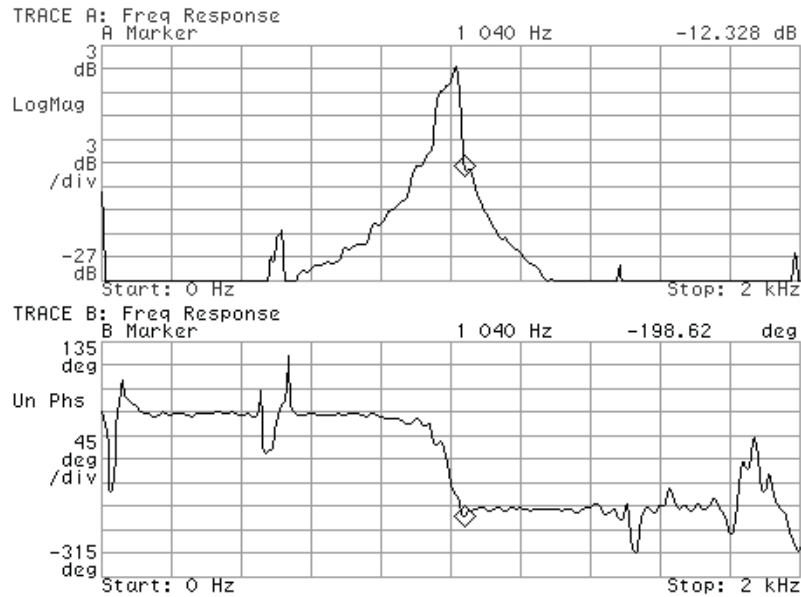


FIGURE 4.2: Amplitude and phase of the quadrupole BTF for a bunch of  $9 \cdot 10^{10}$  particles kept by 95 kV at 40 MHz.

avoid saturation. The peak-detected beam signal was then fed to the second channel of the VNA (see Fig. 4.1). Amplitude and phase of the quadrupole BTF are then read on the VNA by calculating the vectorial ratio of peak-detected beam signal and noise excitation, averaging measurements on many acceleration cycles. A typical quadrupole synchrotron frequency spectrum is shown in Fig. 4.2. The zero-amplitude quadrupole synchrotron frequency is given by the discontinuity of the phase curve following the  $180^\circ$  phase advance. The small peak in both amplitude and phase, at half that frequency, is a direct observation of the synchrotron frequency due to residual oscillations.

#### 4.1.2 Longitudinal impedance from measurements

Two series of single bunch measurements were performed during two different MD sessions using different peak voltages, while the momentum of 26 GeV/c was chosen to minimize the effects of space charge. Each measurement was taken by averaging over 16 acceleration cycles with approximately the same intensity and longitudinal emittance. Longitudinal bunch shapes were also acquired during measurements. Two different types of fit (Gaussian or parabolic) were used to determine the bunch length from the shape. Both models fit well the measured bunch profile. To extract the low-frequency longitudinal impedance, we need to introduce the longitudinal equation of motion of a single particle in presence

of the self-induced wakefields [43]:

$$\ddot{\tau} + \omega_{s0}^2 \tau = \frac{eN_p \omega_{s0}^2}{2\pi V_{RF} h \cos \phi_s} \sum_{p=-\infty}^{\infty} Z(p\omega_0) \sigma_0(p\omega_0) e^{ip\omega_0 \tau}, \quad (4.1)$$

where  $\tau$  is the position of the particle with respect to the synchronous one,  $\omega_{s0}$  the natural synchrotron frequency,  $h$  the harmonic number,  $\phi_s$  the synchronous phase ( $\cos \phi_s < 0$  above transition),  $\omega_0$  the revolution frequency,  $Z(\omega)$  the longitudinal broadband impedance, and  $\sigma_0(\omega)$  the bunch spectrum of the stationary distribution. For a Gaussian distribution with standard deviation  $\sigma_G$ , the bunch spectrum is given by

$$\sigma_0(\omega) = e^{-\frac{\omega^2 \sigma_G^2}{2}}, \quad (4.2)$$

whereas, for a parabolic line density of total length  $\tau_b$ , it is given by

$$\sigma_0(\omega) = 3 \frac{\sin(\omega\tau_b/2) - \omega\tau_b/2 \cos(\omega\tau_b/2)}{(\omega\tau_b/2)^3}. \quad (4.3)$$

In the absence of wakefields, a linear synchrotron motion is assumed. In that situation, RF voltage is linear within the bunch duration and all the particles oscillate at the same frequency  $\omega_{s0}$  independently of their amplitude. The effect of stationary wakefields is to introduce an incoherent synchrotron frequency shift in the synchronous phase, and other non-linear terms that produce a synchrotron frequency spread. This can be easily understood expanding the term  $e^{ip\omega_0 \tau}$  [43]:

$$\ddot{\tau} + \omega_{s0}^2 \tau = \frac{eN_p \omega_{s0}^2}{2\pi V_{RF} h \cos \phi_s} \sum_{p=-\infty}^{\infty} Z(p\omega_0) \sigma_0(p\omega_0) \left( 1 + ip\omega_0 \tau - \frac{(p\omega_0 \tau)^2}{2} + \dots \right). \quad (4.4)$$

The constant term on the right side of Eq. (4.4) produces a phase shift in combination with the real part of the impedance, which is an even function of the frequency, and it is given by

$$\Delta\phi = h\omega_0 \Delta\tau = \frac{eN_p \omega_0}{2\pi V_{RF} \cos \phi_s} \sum_{p=-\infty}^{\infty} \text{Re} [Z(p\omega_0)] \sigma_0(p\omega_0). \quad (4.5)$$

The phase shift given by the above expression is based on the linear expansion of the equation of motion and has to be considered as an approximation. In fact, if we use, for example, a broadband resonator characterized by a shunt resistance  $R_s$ , a quality factor  $Q$  and a resonant frequency  $\omega_r$ , with a Gaussian distribution, by replacing the summation with an integral, we obtain

$$\Delta\phi = \frac{\pi e N_p R_s}{V_{RF} \cos \phi_s \sqrt{Q^2 - 1/4}} \text{Re} \left[ \omega_1 e^{-\frac{\omega_r^2 \sigma_G^2}{2}} \text{Erf} \left( -i \frac{\omega_r \sigma_G}{\sqrt{2}} \right) \right], \quad (4.6)$$

where

$$\omega_1 = \frac{\omega_r}{Q} \left( \frac{i}{2} + \sqrt{Q^2 - \frac{1}{4}} \right). \quad (4.7)$$

By using instead the loss factor of a Gaussian bunch coupled with a resonator impedance [44], the correct synchronous phase shift is slightly modified as

$$\Delta\phi = \frac{eN_p R_s}{2V_{RF} \cos\phi_s \sqrt{Q^2 - 1/4}} \operatorname{Re} \left[ \omega_1 e^{-\omega_r^2 \sigma_G^2} \operatorname{Erf}(-i\omega_r \sigma_G) \right]. \quad (4.8)$$

Equation (4.4) can also be used to obtain an approximate expression of the incoherent synchrotron frequency shift. In fact, if we consider the first order term in  $\tau$  of Eq. (4.4), the oscillation frequency of a particle in the bunch becomes

$$\omega_s^2 = \omega_{s0}^2 \left( 1 + \frac{eN_p \omega_0}{2\pi V_{RF} h \cos\phi_s} \sum_{p=-\infty}^{\infty} \operatorname{Im}[Z(p\omega_0)] p \sigma_0(p\omega_0) \right), \quad (4.9)$$

that is

$$\frac{\omega_s^2 - \omega_{s0}^2}{\omega_{s0}^2} = \frac{eN_p \omega_0}{2\pi V_{RF} h \cos\phi_s} \sum_{p=-\infty}^{\infty} \operatorname{Im}[Z(p\omega_0)] p \sigma_0(p\omega_0). \quad (4.10)$$

If the incoherent frequency shift is small compared to the unperturbed synchrotron frequency we obtain

$$\frac{\omega_s - \omega_{s0}}{\omega_{s0}} = \frac{\Delta\omega_s}{\omega_{s0}} = \frac{\Delta f_s}{f_{s0}} \simeq \frac{eN_p \omega_0}{4\pi V_{RF} h \cos\phi_s} \sum_{p=-\infty}^{\infty} \operatorname{Im}[Z(p\omega_0)] p \sigma_0(p\omega_0). \quad (4.11)$$

In the case of a pure inductive broadband impedance, we finally obtain

$$\frac{\Delta f_s}{f_{s0}} = \frac{eN_p \omega_0}{4\pi V_{RF} h \cos\phi_s} \frac{\operatorname{Im}[Z(p)]}{p} \sum_{p=-\infty}^{\infty} p^2 \sigma_0(p\omega_0), \quad (4.12)$$

which relates the incoherent dipole synchrotron frequency to the inductive machine impedance  $\operatorname{Im}[Z(p)]/p$ . We finally obtain the following expression for the quadrupole frequency:

$$\frac{\Delta f_{2s}}{f_{s0}} = \frac{eN_p \omega_0}{2\pi V_{RF} h \cos\phi_s} \frac{\operatorname{Im}[Z(p)]}{p} \sum_{p=-\infty}^{\infty} p^2 \sigma_0(p\omega_0). \quad (4.13)$$

As for the synchronous frequency shift, if we consider a Gaussian distribution, and approximate the summation with an integral, we get

$$\frac{f_{2s}}{f_{s0}} = 2 + \frac{eN_p}{\sqrt{2\pi} V_{RF} h \cos\phi_s \omega_0^2 \sigma_G^3} \frac{\operatorname{Im}[Z(p)]}{p} = 2 - \tilde{X} \frac{\operatorname{Im}[Z(p)]}{p}. \quad (4.14)$$

The normalized incoherent quadrupole synchrotron frequency as a function of  $\tilde{X}$  for the two sets of measurements are shown in Fig. 4.3 and 4.4. The slope of the linear regression,

obtained with the method of least squares, gives directly the broadband longitudinal impedance of the machine  $Im[Z(p)]/p = (9.1 \pm 2.1) \Omega$  and  $Im[Z(p)]/p = (11.3 \pm 1.9) \Omega$ , respectively. In order to obtain an exact solution of the equation of motion (4.1), a

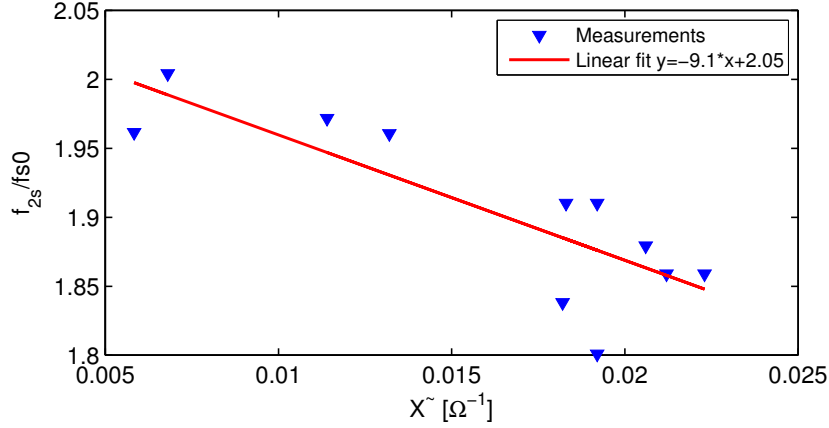


FIGURE 4.3: Quadrupole frequency shift and linear fit with Gaussian distribution function for the first set of measurements.

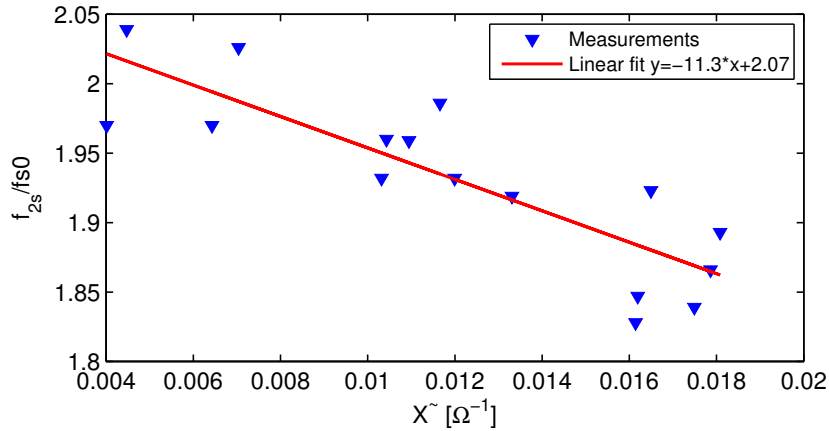


FIGURE 4.4: Quadrupole frequency shift and linear fit with Gaussian distribution function for the second set of measurements.

parabolic line density interacting with a pure inductive impedance was considered. In this case the infinite summation on the right side of Eq. (4.1) can be expressed in closed form

$$\sum_{p=-\infty}^{\infty} p\sigma_0(p\omega_0)e^{ip\omega_0\tau} = i\frac{3\pi\tau}{\omega_0^2(\tau_b/2)^3}, \quad (4.15)$$

and it gives a coherent force linear with  $\tau$ , such that the single particle equation of motion can be reduced to

$$\ddot{\tau} + \omega_{s0}^2\tau = -\frac{3eN_p\omega_{s0}^2}{2V_{RF}h \cos \phi_s \omega_0^2(\tau_b/2)^3} \frac{Im[Z(p)]}{p} \tau, \quad (4.16)$$

which gives a quadrupole synchrotron frequency shift of

$$\frac{f_{2s}}{f_{s0}} = 2 + \frac{12eN_p}{V_{RF}h \cos \phi_s \omega_0^2 \tau_b^3} \frac{Im[Z(p)]}{p} = 2 - \tilde{X} \frac{Im[Z(p)]}{p}. \quad (4.17)$$

If we compare Eq. (4.14) with Eq. (4.17), by considering  $\tau_b \simeq 4\sigma_G$ , we observe that the parabolic line density, with the exact solution of the equation of motion, predicts a frequency shift about two times less than the one obtained with the first order expansion and a Gaussian distribution. This factor two has also been found in [43]. The normalized synchrotron frequencies versus  $\tilde{X}$  when applied a parabolic fit to the measured bunch profiles are shown in Fig. 4.5 and 4.6. The longitudinal broadband impedance is estimated to be  $Im[Z(p)]/p = (17.6 \pm 3.6) \Omega$  and  $Im[Z(p)]/p = (21.0 \pm 4.0) \Omega$ .

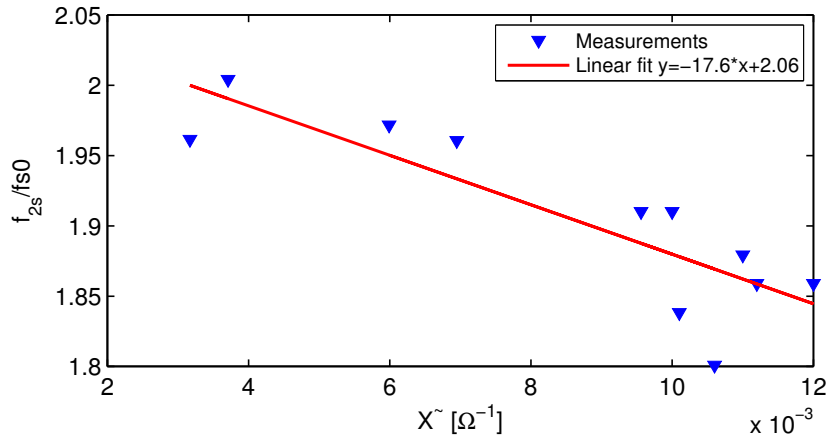


FIGURE 4.5: Quadrupole frequency shift and linear fit with parabolic line density for the first set of measurements.

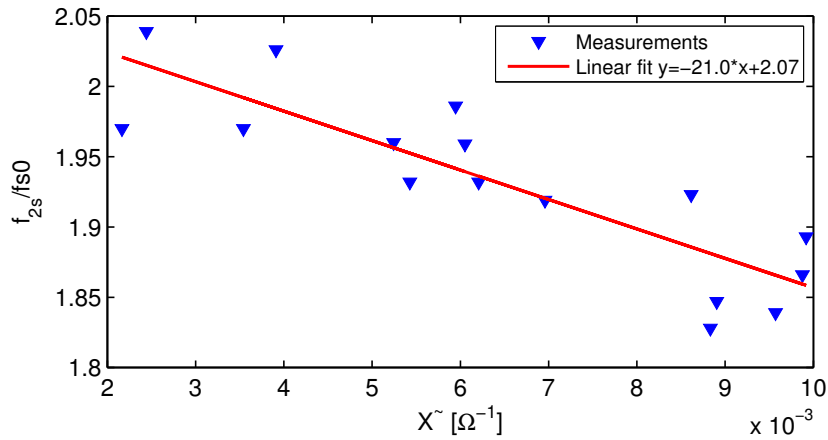


FIGURE 4.6: Quadrupole frequency shift and linear fit with parabolic line density for the second set of measurements.

## 4.2 Longitudinal impedance budget from simulations

### 4.2.1 Space charge

Measuring at the kinetic energy of 25 GeV allowed to reduce the contribution of the direct space charge to the broadband impedance, that has a capacitive effect above transition. The space charge impedance due to the non relativistic velocity of the charges ( $v = \beta c$ ) in a circular pipe of radius  $b$  can be written in the form [3]

$$\frac{Z(p)}{p} = -i \frac{Z_0}{\beta \gamma^2} g_l, \quad (4.18)$$

where  $Z_0=377 \Omega$  is the impedance of the free space,  $\gamma$  is the relativistic Lorentz factor, and  $g_l$  is a geometric constant depending on the transverse bunch distribution. In particular, for a uniform disk distribution of radius  $a$  we obtain

$$g_l = \ln \frac{b}{a} + \frac{1}{2}. \quad (4.19)$$

In case of the PS elliptic vacuum chamber, we substitute  $b$  with an equivalent radius of 43 mm. The contribution to the total broadband impedance due to the direct space charge at the kinetic energy of 25 GeV is about  $2 \Omega$ , the same order of magnitude as the uncertainty of the measurement results.

### 4.2.2 Resistive wall

For a circular pipe of radius  $b$  with high conductivity  $\sigma_c$ , such that  $c^2/(\omega^2 b)$  and  $b$  bigger than the skin depth  $\delta$ , the longitudinal coupling impedance is given by the following formula:

$$\frac{Z(p)}{p} = \frac{Z_0 \delta}{2b} [1 + i \cdot \text{sgn}(\omega)]. \quad (4.20)$$

For the elliptic vacuum chamber case,  $b$  represents the minor semi-axis, while the impedance is multiplied by a form factor that depends on the ellipticity of the beam pipe. For the PS case, the form factor is estimated to be 0.96. The skin depth depends on the pipe material: stainless steel 316 LN with conductivity  $\sigma_c = 1.3 \cdot 10^6$  S/m was considered for 70% of the machine and Inconel X750 alloy with conductivity  $\sigma_c = 8.3 \cdot 10^5$  S/m for about 20% of the machine. The impedance contribution due the resistive wall is shown in fig. 4.7 for both materials as a function of frequency. The impedance calculated at the machine revolution frequency is  $Z(p)/p=2.2(1+i) \Omega$  for stainless steel 316 LN, and  $Z(p)/p=0.8(1+i) \Omega$  for Inconel X750 alloy.

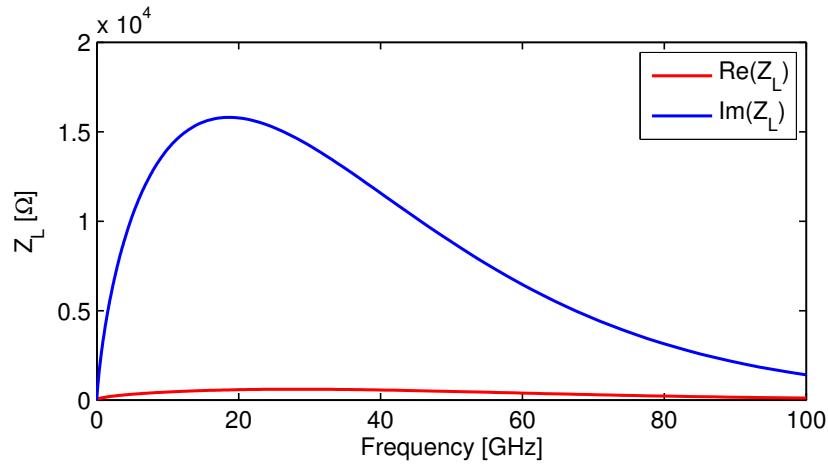


FIGURE 4.7: Resistive wall impedance for the PS vacuum chamber.

### 4.2.3 Kickers

A very important contribution to the total longitudinal PS impedance is given by the eleven ferrite loaded kickers. The longitudinal impedance has been evaluated with CST Microwave Studio [35] simulations and compared with Tsutsui theoretical formula [36]. The sum of kickers longitudinal impedances, shown in Fig. 4.8, represents a good approximation of the longitudinal impedance model of the machine.

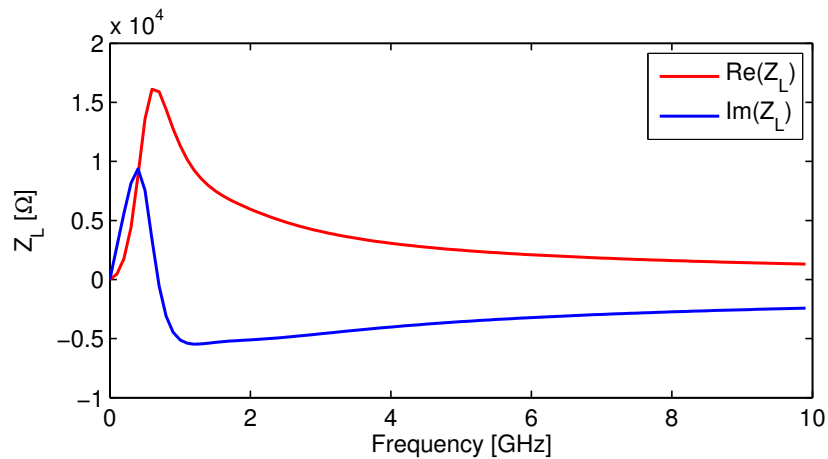


FIGURE 4.8: Total longitudinal impedance of the PS kickers.

### 4.2.4 Vacuum equipment

As for the transverse impedance model described in Chapter 3, some vacuum equipment like vacuum pumps, bellows and step transition are included in the longitudinal impedance model. The devices have been simulated with CST Particle Studio and the impedance of the single object has been multiplied for the number of elements installed in the machine.

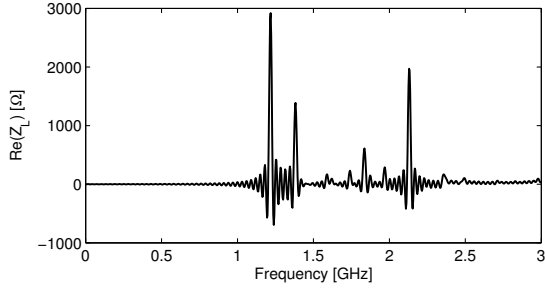


FIGURE 4.9: Real part of longitudinal impedance of a vacuum pump.

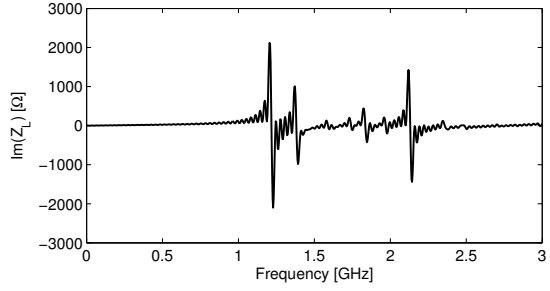


FIGURE 4.10: Imaginary part of longitudinal impedance of a vacuum pump.

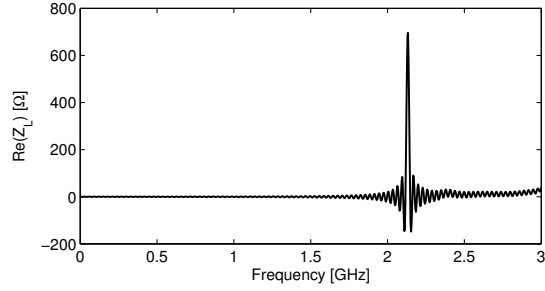


FIGURE 4.11: Real part of longitudinal impedance of a bellow.

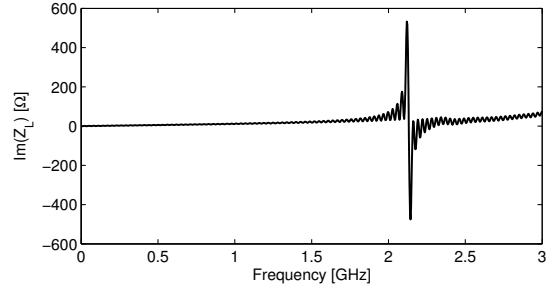


FIGURE 4.12: Imaginary part of longitudinal impedance of a bellow.

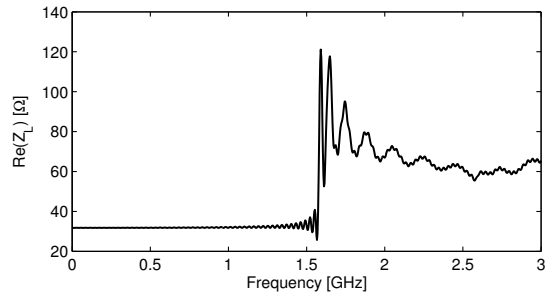


FIGURE 4.13: Real part of longitudinal impedance of a step transition.

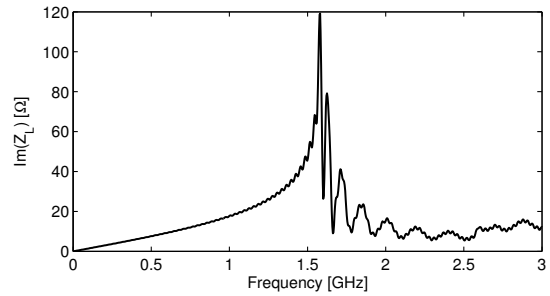


FIGURE 4.14: Imaginary part of longitudinal impedance of a step transition.

The connection region between the beam pipe and the vacuum pump give an important contribution to the geometrical impedance. Indeed the connection is not a simple hole, and there and the port of the pumps are not provided by RF shielding. Moreover, the length of the cylindrical pipe connecting the beam pipe to the vacuum pump does not affect, at first order, the coupling impedance. At low frequencies, the imaginary part of the longitudinal impedance is purely inductive and gives a contribution of  $Z(p)/p=2.8 \Omega$  (accounted for 100 elements). In Figures 4.9 and 4.10 is show the longitudinal impedance of a vacuum pump.

For the calculation of the longitudinal coupling impedance of The PS bellows, we considered the following formula, valid for a pillbox of width  $w$  much lower that the height  $h$ :

$$\frac{Z(p)}{p} = i \frac{n_c \omega_0 Z_0}{2\pi b c} \left( wh - \frac{w^2}{2\pi} \right), \quad (4.21)$$

with  $n_c$  the number of corrugations per bellow. We have assumed  $w = 3$  mm,  $h = 14$  mm, 8 corrugations per bellow, and approximately 200 elements. At low frequencies, the imaginary part of the longitudinal impedance is purely inductive and, considering a circular pipe cross section, is about  $Z(p)/p=1.1 \Omega$ . This results has been compared with CST Particle Studio simulations, that gave a total inductive impedance of  $Z(p)/p = 0.85 \Omega$ , very close to the one evaluated by using the analytic formula. The longitudinal impedance of a bellow is show in Figures 4.11 and 4.12. An important source of geometrical longitudinal impedance is given by step transitions between chamber of elliptical and circular cross-section. Simulations with CST Particle Studio gave an impedance of  $Z(p)/p=0.96 \Omega$  (about 60 transitions considered in calculation). The longitudinal impedance of a step transition between an elliptical pipe of vertical aperture of 35 mm a cylindrical pipe of radius 73 mm is show in Figures 4.13 and 4.14.

#### 4.2.5 RF cavities

Electromagnetic computations have been performed for some of the cavities installed in the PS; in Table 4.1 are summarized fundamental mode resonance parameters for all the cavities included in the longitudinal model. Bench measurements have been performed

TABLE 4.1: RF cavities fundamental mode resonance parameters.

Frequency (MHz)	Q	R/Q	Number
7.6	5	30	10
20	4.6	43.5	1
40	70	33	1
80	100	56	2

for the 200 MHz to verify the resonance parameters for different configurations of the diodes. The measurements have been performed during the shutdown connecting one of the cavities installed in the ring with a VNA, that allows to measure the transmission scattering parameter  $S_{21}$  and calculate the loaded quality factor  $Q_L$  and the main resonance frequency. Since the 200 MHz cavities have no mechanical system to close the gaps, each of them is equipped with three  $\lambda/4$  lines with PIN diodes in parallel to termination resistors at their ends. When the PIN diodes are in an open status, the three lines just couple the terminations to the cavity, significantly reducing it's quality factor. When the PIN diodes are in a closed status, their short circuit is transformed to a high impedance at the coupling surface to the cavity and the cavity has a high quality factor when in use. The amplitude of  $S_{12}$  of the fundamental mode with reversed diodes (open status) is shown in Fig. 4.15: in this case, when the cavity is able to see all the three loads, the quality factor is  $Q_L = 134$  at a frequency of 200.7 MHz. The amplitude of  $S_{12}$  of the

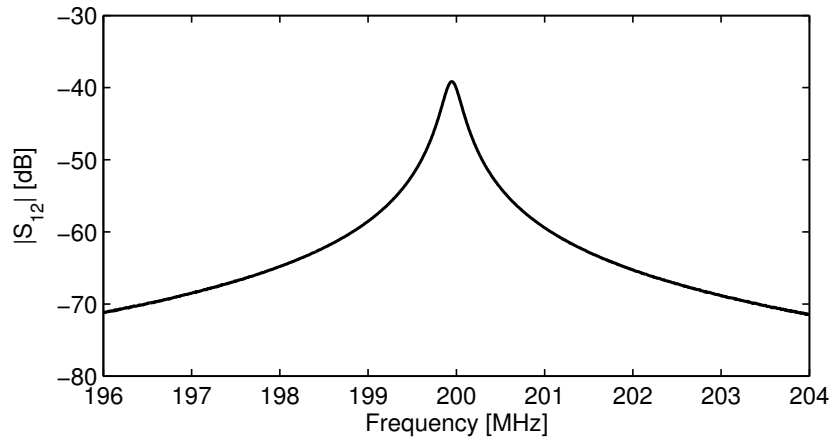


FIGURE 4.15: Amplitude of  $S_{12}$  of the fundamental mode of the 200 Mhz cavity with reversed diodes measured with VNA.

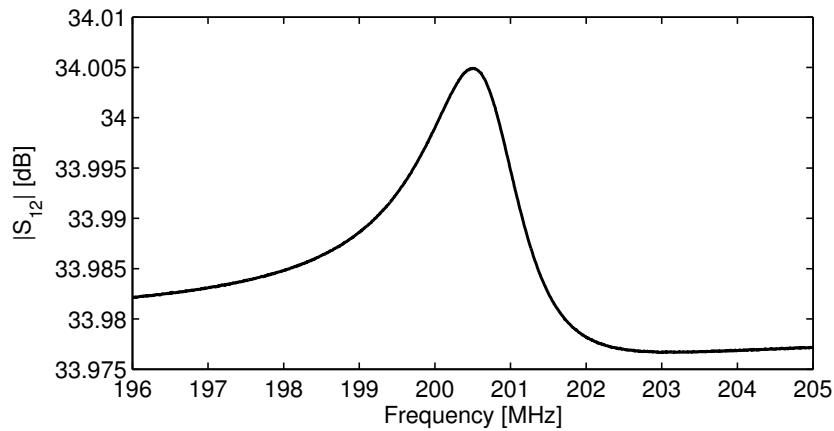


FIGURE 4.16: Amplitude of  $S_{12}$  of the fundamental mode of the 200 Mhz cavity with short circuited diodes measured with VNA.

fundamental mode with short circuited diodes is shown in Fig. 4.16: the quality factor is  $Q_L = 971$  at a frequency of 199.9 MHz. In both cases the quality factor is in agreement with the design parameters of the cavity. As for the transverse case, results from simulations show that RF cavities do not have a strong impact on the longitudinal coupling impedance and their contribution to the broadband impedance is mainly resistive.

## Conclusions

The longitudinal beam coupling impedance model of the CERN PS has been developed with beam based measurements, simulations, RF measurements, analytical formula. The measurement of the incoherent quadrupole frequency shift as a function of the single bunch intensity provided the inductive broadband longitudinal coupling impedance. The longitudinal budget of  $Z(p)/p = 18.4 \pm 2.2 \Omega$  is in agreement with measurements performed on the machine about 10 years ago. An analysis of several contributors to the total

broadband impedance like kicker magnets, RF cavities, vacuum equipment, resistive wall and space charge resulted in excellent agreement with the measurement, explaining almost the 90% of the measured longitudinal impedance. The different machine contributions are summarized in Table 4.2. The wake potential, calculated from the inductive impedance and shown in Fig. 4.17, can be used as input in beam dynamics simulations of the PS.

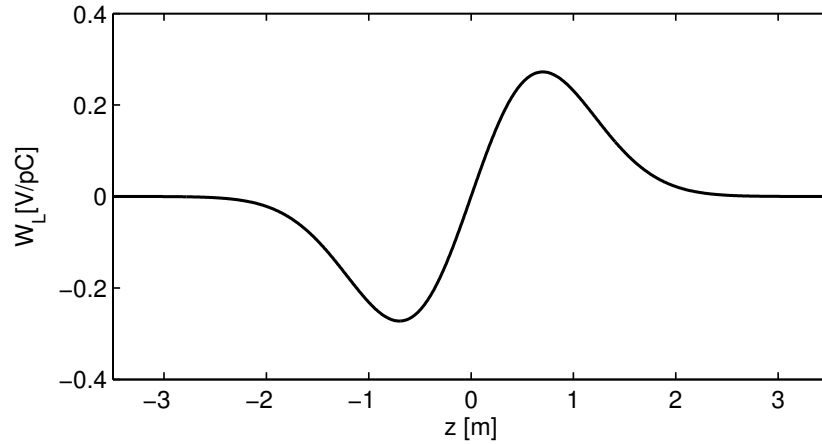


FIGURE 4.17: Longitudinal wake potential of a 2.3 ns Gaussian bunch given by the total simulated impedance budget.

TABLE 4.2: Contributions of the machine elements included in the longitudinal coupling impedance budget.

Machine element	$Z(p)/p$ [ $\Omega$ ]
Space charge	-1.9
Kicker magnets	13.8
Vacuum pumps	2.8
Resistive wall	0.09
Steps	0.96
Bellows	0.85



## Chapter 5

# Impedance studies of machine elements installed during LS1

### 5.1 Dummy septum

#### 5.1.1 Introduction and context

The challenge of the LHC injectors upgrade program is to produce higher intensity and brightness proton beams for collision in the LHC. In this framework, the PS Multi-turn extraction [9] was proposed with the aim of mitigating losses due to the shaving process that is at the heart of the Continuous Transfer (CT) technique, that has been used for years to transfer beams from the PS to the SPS. During the commissioning phase of the PS Multi-Turn Extraction (MTE) and the following operational period, a number of limitations have been observed; one of particular relevance, the high level of activation of the magnetic extraction septum in straight section 16 (see Chapter 2). The activation of the magnetic septum is the result of particles lost during the rise time of the extraction kickers. These losses are unavoidable due to the longitudinal structure of the beam required by the SPS. These issues have been addressed in many ways, and the adopted solution consists in installing a *dummy septum* in the straight section 15 of the PS ring [45]. By “dummy septum”, we mean a protection passive device, provided by a thin copper blade intercepting the beam during the rise time of the kickers. The blade is not generating any deflection and does not interfere with the circulating beam during injection and acceleration, but during the five extraction turns, it absorbs the particles that would be otherwise intercepted by the magnetic septum blade. The activation of the extraction magnetic septum in section 16 will then be reduced. The protection septum must act in

the same passive way for any kind of beam produced by the PS, and for extraction techniques different from MTE. The new device will then be enclosed in a concrete shielding, in order to minimize the level of radiation in the area.

### 5.1.2 Dummy septum design

The dummy septum model used in CST simulations is shown in Fig 5.1 (left). The position of the absorbing particles blade can be adjusted by means of a remote displacement system, allowing for an accuracy of 0.1 mm [46]. The blade can be placed between 80 and 100 mm from the PS orbiting beam during operation. Moreover, when the septum is not used, the blade can be moved to the parking position. The blade is mounted on a solid copper support table that is also designed for transferring heating released by the beam in the blade via a copper conductor connected to a water cooling. A stainless steel RF beam screen has been integrated and connected to the upstream and downstream ends of the tank using multi-contacts. Finally, a beam observation system has been designed, in order to measure the position of the extracted beam and to adjust precisely the extraction blade position.

To perform impedance simulations, several aspects of the beam operation of the dummy septum were considered. During operation, the beam circulates in a nominal position displaced by 27 mm from the geometrical center of the septum. During extraction, the beam moves from the circulating position to few millimeters from the copper blade in about 6 ms. The beam then circulates close to the blade for only few turns before extraction. The design of the septum used for simulations considers the blade positioned at 90 mm from the nominal circulating beam. The mechanical drawings is shown in Fig. 5.1 (right).

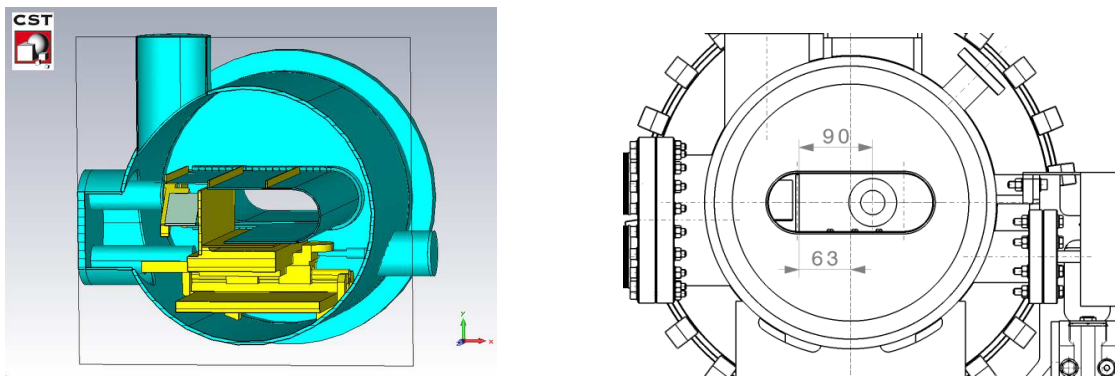


FIGURE 5.1: Dummy septum simplified model used for CST simulations (left) and dummy septum mechanical model with blade in nominal position with respect to the orbiting beam (right).



FIGURE 5.2: Dummy septum tank and motor allocation.

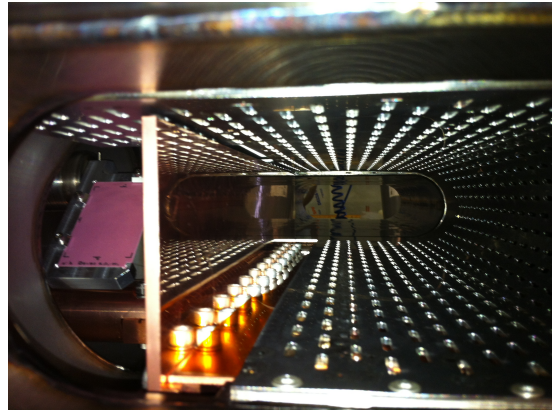


FIGURE 5.3: Inside view with BTV, blade and screen installed.



FIGURE 5.4: Inside view with blade and support table installed.

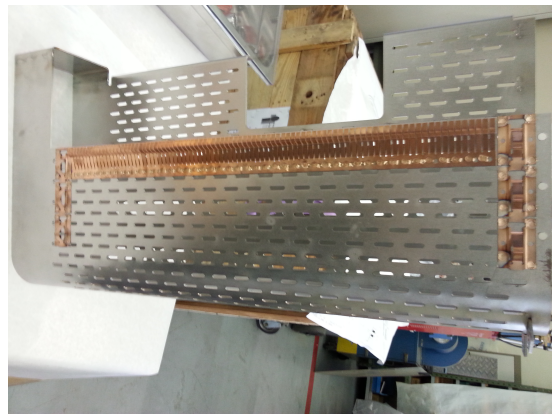


FIGURE 5.5: Beam Screen before with sliding fingers before installation.

### 5.1.3 Impedance aspects

Sharp resonances, namely *trapped modes*, are generated by the electromagnetic interaction of the field produced by the particle beam with the internal equipment of the dummy septum. Simulations and theoretical calculations have been performed in order to evaluate longitudinal and transverse coupling impedances due to trapped modes [47], and their impact on the stability of the beam. The final outcome of these studies represented the basis for acceptance of septum installation in section 15 of the PS ring. The importance of the study is justified by the fact that the septum should require essentially no maintenance and, in the event of damage, a spare will be available for replacement. In fact, the very high level of activation expected in the device, is going to exclude many long repairing interventions.

Since all discontinuities inside the dummy septum can be potential sources of trapped modes, the model used in simulation must be as close as possible to the real object. The analysis has been performed on simplified 3D geometries imported from mechanical CATIA drawings [48], assuming that geometry simplifications have a negligible impact on

final results. In particular the beam observation screen, the holes in the RF beam screen and the screws inside the tanks are elements that have been neglected during simulations. CST Particle Studio Wakefield Solver has been used to perform time domain simulations, of the wake potential generated by a Gaussian bunch circulating inside the septum. The beam coupling impedance components are then evaluated by Particle Studio from the Fourier transform of the wake potential. To crosscheck results obtained with Particle Studio (time domain), CST Microwave Studio (frequency domain) simulations have been performed. The evaluation of the frequencies of eigenmodes resonating in the structure is done by the Eigenmode solver, while  $Q$  factor, shunt impedance  $R_s$ , and  $R/Q$  are obtained from the post-processing. The correct evaluation of the resonance parameters is fundamental to obtain good accuracy in the estimation of the impact of the mode on coupled bunch instability.

In section 5.1.4 we show that beams circulating in the septum generate trapped modes, producing narrow resonances in the coupling impedance; trapped modes' frequencies also correspond to the eigenfrequencies of the closed structure. Since low-frequency trapped modes are a potential source of coupled bunch instability for the PS, two different solutions for reducing their impact on the stability of the beam have been considered, and they are discussed in section 5.1.7.

#### 5.1.4 Impedance simulations

To perform longitudinal impedance simulations in CST Particle Studio, both the beam and the integration path need to be placed on the same axis position. Then, the longitudinal impedance can be evaluated at different distances from the location of the blade. From simulations, excitation of trapped modes in the longitudinal and transverse impedance, due to the passage of a beam of r.m.s. bunch length of 26 cm, has been observed. This bunch length corresponds to the shorter bunch for the PS at flat bottom, and has been chosen to obtain a good resolution in the desired frequency range. Trapped modes frequencies, which also correspond to the eigenvalue of the closed structure, do not depend on the beam position. On the contrary, the amplitudes of several peaks are increasing while the relative distance between the beam and the blade is decreasing. Before extraction, while the beam covers 90 mm in about 6 ns to approach the blade, a significant increase of shunt impedance for some trapped mode has been observed. During extraction, when the beam is close to the blade at a minimum distance of 5 mm, the maximum of the impedance peaks' amplitude is reached. This effect is due to the strong electromagnetic field trapped at the edges of the blade after the passage of the beam.

Since the inner geometry of the dummy septum is strongly asymmetric, all trapped modes excited by the passage of the beam, have both longitudinal and transverse components.

TABLE 5.1: Main parameters of CST Particle Studio simulations for the longitudinal coupling impedance simulation.

Bunch length	26 cm
Wake length	100 m
Frequency max	700 MHz
Number of mesh cells	812.360 hexahedral
Method of field integration	Direct

The dipolar impedance can be evaluated with CST Particle Studio by shifting the beam in the transverse direction and by performing the integration of the field along the central axis. Similarly, the quadrupolar impedance can be obtained by shifting the integration path while keeping the beam in the center. The dipolar (resp. quadrupolar) component is then calculating subtracting from the simulated dipolar (resp. quadrupolar) transverse impedance the same term evaluated in the center and then dividing by the displacement [49]. For the transverse impedance, the same increase in the amplitude of the peaks while the beam is approaching the blade has been observed. For this reason, only numerical examples of the longitudinal component of the impedance are shown, since the transverse one shows a similar behavior. Figure 5.6 shows the real part of the longitudinal

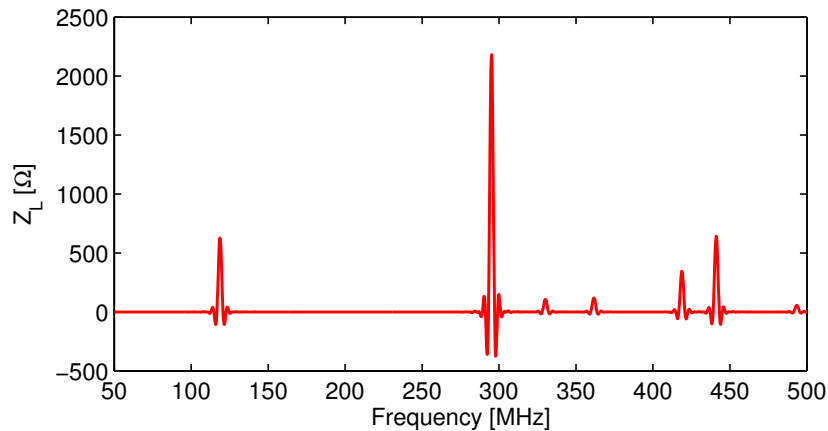


FIGURE 5.6: Longitudinal beam coupling impedance at extraction evaluated with CST Particle Studio 2012.

impedance excited by a bunch of r.m.s. length 26 cm and charge 1 nC, circulating 5 mm away from the axis of the copper blade. The wake potential has been evaluated through the Direct Integration Method using a wake length of 100 m. Perfect electric conductor (PEC) has been defined on all the outer surfaces, except for the beam entrance and exit planes that have been defined as open boundaries (perfect matching layer) due to the beam pipe aperture. No symmetry planes have been used. The parameters used in simulation are summarized in Table 5.1. Resonant parameters of the dummy septum can be rapidly calculated post-processing the Eigenmode simulation. As shown in Table 5.2, the first trapped mode excited by the beam resonates at 118 MHz with a  $Q$  factor of 2616

TABLE 5.2: Resonant parameters of the first ten eigenmodes.

Frequency [MHz]	Q	$R_s[\Omega]$ orbit	$R_s[\Omega]$ extraction
118	2655	62	36176
295	3975	76	74899
331	3947	7	5153
362	4727	2	2909
420	4987	13	10109
441	4885	22	18914
495	5777	3	2097
533	7597	9	8852
616	3585	3	2145
656	5805	18	13988

and, since  $Q$  depends only from the geometry, it will be constant for the same mode while the beam is moving from the nominal position towards the blade during extraction. The shunt impedance of the 118 MHz mode has been evaluated in the case of a beam placed in nominal position and in the case of a beam at 5 mm from the blade at extraction: in the latter case it has been estimated to be approximately 36 k $\Omega$ . Between the nominal and the extraction positions, the shunt impedance increases of a factor 600. The amplitude of the impedance's peaks does not correspond to the shunt impedance of each resonance, since the saturation of the peaks is reached when the simulation is performed with a wake length of about 7 km, calculated as  $WL_{max} = \frac{\Delta f}{c_{light}}$ . Such a time consuming simulation has been performed and fits with the shunt impedance evaluated by the Eigenmode solver. Only numerical examples of the longitudinal impedance obtained with a wake length of 100 m are shown, as qualitative output of CST Particle Studio.

For the PS, we assume that only resonant modes with a frequency lower than 200 MHz represent potential issues for coupled bunch instability: the growth rate of an instability increases significantly while the frequency of the mode is diminishing. For this reason, the mode at 118 MHz has been studied in more detail in section (5.1.5), while the other trapped modes at higher frequencies are not expected to be source of coupled bunch instability.

### 5.1.5 Coupled bunch instability evaluation

Longitudinal coupled bunch (CB) oscillations represent a major source of instability, limiting the beam intensity and brightness that can be delivered from the CERN PS. Low frequency trapped modes with high Q factor and shunt impedance are potential source of this instability for the PS [50] [51]. To deeply investigate the possible impact of the 118 MHz mode, the coupled bunch instability growth rate has been calculated with the

TABLE 5.3: PS-LIU parameters (25 ns bunch spacing) considered for coupled bunch calculations.

Energy [GeV]	13	26
RF voltage [kV]	165	100
Harmonic number	21	84
Number of bunches	18	72
Charge per bunch [C]	$1.28 \cdot 10^{-7}$	$3.2 \cdot 10^{-8}$
Slippage factor	0.0163	0.0215
rms bunch length [ns]	3	3

following formula, which is valid for a mode fully coupled with the multi-bunch spectrum [52]:

$$\alpha = \frac{c^2 \eta_c q N_b}{2L^2 E_0 \omega_s} \omega_r \operatorname{Re}(Z(\omega_r)), \quad (5.1)$$

where  $\eta_c$  is the slippage factor,  $q$  is the bunch charge,  $N_b$  is the number of bunches,  $L$  the length of the machine,  $E_0$  the beam energy,  $\omega_s$  the synchrotron frequency, and  $\omega_r$  the resonance frequency. Resonant parameters are taken into account for the calculation of the broad-band impedance

$$Z(\omega_r) = \frac{R_s}{1 + iQ\left(\frac{\omega}{\omega_r} - \frac{\omega_r}{\omega}\right)}. \quad (5.2)$$

Since the septum is going to work in all operational conditions and with several types of beam, growth rates should be evaluated at different beam energies, assuming worst case scenarios. The beam parameters that have been considered for the estimation are summarized in Table 5.3. Furthermore, to be closer to the real conditions, the actual Gaussian shape of the bunch has to be taken into account. Therefore, the shunt impedance  $R_s$ , evaluated with CST Microwave Studio, has to be corrected with the following form factor:

$$R_s' = R_s e^{-(\omega_r \sigma_b)}. \quad (5.3)$$

When such a correction is taken into account, the amplitude of the shunt impedance is drastically reduced. In Table 5.4, the values of growth rate for the 118 MHz mode, evaluated both at intermediate (13 GeV) and extraction (26 GeV) energies, for different beam positions from the geometrical center of the septum, are summarized.

TABLE 5.4: Coupled bunch instability growth rates evaluated for different beam position inside the septum.

Displacement [mm]	$R_s$ [Ω]	$R_s'$ [Ω]	$\alpha$ [s <sup>-1</sup> ] 13 GeV	$\alpha$ [s <sup>-1</sup> ] 26 GeV
0	640	10	0.15	0.08
20	3385	53	0.82	0.43
40	14762	231	3.59	1.87
60	49215	770	11.97	6.25

### 5.1.6 Contribution to the total Proton Synchrotron Impedance budget

The imaginary part of the longitudinal impedance beam coupling of the PS has been evaluated with measurement campaigns [17] [42] to be

$$\frac{Z(p)}{p} = 18.4 \pm 2.2 \Omega, \quad (5.4)$$

as discussed in Chapter 4. In order to calculate the contribution of the dummy septum to the total PS impedance budget, simulations with very long bunch length were performed. This choice allows to identify the low frequency inductive impedance. A long bunch, circulating in nominal position in the septum, excites an imaginary part of the longitudinal impedance that is purely inductive, giving an effective impedance of  $\frac{Z(p)}{p} = 0.001 \Omega$ . In comparison with the measured value, the contribution of the dummy septum to the PS longitudinal impedance budget is expected to be negligible. When the bunch circulates at 5 mm from the blade before extraction, the effective impedance is  $\frac{Z(p)}{p} = 0.12 \Omega$ , much larger than in the previous case. Nevertheless, at extraction, the contribution of the dummy septum to the PS longitudinal impedance budget is less than 1%. For the sake of comparison, the 200 MHz cavities complex of the PS provides a contribution of about 4% of the total longitudinal impedance. Hence, no issue is expected under any of the operational conditions foreseen.

### 5.1.7 Mode damping proposals

In the unlikely event of unexpected failure or damage of the dummy septum after installation and shielding, repairing action and intervention will be complicated and potentially dangerous. This fact justifies the interest in finding preventive measures, for example reducing the impact of a mode that, from simulation results, is not predicted to be an issue for the stability of the beam. For this reason, two proposals of modifications of the inner design have been studied with the aim of damping the 118 MHz mode. Since the resonance at 118 MHz is mainly localized in the gap between the RF beam screen and the support table, the first solution consists of inserting sliding contacts among them: closing the gap has the effect of canceling the mode at 118 MHz, as shown in fig. 5.7. Similarly, a small amount of energy is also trapped at the edge of the blade, in the 3 mm gap between the impedance screen and the blade itself. To avoid that resonance, it would be necessary to create contacts between the two object, filling the gap. Unfortunately, this last solution, cannot be easily implemented. The second solution consists in inserting a block of ferrite TT2-111R, a material with good electromagnetic performances in the frequency range of interest. This solution would not have the effect of damping the

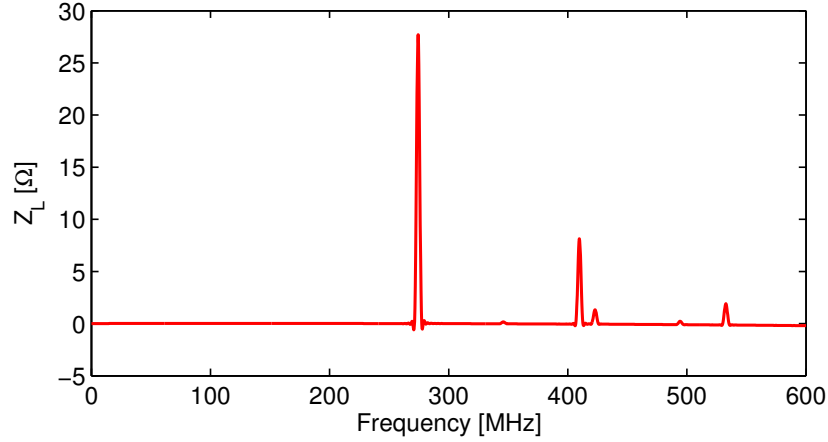


FIGURE 5.7: Longitudinal coupling impedance at extraction evaluated with CST Particle Studio after the insertion of sliding contacts between the screen and the support table.

mode, but would reduce the shunt impedance  $R_s$  and  $Q$  of the mode itself and, as a consequence, the impact of coupled bunch instability. Several studies have been performed using CST Particle Studio, using different dimensions and positions of the ferrite. As a general rule, the brick of ferrite should be placed inside the tank where the magnetic field is stronger; therefore, we suggested to position a brick of  $24 \times 7 \times 395$  mm<sup>3</sup> between the displacement system and the impedance screen, as shown in Fig. 5.9. With this solution, the shunt impedance reduction of the 118 MHz mode at extraction has been estimated to be about a factor 600. For power loss estimation we consider the following formula for sharp resonances [53]:

$$P_l = 2(MI_b)^2 R_s 10^{\frac{P_{dB}(f_r)}{10}} \quad (5.5)$$

where  $MI_b$  is the total beam current,  $R_s$  is the shunt impedance and  $P_{dB}(f_r)$  is the power in dB read from the beam power spectrum at the frequency  $f_r$  (see Chapter 2 for beam spectra measurements). Since the 118 MHz mode falls inside the PS bunch extraction spectrum with power of -20 dB, the deposited heating would be about 3.6 W and the foreseen cooling system should easily cope with it.

As an outcome of these studies, the decision has been taken to install the sliding contacts between the RF beam screen and the support table. A picture of the sliding fingers mounted on the screen before installation is shown in Fig. 5.5. The option of installing a block of ferrite is left as a fall back solution to be implemented only in case of failure of the sliding contacts. Therefore, the blade displacement system has been equipped with a support that could be used to house the ferrite block.

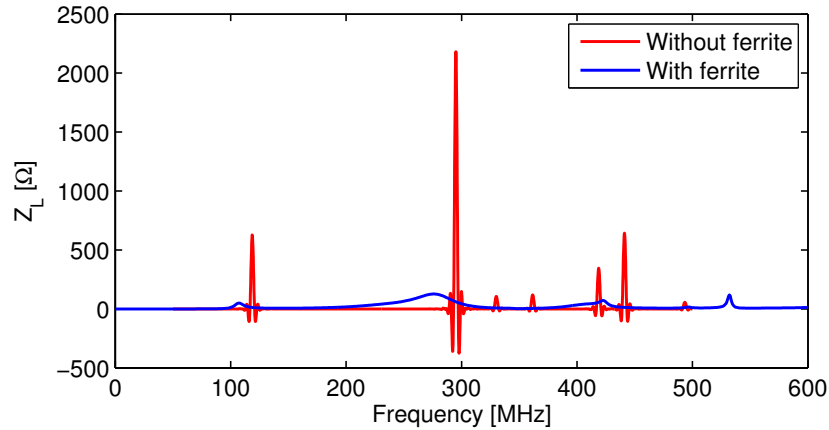


FIGURE 5.8: Comparison between longitudinal impedance evaluated with CST Particle Studio with and without ferrite.

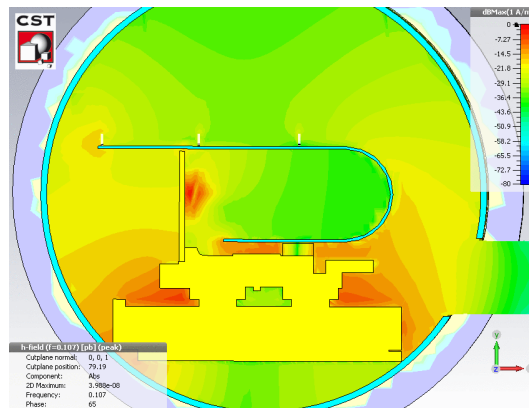


FIGURE 5.9: Magnetic field lines on a transversal cut in the dummy septum with the ferrite block insertion.

### 5.1.8 RF impedance measurements

Coupling impedance RF measurements have been performed to confirm the results of numerical simulations, to test the effectiveness of the sliding contacts, and to assess the need of ferrite. Two measurement campaigns were performed at the end of 2013 and at the beginning of 2014, respectively. After the first set of measurements, due to an oil leakage, the septum was opened, cleaned and assembled again. Because of a mechanical break down, also the sliding fingers were replaced before the second set of measurements was carried out. The well-known technique based on the coaxial wire method [54] has been used, allowing to excite in the device under test an electromagnetic field similar to the one generated by an ultra-relativistic point charge. The impedance has been measured stretching a metallic wire of 0.5 mm radius inside the septum, modeling a TEM-like coaxial line; the wire was then connected to two matching resistors to consider the effect of the mismatch at the beginning and at the end of the perturbed transmission line. Two carbon resistances of 276  $\Omega$  and 281  $\Omega$  were welded to a suco-box of 16 mm length on

one side, and to the stretched wire on the other side, as shown in Fig. 5.10. This setup allows measuring the transmission coefficient  $S_{12}$  by means of a Vector Network Analyser (VNA). Using special flanges and 10 dB attenuators, the impedance for three positions of the wire/beam with respect to the extraction blade has been measured, while the position of the blade was fixed at 90 mm from the nominal orbit beam position, and the beam monitor (BTV) was placed in out position, for both set of measurements. Figure 5.11

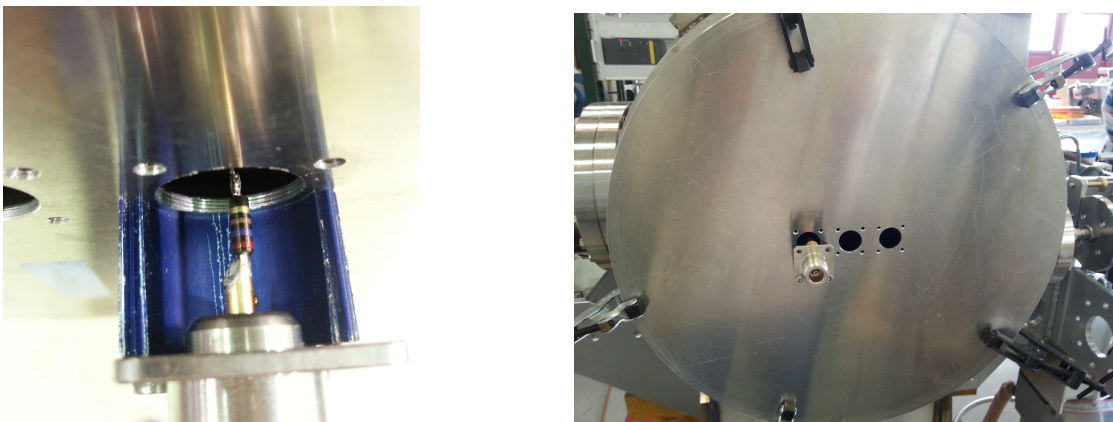


FIGURE 5.10: Measurement setup for dummy septum impedance measurements. On the left, a suco box connected to the septum flange and welded to the stretched wire through a matching resistor; on the right, the flange with three holes to allow different position for the wire.

shows the comparison of the impedance measurement for the three wire positions during the second set of measurements. The first trapped mode is excited with a frequency of 270 MHz, thus indicating that the sliding fingers are working as expected on cancelling the mode at 118 MHz. Moreover, 270 MHz is predicted to be too high frequency to be source of coupled bunch instability in the PS, even with a  $Q$  factor of 3413, shunt impedance calculated at extraction of 21.6 k $\Omega$  and power loss at extraction of 9 W. Also in this case the foreseen cooling system should easily cope with power loss. From Eigenmode simulations is it clear that this mode is generated by resonances trapped at the gap between the impedance screen and the copper blade, and increases in amplitude when the wire/beam is set closer to the blade, as shown in Fig. 5.11. Measurements have also been compared with realistic simulations performed with CST Microwave Studio Frequency domain solver. The measurement setup is simulated adding the metallic wire in the geometry and calculating the scattering parameters at the input and output port of the device under test. As shown in Fig. 5.12, measurements and simulations agree on the frequency of the first trapped mode resonating in the septum. The second peak not visible in the simulation, is due to the presence and to the position of the BTV in the assembly. Nonetheless, measurement results confirm that the dummy septum can be safely installed in the PS ring and that the insertion of ferrite is not needed.

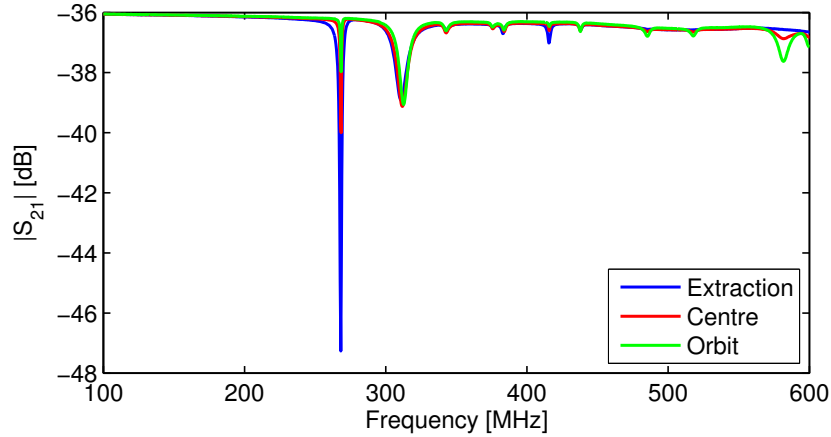


FIGURE 5.11: The  $S_{21}$  transmission coefficient measured for three positions of the wire respect to the extraction blade.

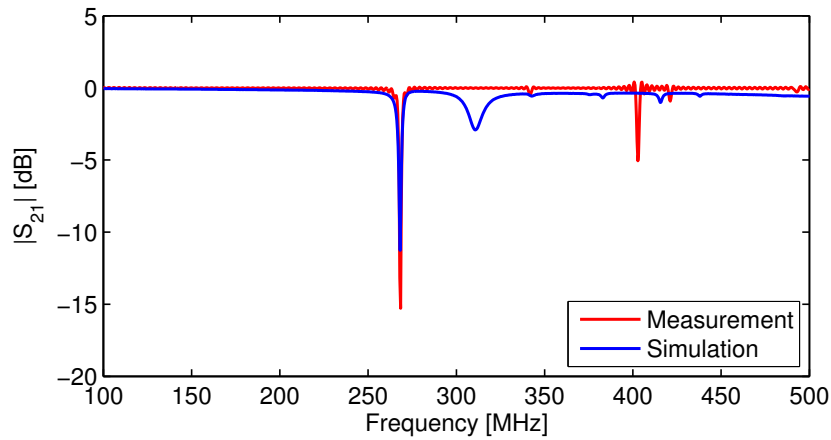


FIGURE 5.12: The  $S_{21}$  transmission coefficient measured at extraction compared with CST Microwave Studio simulation in frequency domain.

## 5.2 Finemet loaded longitudinal damper

### 5.2.1 Introduction

In the framework of the LHC Injectors Upgrade (LIU) a new longitudinal damper cavity has been designed [55] [56] to operate as coupled bunch feedback for the CERN Proton Synchrotron (PS), providing a correction of the RF voltage to the circulating bunches and avoiding the generation of coupled bunch oscillation. Before the installation of the new damper, the coupled-bunch feedback was provided by a dedicated 10 MHz cavity (see Chapter 2), operating as longitudinal kicker. The design of the new damper, driven by a solid state amplifier, is based on the wideband frequency characteristics of Finemet® [57] magnetic alloy. Beam coupling impedance studies for the new elements were performed before installation in the PS, in order to determine the contribution of the new device to the current coupling impedance budget of the machine, to exclude the excitation of

trapped modes due to the interaction between the beam and the cavity, to assess the impact on the stability of the beam, and to explore the electromagnetic characteristics of Finemet®.

### 5.2.2 Longitudinal impedance calculation

The Finemet® loaded longitudinal damper has been initially modeled in CST Particle Studio as a single cell cavity [58] [59]. This model consists of a beamline section with an alumina gap of 3 mm and two Finemet® rings of 165 mm radius and 25 mm thickness, enclosed into a metallic squared tank. Finemet® has been put in contact with the tank of the damper through two support copper disks. Such a cavity system forms two  $\lambda/4$  resonators excited in counter-phase. The single cell model used for impedance simulations is shown in Fig. 5.13. Finemet® dispersive parameters have been defined in CST importing  $\mu_1$  and  $\mu_2$  measured data. CST offers the possibility of defining and automatically fitting a specific magnetic material dispersion curve from uploaded data: several different magnetic dispersion fit models can be chosen, but in this case a general N-th order has been selected. The relative permittivity of Finemet® has then been set up as  $\epsilon_r = 25$ . A comparison between the Finemet® measured and fitted  $\mu_1$  and  $\mu_2$  parameters is shown in Fig. 5.14.

For CST Particle Studio 2012 simulations, the bunch length was chosen in order to obtain a good resolution in the desired frequency range, according to the relationship  $f = \frac{c}{1.69\sigma_b}$ , while the length of the wake has been fixed long enough to obtain impedance peaks with saturated amplitude. A bunch length of 50 cm and bunch charge of 1 nC has been considered. The wake potential has been evaluated through the Indirect Test Beam integration method using a wake length of 600 m. The indirect method computes the longitudinal wakes generated by the interaction of test beams with the wall of the beam tube to get the longitudinal wake everywhere in the cross section of the cavity and it is considered the most accurate calculation method. Perfect electric conductor (PEC) has been defined on all the surface as boundary condition, excepted for the Z plan (beam entrance and exit plane) that has been defined open due to the beam pipe aperture. XZ and YZ symmetries have been used to reduce by a factor four the computational time. The main parameters of the simulation are summarized in Table 5.5.

In the low frequency longitudinal impedance one can identify the first accelerating mode of the cavity; the real part of the longitudinal impedance is about 350  $\Omega$  at a frequency of 4 MHz. Results from simulations have been compared to the longitudinal impedance obtained with bench measurements of the single cell prototype. Measurements and simulations show good agreement for frequencies higher than 4 MHz, while for lower frequencies small discrepancies are due to the low accuracy in the fitting of the dispersive parameters

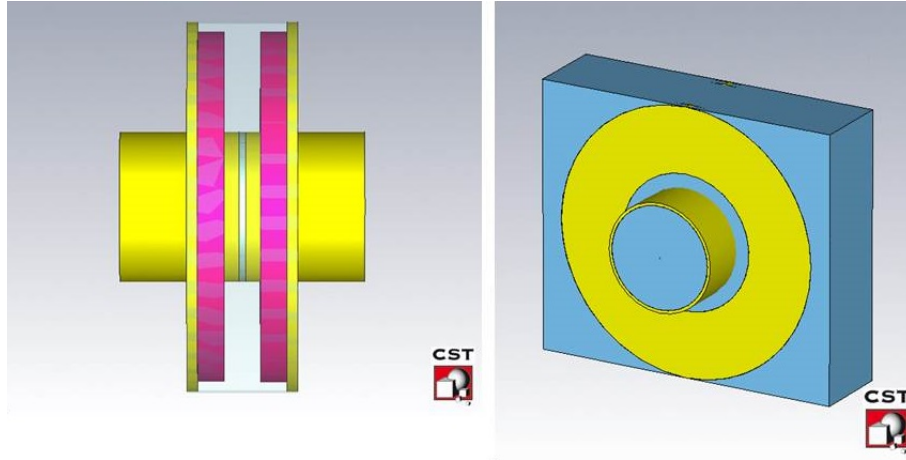


FIGURE 5.13: CST model of the one cell prototype of the Finemet® loaded longitudinal damper.

TABLE 5.5: Main parameters of CST Particle Studio simulations for the single cell damper.

Bunch length	50cm
Wake length	600m
Frequency max	200MHz
Number of mesh cells	112.860 hexahedral
Method of field integration	Indirect Test Beam

performed by CST Particle Studio. A comparison between measured and simulated longitudinal coupling impedance is shown in Fig. 5.15.

Furthermore, the strong damping effect of Finemet can be observed from simulations: no excitation of parasitic or trapped modes has been detected. The final model of the

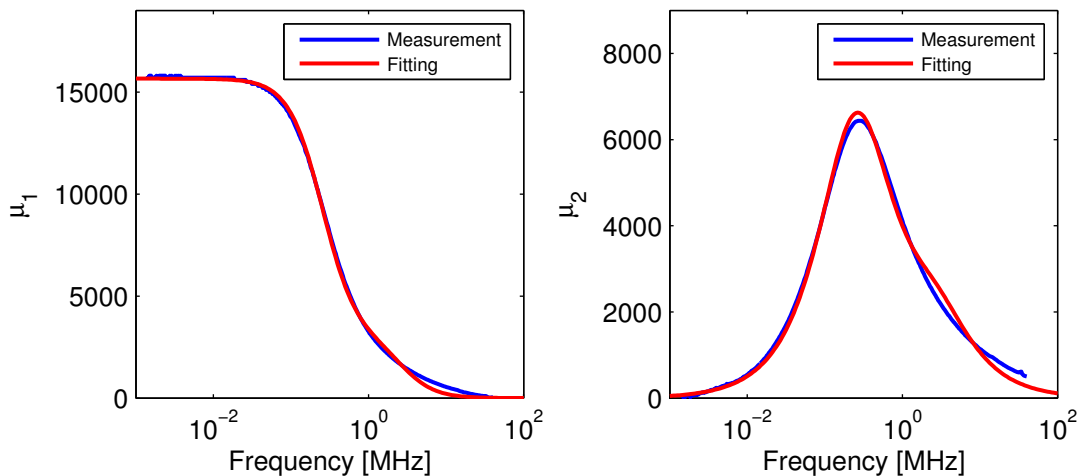


FIGURE 5.14: Comparison between Finemet® measured and fitted dispersive parameters  $\mu_1$  and  $\mu_2$ .

longitudinal damper, made of six Finemet® loaded cells, is shown in Fig. 5.16. The model has been obtained repeating six times the single cell model, allowing to obtain

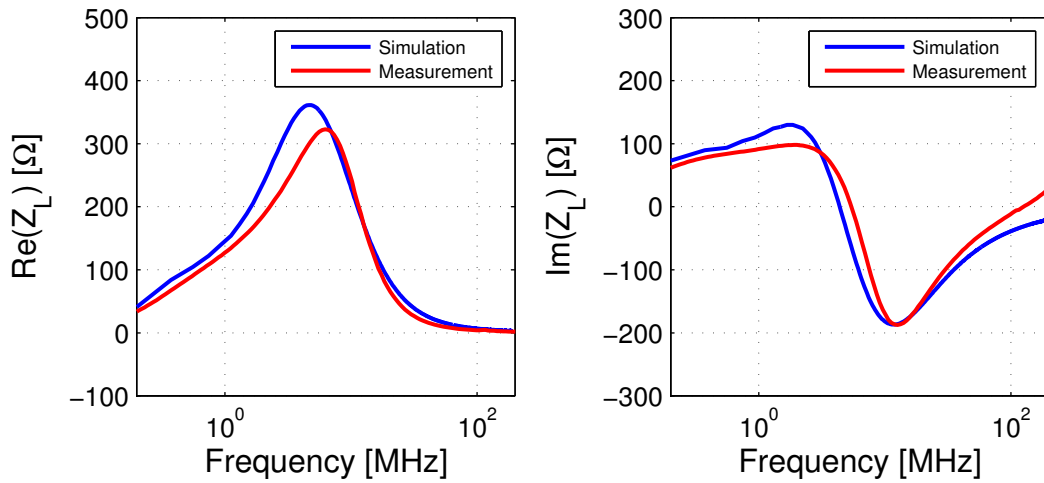


FIGURE 5.15: Longitudinal impedance of the single cell damper.

TABLE 5.6: Main parameters of CST Particle Studio simulations for the six cells Finemet® loaded longitudinal damper.

Bunch length	50cm
Wake length	600m
Frequency max	345MHz
Number of mesh cells	3,000,816 hexahedral
Method of field integration	Indirect Test Beam

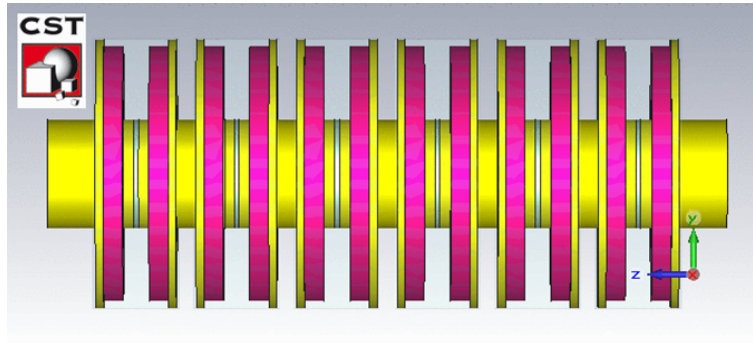


FIGURE 5.16: CST model of the six cells Finemet® loaded longitudinal damper.

a good model for simulation and avoiding all the issues connected to import a complex drawing from a mechanical CAD. The model does not include transitions between the circular pipe of the cavity and the elliptical pipe of the PS: no changes on the impedance have been predicted because of the tapers, thanks to the large bunch length circulating in the PS (26 cm-12 m), as will be discussed in Chapter 6. The main parameters of the six cells simulation are resumed in Table 5.6, while the longitudinal coupling impedance is shown in Fig. 5.17. The first accelerating mode of the cavity is clearly visible from the longitudinal impedance. PS bunches circulating in the center of the cavity can excite a longitudinal impedance, the real part of which has a maximum of 2 kΩ at 4 MHz. Parasitic or trapped modes have not been detected.

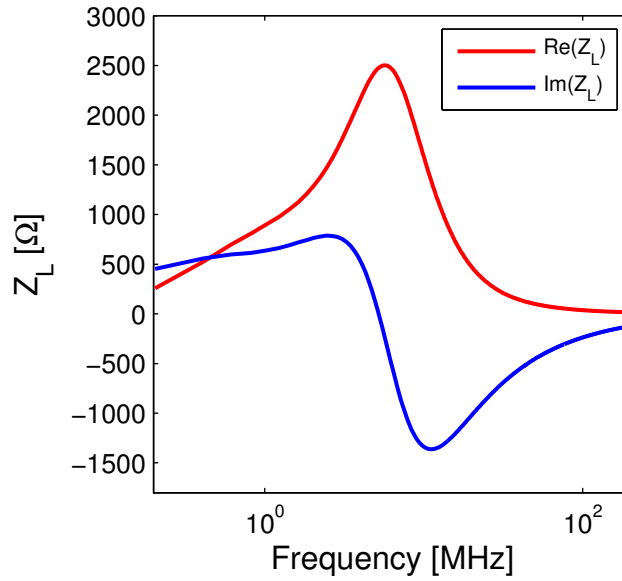


FIGURE 5.17: Longitudinal impedance of the six cells damper.

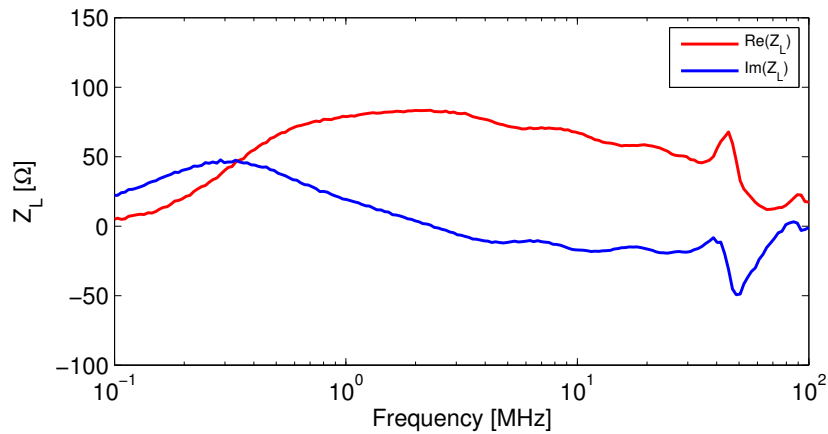


FIGURE 5.18: Measured longitudinal impedance of the single cell as seen by the beam when going through one gap connected to the amplifiers with 4 ns cables.

### 5.2.2.1 Connection Lines Effect on the Impedance

The longitudinal impedance seen by a beam circulating inside the damper is defined not only by the cavity impedance, but also by the effects of the amplifier output impedance and the connected transmission lines. The longitudinal impedance of the single cell prototype connected to the amplifiers through 4 ns cables has been measured, and is shown in Fig. 5.18. This response shows a broadening and a further reduction in the longitudinal impedance with respect to Fig. 5.15. By comparing the results with and without the effects of the power amplifier and the transmission lines, the contribution of the damper to the total impedance budget allows to conclude that the damper can be safely installed in the PS ring. An additional reduction of the cell impedance will be provided by means of a one-turn feedback loop.

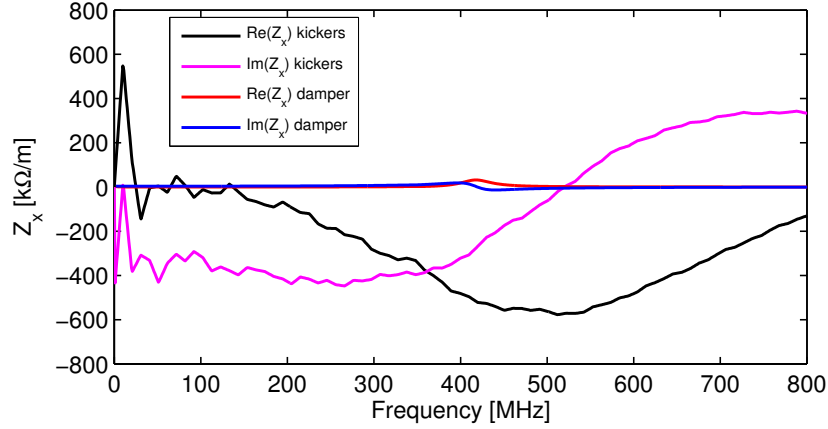


FIGURE 5.19: Comparison between the dipolar impedance of the longitudinal damper and the sum of the horizontal impedances of the PS kickers.

TABLE 5.7: Main parameters of CST Particle Studio transverse simulations for the six cells longitudinal damper.

Bunch length	200 cm
Wake length	800 m
Frequency max	511 MHz
Number of mesh cells	3,000,816 hexahedral
Method of field integration	Indirect Test Beam

### 5.2.3 Transverse impedance calculation

The transverse dipolar impedance can be evaluated with CST Particle Studio shifting the beam in the transverse direction and performing the integration of the field along the axis of the cavity. The dipolar component is then obtained by dividing the simulated transverse wake potential by this displacement. Being the structure symmetric is sufficient to compute the dipolar impedance shifting the beam in only one transverse direction. For this simulation XZ symmetry has been used, allowing a factor two reduction in the number of mesh cells. Simulations have been performed for both the single cell and the six cells models, considering different shifts of the beam from the center to verify linearity. The main parameters are summarized in Table 5.7. Simulation results confirm that the first accelerating mode of the cavity does not have a transverse component. Figure 5.19 shows that a broad parasitic mode at the frequency of 400 MHz is now excited as the dipolar impedance. The absence of excitation of this mode in the longitudinal impedance is probably due to the TE-like configuration of the field. In this plot, the transverse impedance of the longitudinal damper has been compared to the total horizontal impedance of the eleven kickers installed in the machine: the contribution to the transverse impedance budget of the machine is predicted to be negligible. The effective vertical coupling impedance of the six-cells device is 6 k $\Omega$ /m. Impedance simulations and measurements confirmed



FIGURE 5.20: Longitudinal damper after installation in SS01 of the PS ring.

that the longitudinal damper could be safely installed in the PS machine. In Fig. 5.20 a picture of the damper after installation in the ring is shown.

## 5.3 Tune Stripline Beam Position Monitor

### 5.3.1 Introduction

Beam position monitors are very common devices in particle accelerators for measuring the horizontal and vertical position of the circulating beams. For high energy circular accelerators like the PS, a large number of beam position monitors is usually required, introducing a significant contribution to the total coupling impedance of the machine. Therefore, an impedance study has been requested for the approval of the new stripline pickup to be installed during LS1 in straight section 72.

The new beam monitor is a cylindrical pickup provided by four striplines, connected through ports to the external tank of the device. The model used for beam coupling impedance simulations is shown in Fig. 5.21, while a picture of the pickup before installation is shown in 5.22 [60]. Each stripline has a length  $l = 0.779$  m and subtends an angle  $\phi_0$  to the transverse axis of the beam pipe. The system composed by the stripline and the beam pipe can be treated as a section of transmission line with a characteristic impedance  $Z_s = \sqrt{L/C}$ , where  $L$  and  $C$  are the inductance and capacitance per unit length. Signals can propagate in the transmission line with velocity  $\beta_s c = \frac{1}{\sqrt{LC}}$ . The four striplines are connected through ports to a transmission line of the same characteristic impedance, meaning that the signals induced on the stripline can propagate through one of the ports into a transmission line without reflections. This is equivalent to terminating each end of the stripline by a resistance of  $Z_s = 50 \Omega$ .

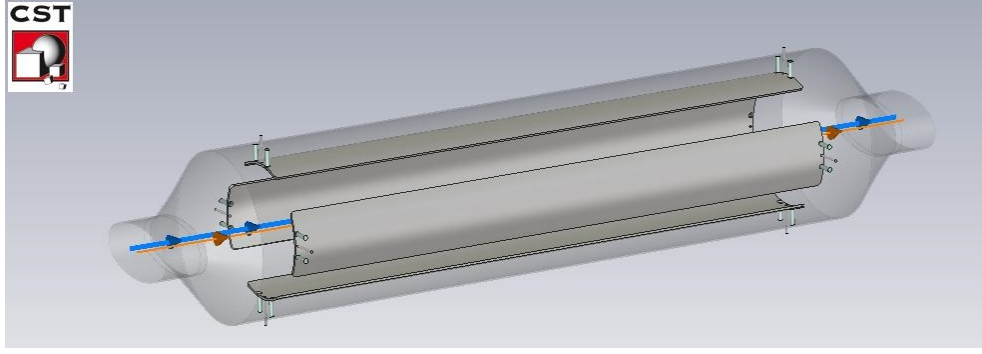


FIGURE 5.21: 3D model of the stripline beam position monitor used for implemented in CST Microwave Studio.

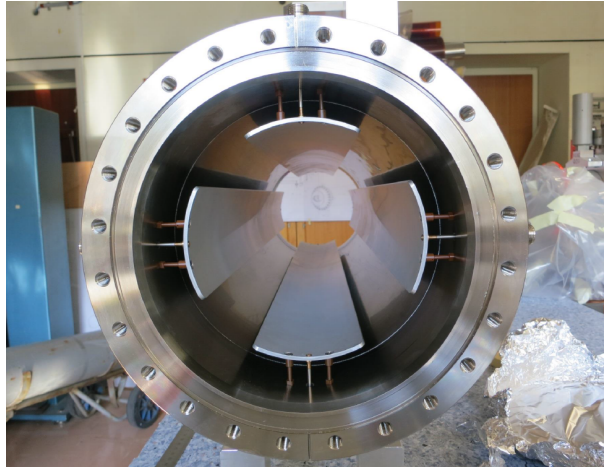


FIGURE 5.22: Pickup before installation.

### 5.3.2 Impedance calculation

The longitudinal beam coupling impedance of the device can be calculated with the following analytical formula [61] :

$$Z_L = 4Z_s \left( \frac{\phi_0}{2\pi} \right)^2 \left( \sin^2 \frac{\omega l}{c} + j \sin \frac{\omega l}{c} \cos \frac{\omega l}{c} \right). \quad (5.6)$$

It is clear that, if the stripline is matched at both terminations, we cannot observe the generation of parasitic modes. Nevertheless, at high frequencies, the stripline can support standing wave resonances having a node at the middle of the stripline, where the termination does not absorb any power. Moreover, resonances could occur whenever the length of the stripline is an half-integer multiple of the wavelength. Such resonances cannot therefore be damped by the matched transmission line. At low frequencies  $\frac{\omega}{2\pi} \ll \frac{c}{4l}$ , the longitudinal beam coupling effective impedance is given by [61]

$$\frac{Z_L}{n} \approx jZ_s \left( \frac{\phi_0}{\pi} \right)^2 \frac{l}{R}, \quad (5.7)$$

TABLE 5.8: Main parameters of CST Particle Studio simulations for the longitudinal impedance simulation of the beam position monitor.

Bunch length	18 cm
Wake length	300 m
Frequency max	560 MHz
Number of mesh cells	204.918 hexahedral
Method of field integration	Direct

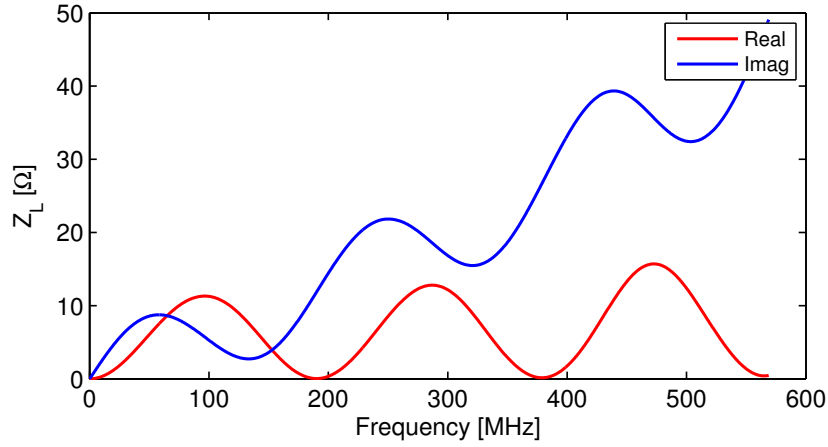


FIGURE 5.23: Longitudinal coupling impedance of the stripline beam position monitor calculated with CST Particle Studio.

while the transverse beam coupling effective impedance is given by

$$Z_T \approx j \left( \frac{8Z_s l}{\pi^2 R^2} \right) \sin^2 \frac{\phi_0}{2}, \quad (5.8)$$

where  $R$  is the beam pipe radius. Electromagnetic simulations of the new pickup have been performed using CST Particle Studio with the aim of excluding the excitation of low frequency resonances and to determine the impact of the new device on the total machine impedance. Table 5.8 summarizes the main parameter used in simulations. Thanks to the symmetry of the structure, only a quarter of the model has been considered, reducing the computational time of a factor four. In Fig. 5.23 the longitudinal impedance is shown. On the real part, the distance between two crests is about 180 MHz, corresponding to  $\lambda=1.6$  m, about twice the length of one stripline. The imaginary part cannot be treated as an inductive impedance, but the effective longitudinal coupling impedance can be evaluated for a certain frequency  $2\pi f = \frac{1}{\sigma_b}$ , with  $\sigma_b$  the bunch length. We have that, for  $\sigma_b=26$  cm (minimum bunch length in the PS) the effective impedance contribution is  $\frac{Z}{n} = 0.0052 \Omega$ , about the 0.2% of the total longitudinal impedance budget. Transverse coupling impedance is shown in Fig. 5.24. Also the effective transverse impedance is predicted to be negligible with respect to the transverse budget.

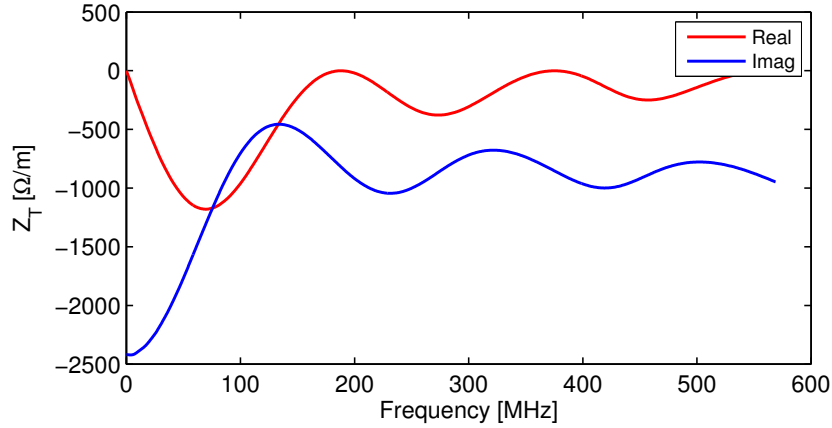


FIGURE 5.24: Transverse coupling impedance of the stripline beam position monitor calculated with CST Particle Studio.

## 5.4 Conclusions

Coupling impedance studies, including simulation, RF measurements and theoretical calculations, have been performed for three new devices, before their installation in the machine in the period 2013-2014. This studies helped to understand the contribution of the single elements on the longitudinal and transverse impedance models discussed in Chapters 4 and 5. In the case of the dummy septum, some modification of the design have been suggested in order to reduce the impact on the coupled bunch instability. The final contribution to the impedance of the three devices was predicted to be negligible, and the three devices have been correctly installed in the machine where are successfully working under normal operational condition.



## Part II

Electromagnetic field and beam  
coupling impedance of elliptical  
beam chambers and step  
transitions in particle accelerators



## Chapter 6

# Green functions in elliptical vacuum chambers

The second part of this thesis work is aimed to determine an analytical formula for the longitudinal beam coupling impedance of a step transition between two beam chambers with the mode matching method. The electromagnetic interaction of a charged particle beam with an abrupt step transition connecting two vacuum tanks produces an exchange of energy between the particle beam and the surrounding medium. This interaction can be described by means of the beam coupling impedance [1]. We assume that the cross sections of the step transition are confocal ellipses. In order to calculate the coupling impedance by means of analytical-numerical methods it is necessary to express the Green function and the eigenmodes of the elliptical chamber in elliptical coordinates, expanded as function of separate variables.

### Introduction

Let us consider a  $\delta$  distribution particle beam crossing an abrupt step transition between two beam chambers of elliptical cross-section. The electromagnetic field generated in the step transition is given by the superimposition of two terms: the first term is the source field of the particle beam traveling in the chamber, while the second term is represented by the source field that is radiated back from the discontinuity. This type of problem, involving two separate regions, can be addressed with the so-called *mode matching* method. Expressing the radiated field from the discontinuity as the product of a modal function for a modal coefficient, and imposing the condition on continuity of the tangential electric and magnetic fields at the interface, we obtain a set of linear equations for the unknown modal coefficients. Because of the functional form of the modal modes, the problem reduces in

determining a set of modal amplitudes associated with the field expansions in the two regions, where the primary field represents the known coefficients of the system. Solving this *matching system* allows to calculate the amplitude of the radiated electric field, and the longitudinal impedance is the Fourier transform of the field itself. In order to develop the matching system and calculate the coupling impedance, we need to calculate an expression in elliptical coordinates of the source field of the particle beam traveling in the chamber. For this purpose, in this chapter we are going to determine a novel formulation of the Green function in the free space expressed in elliptical coordinates. Moreover, the novel formulation is provided in separate functions of the elliptical coordinate variables. This formulation allows to calculate the *indirect* field, that is the response of the Green function to an elliptical boundary. Summing the contribution of the Green function (direct or primary field) and the scattered (indirect) field from the boundary, we can fully describe the electric field produced by the interaction of a  $\delta$  distribution particle beam traveling inside a tube of elliptical cross section. In order to match the particle distribution with the elliptical geometry, we need to introduce a set of functions, called *Mathieu functions*. Mathieu functions were introduced by their originator in 1868, when he determined the vibrational modes of an elliptical membrane with an elliptic boundary. Papers and books on the computation of Mathieu functions can be found in literature and include references [62], [63], [64] [65], [66], [67], while the fundamental reference works on Mathieu functions are in the books by McLachlan [68]. The computation of Mathieu functions is far from trivial and, in addition, built in library routines for Mathieu functions are not widespread. An available source of software for the computation of Mathieu functions is described in [65]. Nevertheless, it seems not to exist a single repository where official software and information about the computation of Mathieu functions can be found. The absence of explicit integral formula makes asymptotic analysis more difficult for Mathieu functions than for Bessel functions. In particular, we are going to show that the two-parameter dependence of the Mathieu functions and the non existence of an explicit formula for their evaluation, contribute to complicate calculation of eigenfunctions of the wave equation, arising by separating variables in elliptic coordinates.

## 6.1 Theory and applications of Mathieu functions

### 6.1.1 The wave equation in elliptical coordinates

Let us consider the wave equation for the longitudinal component of the electric field for a transverse magnetic (TM) field propagating in a generic waveguide

$$\Delta_t^2 E_z = (k_0^2 - k_z^2) E_z, \quad (6.1)$$

where  $k = \omega/c$  is the wave number in free space and  $k_z$  is the propagation constant. For an an elliptical cross section waveguide it is convenient to use confocal elliptical

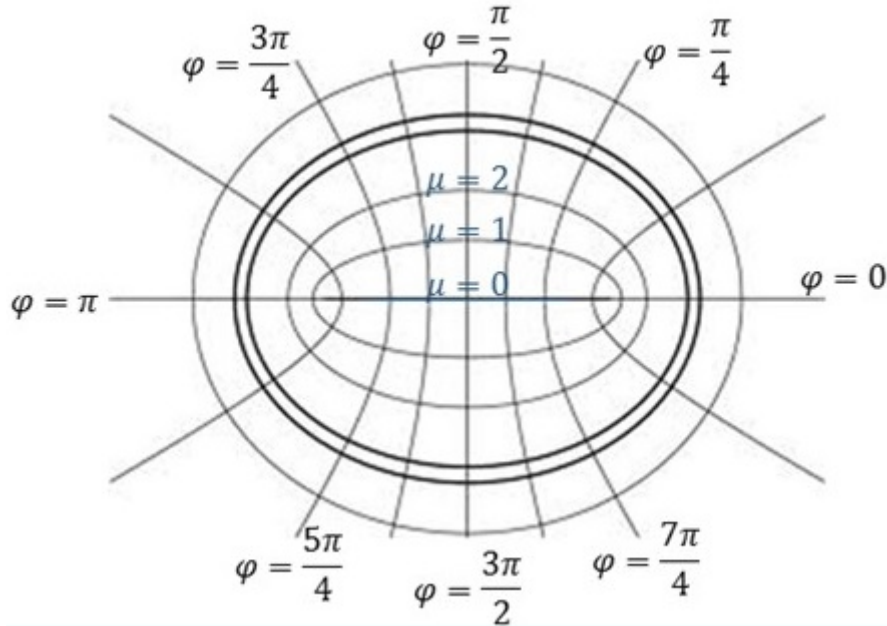


FIGURE 6.1: Elliptic Cylindrical Coordinates. The  $\varphi$  coordinates are the asymptotic angle of confocal hyperbolic cylinders symmetrical about the x-axis. The  $\mu$  coordinates are confocal elliptic cylinders centered on the origin.

coordinates. In an elliptical coordinate system we can define the *angular* coordinate  $\varphi$  as a set of hyperbolas having the same foci, and the *radial* coordinate  $\mu$  as a set of confocal ellipses. This nomenclature becomes obvious observing in Fig. 6.1 the similarity between the elliptic coordinates and the polar coordinates. The elliptic variable  $\varphi$  has a domain  $0 \leq \varphi \leq 2\pi$  and plays a similar role to a polar angle. The variable  $\mu$ , in the domain  $0 \leq \mu \leq \infty$ , behaves like a radial variable.  $F$  is the *focal distance* of the ellipse, and is related to the semi major and semi minor axes  $a$  and  $b$  by

$$F = \sqrt{a^2 - b^2}. \quad (6.2)$$

The line joining the foci corresponds to  $\mu = 0$ . The polar coordinates can be considered a special case of the elliptic coordinate in the limit  $F \rightarrow 0$ , when the foci of the elliptic coordinate collapses into the origin. In this limit, the angular and radial Mathieu equations become harmonic and Bessel equation, respectively. It is useful to parametrize an ellipse in terms of its *eccentricity*  $e$ , defined by

$$e = \frac{\sqrt{a^2 - b^2}}{a}. \quad (6.3)$$

The relation between elliptical and Cartesian coordinates is given by [62]

$$\begin{cases} x = F \cosh \mu \cos \varphi \\ y = F \sinh \mu \sin \varphi. \end{cases} \quad (6.4)$$

It is also useful to introduce a *scale coefficient*  $h(\mu, \varphi)$  for the elliptical coordinate, defined as

$$h(\mu, \varphi) = F \sqrt{\cosh^2 \mu - \cos^2 \varphi}. \quad (6.5)$$

The two-dimensional Laplacian in this coordinates system can be written as [69]:

$$\begin{aligned} \nabla_t^2 &= \frac{1}{F^2(\cosh^2 \mu - \cos^2 \varphi)} \left( \frac{\partial^2}{\partial \mu^2} + \frac{\partial^2}{\partial \varphi^2} \right) \\ &= \frac{2}{F^2(\cosh 2\mu - \cos 2\varphi)} \left( \frac{\partial^2}{\partial \mu^2} + \frac{\partial^2}{\partial \varphi^2} \right) = \frac{1}{h^2(\mu, \varphi)} \left( \frac{\partial^2}{\partial \mu^2} + \frac{\partial^2}{\partial \varphi^2} \right). \end{aligned} \quad (6.6)$$

If we substitute the above Laplacian definition in Eq. 6.1, we obtain the wave equation in elliptical coordinates [62]:

$$\frac{2}{F^2(\cosh 2\mu - \cos 2\varphi)} \left( \frac{\partial^2}{\partial \mu^2} + \frac{\partial^2}{\partial \varphi^2} \right) E_z - k_t^2 E_z = 0, \quad (6.7)$$

where  $k_t^2 = k_0^2 - k_z^2$  are the eigenvalues of the elliptical waveguide. A formal solution of Eq. 6.7 can be obtained with the method of variable separations. If we apply the method,  $E_z$  can be written in the form  $U(\varphi)V(\mu) e^{-ik_z z}$  and we can rewrite the equation above as:

$$\frac{1}{U} \frac{\partial^2}{\partial \mu^2} - \frac{k_t^2}{2} F^2 \cosh 2\mu = -\frac{1}{V} \frac{\partial^2}{\partial \varphi^2} - \frac{k_t^2}{2} F^2 \cos 2\varphi. \quad (6.8)$$

Separating variables of the wave equation gives two ordinary differential equations, involving a separation constant  $a$  and a frequency dependent parameter  $q$ . We will show that the two parameters dependence makes the computation of Mathieu functions more involved than, for example, Bessel functions. We can then rewrite Eq. 6.8 as two separate equations, considering that left and right-hand sides must be equal to the separation constant  $a$ :

$$\frac{d^2 U}{d\mu^2} + (a - 2q \cosh 2\mu)U = 0 \quad (6.9)$$

$$\frac{d^2 V}{d\varphi^2} - (a - 2q \cos 2\varphi)V = 0 \quad (6.10)$$

where

$$q = \frac{k_t^2 F^2}{4} \quad (6.11)$$

are the eigenvalues of the elliptical waveguides, depending by the geometry. Equations 6.9 and 6.10 are known as *Modified Mathieu Equation* and *Ordinary Mathieu Equation*,

respectively. Their solutions, that we are going to deduce in the next section, are known as *Modified Mathieu Functions* and *Ordinary Mathieu Functions*, respectively.

### 6.1.2 Solution of the Mathieu equations

The periodic solution of Eq. 6.10 can be obtained with a Fourier series expansion

$$V(q, \varphi) = \sum_{k=0}^{\infty} [A_k(q) \cos(k\varphi) + B_{k+1}(q) \sin(k+1)\varphi], \quad (6.12)$$

where  $k$  is the number of expansion terms and  $A_k$  and  $B_{k+1}$  are the Fourier coefficients. This solution can be separated into two parts as follows:

$$ce_r(q, \varphi) = \sum_{k=0}^{\infty} A_k(q) \cos(k\varphi) \quad (6.13)$$

$$se_{r+1} = \sum_{k=1}^{\infty} B_k(q) \sin[(k+1)\varphi], \quad (6.14)$$

where  $ce_r$  and  $se_{r+1}$  are known as the *even Mathieu function* of  $r$ -th order and the *odd Mathieu function* of the  $(r+1)$ -th order, respectively. The notation  $ce$  and  $se$  comes from “cosine-elliptic” and “sine-elliptic”.

If we substitute Eq. 6.12 in 6.10, we obtain recurrence relations for the Fourier coefficients  $A_k$  and  $B_{k+1}$  for a given characteristic value  $a_r$  and  $b_r$ :

$$\begin{aligned} & aA_0 - qA_2 = 0 \\ ce_{2n} \quad [k \geq 2] : & \quad (a-4)A_2 - q(2A_0 + A_4) = 0 \\ & (a-4k^2)A_{2k} - q(A_{2k-2} + A_{2k+2}) = 0 \end{aligned} \quad (6.15)$$

$$\begin{aligned} & (a-1)A_1 - q(A_1 + A_3) = 0 \\ ce_{2n+1} \quad [k \geq 1] : & \quad (a-(2k+1)^2)A_{2k+1} - q(A_{2k-1} + A_{2k+3}) = 0 \end{aligned} \quad (6.16)$$

$$\begin{aligned} & (b-4)B_2 - qB_4 = 0 \\ se_{2n+2} \quad [k \geq 2] : & \quad (b-(2k)^2)B_{2k} - q(B_{2k-2} + B_{2k+2}) = 0 \end{aligned} \quad (6.17)$$

$$\begin{aligned} & (b-1)B_1 - q(B_3 - B_1) = 0 \\ se_{2n+1} \quad [k \geq 1] : & \quad (b-(2k+1)^2)B_{2k+1} - q(B_{2k-1} + B_{2k+3}) = 0. \end{aligned} \quad (6.18)$$

In order to obtain a periodic solutions for the above recurrence relations, the characteristics values  $a$  and  $b$  must satisfy the following continued fractions [69]:

$$V_0 = \frac{2}{V_2 - \frac{1}{V_4 - \frac{1}{V_6 - \dots}}}; (Roots = a_{2n}) \quad (6.19)$$

$$V_1 - 1 = \frac{1}{V_3 -} \frac{1}{V_5 -} \frac{1}{V_7 -} \dots; (\text{Roots} = a_{2n+1}) \quad (6.20)$$

$$V_2 = \frac{1}{V_4 -} \frac{1}{V_6 -} \frac{1}{V_8 -} \dots; (\text{Roots} = b_{2n+2}) \quad (6.21)$$

$$V_1 + 1 = \frac{1}{V_3 -} \frac{1}{V_5 -} \frac{1}{V_7 -} \dots; (\text{Roots} = b_{2n+1}). \quad (6.22)$$

Once the characteristic values are calculated by solving continued fractions, the recurrence equations should be applied to obtain Fourier coefficients of Eq. 6.12.

For a given order  $n$ , there are four categories of periodic Mathieu functions that are solutions of 6.10. The (*angular*) ordinary Mathieu functions can be expressed as follows:

$$\begin{aligned} ce_{2n}(\varphi, q) &= \sum_{k=0}^{\infty} A_{2k}^{(2n)} \cos(2k\varphi) \\ ce_{2n+1}(\varphi, q) &= \sum_{k=0}^{\infty} A_{2k+1}^{(2n+1)} \cos(2k+1)\varphi \\ se_{2n+1}(\varphi, q) &= \sum_{k=0}^{\infty} B_{2k+1}^{(2n+1)} \sin(2k+1)\varphi \\ se_{2n+2}(\varphi, q) &= \sum_{k=0}^{\infty} B_{2k+2}^{(2n+2)} \sin(2k+2)\varphi \end{aligned} \quad (6.23)$$

As a consequence of orthogonality property of the sine and cosine series,  $ce_r$  and  $se_{r+1}$  are orthogonal functions [68]:

$$\int_0^{2\pi} ce_m(q, z) ce_p(q, z) dz = \int_0^{2\pi} se_m(q, z) se_p(q, z) dz = \begin{cases} 0 & m \neq p \\ \pi & m = p \end{cases} \quad (6.24)$$

By substituting 6.23 in Eq. 6.24, we obtain the following normalization condition for the Fourier coefficients:

$$2A_0^2 + \sum_{k=0}^{\infty} (A_{2k})^2 = \sum_{k=0}^{\infty} (A_{2k+1})^2 = \sum_{k=0}^{\infty} (B_{2k+2})^2 = \sum_{k=0}^{\infty} (B_{2k+1})^2 = 1. \quad (6.25)$$

Solutions of Eq. 6.9 can be obtained from 6.10 by setting the change of variable  $\varphi = j\mu$ , and are called (*radial*) *modified Mathieu functions*, defined as

$$\begin{aligned}
Ce_{2n}(\mu, q) &= \sum_{r=0}^{\infty} A_{2r}^{(2n)} \cosh(2r\mu) \\
Ce_{2n+1}(\mu, q) &= \sum_{r=0}^{\infty} A_{2r+1}^{(2n+1)} \cosh(2r+1)\mu \\
Se_{2n+1}(\mu, q) &= \sum_{r=0}^{\infty} B_{2r+1}^{(2n+1)} \sinh(2r+1)\mu \\
Se_{2n+2}(\mu, q) &= \sum_{r=0}^{\infty} B_{2r+2}^{(2n+2)} \sinh(2r+2)\mu,
\end{aligned} \tag{6.26}$$

where  $Ce_r$  and  $Se_{r+1}$  are known as the *even modified Mathieu function* of  $r$ -th order and the *odd modified Mathieu function* of the  $(r+1)$ -th order, respectively.

The spatial solution of the wave equation 6.7 is given by a combination of even and odd Mathieu functions:

$$W(\mu, \varphi) = \sum_{r=0}^{\infty} \left\{ \begin{array}{l} Ce_r(q, \mu) ce_r(q, \varphi) \\ Se_{r+1}(q, \mu) se_{r+1}(q, \varphi) \end{array} \right\}. \tag{6.27}$$

The solution of the wave equation, to satisfy the boundary conditions, has to be null on the contour of the ellipse

$$\left\{ \begin{array}{l} Ce_r(q, \mu_0) \\ Se_{r+1}(q, \mu_0) \end{array} \right\} = 0, \tag{6.28}$$

where  $\mu_0$  is the radial coordinate of the elliptical boundary, that can be calculated as

$$e = \frac{1}{\cosh \mu_0}, \tag{6.29}$$

where  $e$  is the *eccentricity* of the elliptical waveguide. Finally, the field components of the TM mode in an elliptical waveguide can be derived from the spacial TM solution, corresponding to the longitudinal electric field [70] [71]:

$$E_z = \alpha U(\mu)V(\varphi) \tag{6.30}$$

$$E_\mu = -\frac{ik_z\alpha U'(\mu)V(\varphi)}{k_t^2 F \sqrt{\cosh^2 \mu - \cos^2 \varphi}} \tag{6.31}$$

$$E_\varphi = -\frac{ik_z\alpha U(\mu)V'(\varphi)}{k_t^2 F \sqrt{\cosh^2 \mu - \cos^2 \varphi}} \tag{6.32}$$

$$H_\mu = -\frac{E_\varphi}{Z_{TM}} = \frac{i\omega\epsilon\alpha U(\mu)V'(\varphi)}{k_t^2 F \sqrt{\cosh^2 \mu - \cos^2 \varphi}} \tag{6.33}$$

$$H_\varphi = \frac{E_\mu}{Z_{TM}} = -\frac{i\omega\epsilon\alpha U'(\mu)V(\varphi)}{k_t^2 F \sqrt{\cosh^2 \mu - \cos^2 \varphi}} \quad (6.34)$$

$$H_z = 0, \quad (6.35)$$

where  $Z_{TM}$  is the characteristic impedance of the TM mode and  $\alpha$  is the field amplitude. Plots of the Mathieu angular and radial functions and their derivative are shown in Figures 6.2 and 6.3. The functions were derived with the Matlab toolbox described in [65] and normalized as in Eq. 6.25. In these examples, the geometry of the PS elliptical beam chamber has been considered. It can be easily seen that, in the limit  $F \rightarrow 0$ , the angular and radial Mathieu equations becomes harmonic and Bessel equation, respectively. As a consequence, the angular Mathieu function is transformed into the trigonometric function  $\cos \varphi$  and  $\sin \varphi$ , while the radial Mathieu function become the Bessel function.

Several categories of physical problems can be described by Mathieu equations, like vibrational modes in an elliptical membrane, the propagating modes in elliptical waveguides and water oscillations in lakes of elliptical shapes. Moreover, Mathieu functions are solutions of problems involving periodic motions, like the trajectory of an electron in a periodic array of atoms, quantum pendulum mechanics and floating vessel oscillations. In the following sections we are going to use the Mathieu equations to derive in elliptical coordinates a novel expression of the primary field, produced of the interaction between a circular beam and an elliptical chamber.

### 6.1.3 Calculation of eigenfrequencies

Calculation of cut-off frequencies in an elliptical waveguide requires the determination of the zeros of the modified Mathieu functions of the first kind  $Ce(\mu, q)$  and  $Se(\mu, q)$  and their derivatives [66] [67]. The most direct method of calculating these frequencies is by numerical integration of Equations 6.9 and 6.10. Because the two separation constants  $q$  and  $a$  appear in both equations, the problem has to be solved for both sets of eigenvalues simultaneously, by looking for combinations of  $q$  and  $a$  which satisfy the angular and radial boundary conditions at the same time. The mode frequencies is then obtained by

$$f_{nm} = \frac{c}{2\pi} \sqrt{\frac{q_{nm}}{F^2} + k_z^2}, \quad (6.36)$$

where  $n$  is the index of the angular Mathieu function, indicating the number of oscillations between 0 and  $2\pi$ , and  $m$  is the index of the radial solution corresponding to the  $m$ -th root of  $U_n(q, \mu_0) = 0$  (for TM modes) or  $U'_n(q, \mu_0) = 0$  (for TE modes).

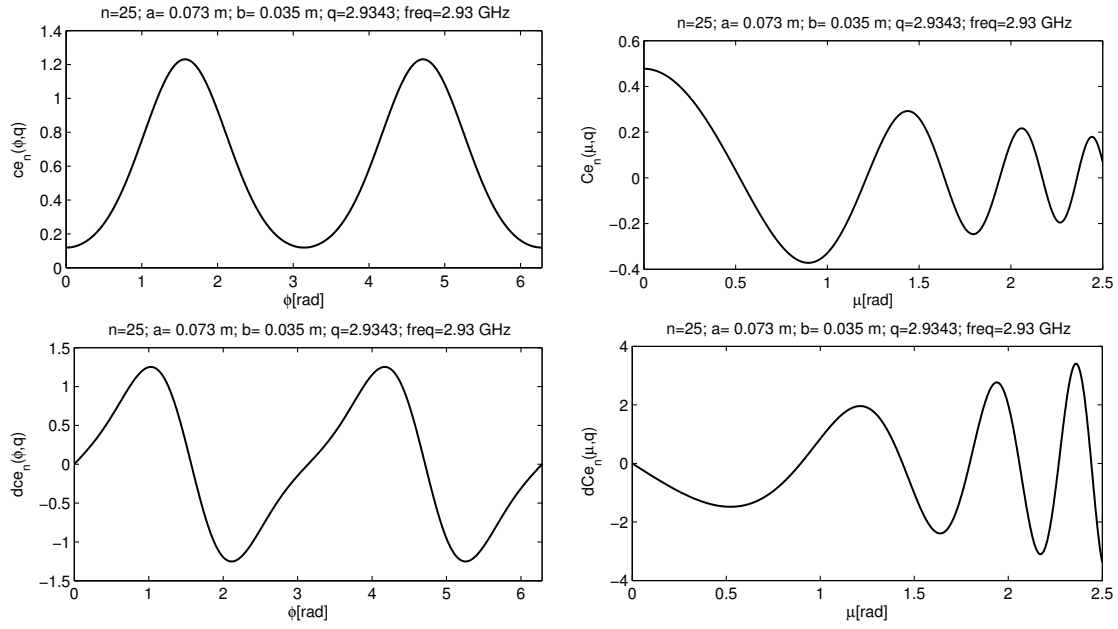


FIGURE 6.2: Angular and radial even Mathieu functions and their derivative calculated for the mode  $TM_{01}^e$  for the main beam chamber of the PS.

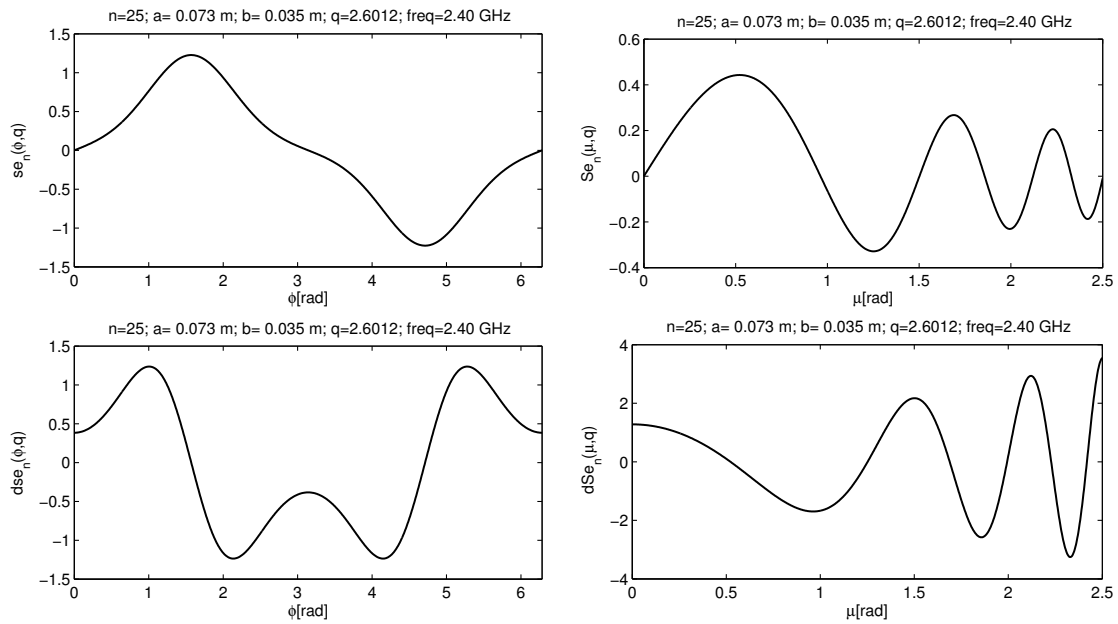


FIGURE 6.3: Angular and radial odd Mathieu functions and their derivative calculated for the odd mode  $TE_{11}^s$  for the main beam chamber of the PS.

The analysis leads to an eigenvalue problem involving an infinite set of eigenvalues  $q_{nm}$ . Some common applications for this boundary value problem is the propagation of electromagnetic or acoustic waves in cylindrical pipes of elliptic cross-section. The Dirichlet boundary condition on  $W(\mu, \varphi)$  applies to the axial component of the electric field intensity for TM modes in waveguides, as well as to the velocity potential of an acoustic mode propagating down a waveguide with acoustically *soft* walls. If  $W(\mu, \varphi)$  represents the axial component of the magnetic field intensity for TE modes, or the acoustic velocity potential for sound waves propagating down an acoustically *hard* wall, then the Neumann boundary condition holds. It has been shown in [72] the existence of special eigenmodes of the elliptical waveguide, called the *whispering gallery* and *bouncing ball* modes. The *whispering gallery* mode in acoustics was observed by Lord Rayleigh in 1910, showing that, at certain high frequencies, sound waves exhibit a particle behavior like a ball sliding along the boundary. Consequently, a person who speaks near the wall of a convex room can be heard across the room near the wall, but not in the interior of the room. Moreover,

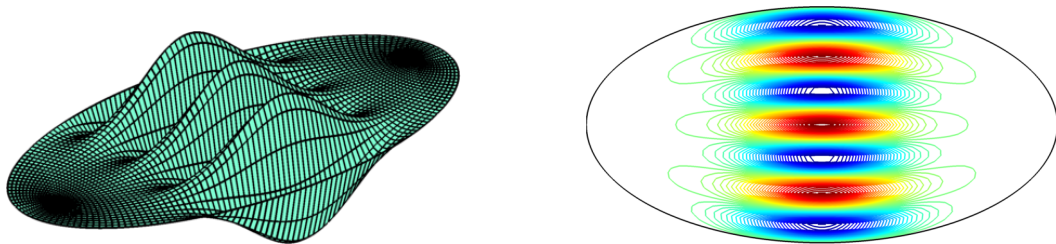


FIGURE 6.4: Perspective view (right) and contour plot (left) of a bouncing ball mode  $TM_{0,4}^e$ .

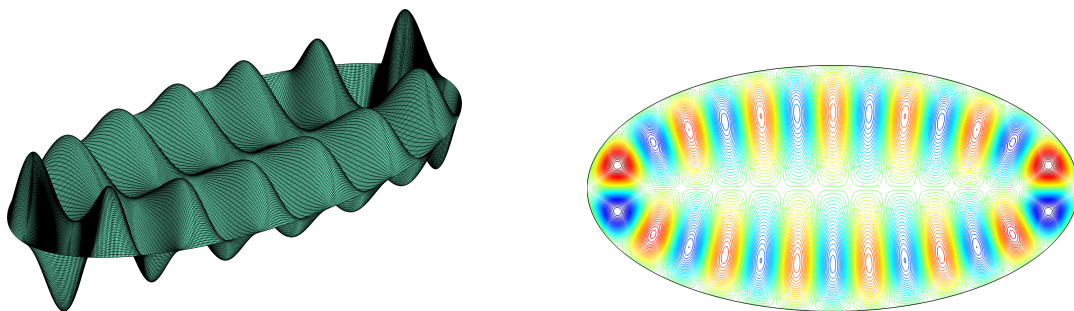


FIGURE 6.5: Perspective view (right) and contour plot (left) of a whispering gallery mode  $TM_{12,1}^e$ .

in quantum mechanics, it is well known that at high energy levels, the distribution of electrons (or “electron clouds”) will be uneven in a bounded open domain, where one can capture an electron with the largest probability only on a proper subdomain. In this type of subdomain, where the eigenfunctions are asymptotically zero except in a thin layer near the boundary, a *whispering gallery* mode can propagate. Another type of subdomain, formed by a thin strip around the line segment which is the shortest diameter of the domain, supports a *bouncing ball* mode, displaying the behavior of a particle bouncing

back and forth on the wall of a waveguide. The eigenfunction decays exponentially fast across the bounding curves of these strips, becoming negligible on the non shaded regions, that corresponds to classically forbidden regions. Both types of modes reflect a strong matter-wave dualism of electrons or other subatomic particles in quantum mechanics.

## 6.2 Primary fields in elliptical coordinates

In this section we want to develop a novel expression, in elliptical coordinates and separate functions of the elliptical variables  $\varphi$  and  $\mu$ , of the electric field  $E_z^0$ , generated by a  $\delta$  beam distribution traveling in an elliptical waveguide. To do that we need to find an expression for the Green function which matches the elliptical system of coordinates. Let us consider the following wave equation for the TM mode:

$$\nabla_t^2 E_z^0 - \frac{k_0^2}{\beta^2 \gamma^2} E_z^0 = G \delta(P - P_0), \quad (6.37)$$

where  $E_z^0$  is the longitudinal component of the electric field,  $jk_0/\beta\gamma$  is the transverse wave number,  $\delta$  is the bi-dimensional Dirac function,  $P_0$  is the position of the particle in the chamber and where  $G$  is a constant depending by the beam parameters and can be calculated as [73]

$$G = -jZ_0 \frac{Qk_0}{\beta^2 \gamma^2}, \quad (6.38)$$

where  $Q$  is particle beam charge, and  $Z_0$  is the characteristic impedance in free space.  $E_z^0$  is given by the superposition of a field produced by the particle beam traveling in the free space, and a term scattered by the elliptical boundary, that acts back on the beam itself. We can then divide the solution of the wave equation in two scalar solutions:

$$E_z^0 = E_z^s + E_z^i. \quad (6.39)$$

The first scalar solution  $E_z^s$  represent the *direct* (or *primary*) component of the field, and has to satisfy the inhomogeneous wave equation in free space and verify the conditions of radiation in the free space:

$$\nabla_t^2 E_z^s - \frac{k_0^2}{\beta^2 \gamma^2} E_z^s = G \delta(P_0), \quad (6.40)$$

The direct field is represented by a  $\delta$  function in the origin.

The second scalar solution  $E_z^i$  is the *indirect* component of the source field, that is the field scattered from the elliptic contour. The indirect field has to satisfy the homogeneous wave equation in free space

$$\nabla_t^2 E_z^i - \frac{k_0^2}{\beta^2 \gamma^2} E_z^i = 0, \quad (6.41)$$

and verify the conditions of radiation in the free space, showing a finite value in the origin. We are going to calculate separately the two contributions of  $E_z^0$  field, considering that the sum of the direct and indirect field must satisfy the boundary condition on the contour of the elliptical waveguide.

### 6.2.1 Direct field (primary field)

An expression of the direct field generated by a  $\delta$  distribution in a circular waveguide, that is a solution of Eq. 6.40, is given by [73]

$$E_z^s = GK_0 \left( \frac{k_0 r}{\beta \gamma} \right), \quad (6.42)$$

where  $r$  is the radius of the circular geometry and  $K_0$  is the zero order modified Bessel function. This expression allows to calculate the Green function in free space in circular coordinates. We want to develop an analogous expression in elliptical coordinates. To do that we can substitute the variable  $r$  with the elliptical variables  $\varphi$  and  $\mu$ :

$$E_z^s = GK_0 \left( \frac{k_0 F}{\beta \gamma} \sqrt{\sinh^2 \mu + \cos^2 \varphi} \right). \quad (6.43)$$

We have to develop the modified Bessel function  $K_0$  in separate functions of the elliptic variables  $\mu$  and  $\varphi$ , using the half angle formula

$$K_0 \left( \frac{k_0 F}{\beta \gamma} \sqrt{\sinh^2 \mu + \cos^2 \varphi} \right) = K_0 \left( \frac{k_0 F}{2\beta \gamma} \sqrt{e^{-2\mu} + e^{2\mu} - 2\cos(2\varphi + \pi)} \right), \quad (6.44)$$

and considering Gegenbauer's addition theorem [74] for modified Bessel functions ( $z_1 < z_2$ ):

$$K_0 \left( \frac{k_0 F}{2\beta \gamma} \sqrt{z_1^2 + z_2^2 - 2z_1 z_2 \cos \varphi} \right) = \sum_{n=0}^{\infty} \epsilon_n I_n(z_1) K_n(z_2) \cos n\varphi \quad (6.45)$$

where

$$\epsilon_n = \frac{2}{1 + \delta_{n,0}}, \quad (6.46)$$

being  $\delta_{n,0}$  the Kronecker delta (equal to 1 for  $n = 0$  and equal to 0 elsewhere).  $I_n$  and  $K_n$  are the Modified Bessel function of first and second kind and  $n$ -th order, respectively. Using Gegenbauer's theorem, we have obtained an expression of  $E_z^s$  given by two separate functions of  $\mu$  and  $\varphi$ :

$$E_z^s = \sum_{n=0}^{\infty} (-1)^n \epsilon_n I_n \left( \frac{k_0 F}{2\beta \gamma} e^{-\mu} \right) K_n \left( \frac{k_0 F}{2\beta \gamma} e^{\mu} \right) \cos 2n\varphi. \quad (6.47)$$

We want now to express Eq. 6.47 in term of Mathieu's functions, expanding  $\cos 2n\varphi$  in terms of angular Mathieu functions for negative values of the eigenvalue  $q$ :

$$\epsilon_n \cos 2n\varphi = \sum_{l=0}^{\infty} S_{2l}^{(2n)} ce_{2l}(\varphi, -q). \quad (6.48)$$

We can multiply both sides of Eq. 6.48 for the Mathieu function  $ce_{2p}(\varphi, -q)$  and integrate between 0 and  $2\pi$ :

$$\epsilon_n \int_0^{2\pi} \cos 2n\varphi ce_{2p}(\varphi, -q) d\varphi = \sum_{l=0}^{\infty} S_{2l}^{(2n)} \int_0^{2\pi} ce_{2l}(\varphi, -q) ce_{2p}(\varphi, -q) d\varphi. \quad (6.49)$$

Let us now consider the orthogonality properties of Mathieu's functions [68]. Being

$$\int_0^{2\pi} ce_{2l}(\varphi, -q) ce_{2p}(\varphi, -q) d\varphi = \pi, \quad (6.50)$$

Equation 6.49 becomes

$$\epsilon_n \int_0^{2\pi} \cos 2n\varphi ce_{2p}(\varphi, -q) d\varphi = \pi S_{2p}^{(2n)}. \quad (6.51)$$

If we consider the following expansion for the angular Mathieu functions for a negative value of the eigenvalue  $q$  [68]

$$ce_{2p}(\varphi, -q) = (-1)^p \sum_{m=0}^{\infty} (-1)^m A_{2m}^{(2p)} \cos 2m\varphi \quad (6.52)$$

we obtain the following identity:

$$\epsilon_n \int_0^{2\pi} \cos 2n\varphi (-1)^p \sum_{m=0}^{\infty} (-1)^m A_{2m}^{(2p)} \cos 2m\varphi d\varphi = \pi S_{2p}^{(2n)}. \quad (6.53)$$

The integral is always zero for  $n \neq m$ . The sign of summation disappears and all the terms are calculated in  $n = m$ :

$$\epsilon_n \int_0^{2\pi} \cos 2n\varphi \cos 2n\varphi d\varphi = \epsilon_n \begin{cases} \pi & n > 0 \\ 2\pi & n = 0 \end{cases} \quad (6.54)$$

Finally Eq. 6.48 becomes

$$2\pi (-1)^{n+p} A_{2n}^{(2p)} = \pi S_p^n, \quad (6.55)$$

where the harmonic function has been developed in Mathieu functions as follows

$$\epsilon_n \cos 2n\varphi = 2(-1)^n \sum_{l=0}^{\infty} (-1)^l A_{2n}^{(2l)} ce_{2l}(\varphi, -q). \quad (6.56)$$

Equation 6.43 can be rewritten as

$$E_z^s = 2G \sum_{l=0}^{\infty} (-1)^l ce_{2l}(\varphi, -q) \sum_{n=0}^{\infty} A_{2n}^{(2l)} I_n \left( \frac{k_0 F}{2\beta\gamma} e^{-\mu} \right) K_n \left( \frac{k_0 F}{2\beta\gamma} e^{\mu} \right), \quad (6.57)$$

and if we consider Eq. 2.18.(2) in [68], we obtain the following novel expression for the Green function in free space in elliptical coordinates and separate functions of  $\varphi$  and  $mu$

$$E_z^s = 2G \sum_{l=0}^{\infty} ce_{2l} \left( \frac{\pi}{2} - \varphi, q \right) \sum_{n=0}^{\infty} A_{2n}^{(2l)} I_n \left( \frac{k_0 F}{2\beta\gamma} e^{-\mu} \right) K_n \left( \frac{k_0 F}{2\beta\gamma} e^{\mu} \right), \quad (6.58)$$

where  $A_{2n}^{(2l)}$  are the Fourier expansion coefficients of the even Mathieu function of order  $(2n)$ -th. We verified that the Green function in free space, expanded in elliptical coordinates and represented by Eq. 6.58, is rapidly convergent thanks to the expansion in terms of Mathieu and Bessel functions.

Let us consider now the following expansion of the radial Mathieu function  $Fek_{2l}(\mu, -q)$  [68] for negative values of the eigenvalue  $q$ :

$$Fek_{2l}(\mu, -q) = \frac{p'_{2l}}{\pi A_0^{(2l)}} \sum_{n=0}^{\infty} A_{2n}^{(2l)} I_n \left( \frac{k_0 F}{2\beta\gamma} e^{-\mu} \right) K_n \left( \frac{k_0 F}{2\beta\gamma} e^{\mu} \right), \quad (6.59)$$

where

$$p'_{2l} = (-1)^l p_{2l} = (-1)^l \frac{ce_{2l}(0, q) ce_{2l}(\frac{\pi}{2}, q)}{A_0^{(2l)}}, \quad (6.60)$$

and  $A_0^{(2l)}$  are the expansion Fourier coefficients of the even Mathieu function of zero order. If we substitute the expansion of function  $Fek_{2l}(\mu, -q)$  in Eq. 6.64, the Green function can be written in a more compact form

$$E_z^s = 2\pi G \sum_{l=0}^{\infty} \frac{(-1)^l A_0^{(2l)}}{p_{2l}} ce_{2l} \left( \frac{\pi}{2} - \varphi, q \right) Fek_{2l}(\mu, -q). \quad (6.61)$$

For the Green function calculation, several expansions of the function  $Fek_{2l}(\mu, -q)$  have been considered [68]. Nevertheless, has been observed that the expansion 6.59, because of the product between the modified Bessel functions  $I_n$  and  $K_n$ , provides the best convergent behavior. Since the Green function in free space must exhibit the same configuration independently from the coordinate system that has been adopted, we can compare the new expansion 6.64 in elliptical coordinates with the existing expansion 6.43 in circular coordinates. To compare the two expansions we need to transform Eq. 6.58 in function of the circular radial coordinate  $r$  and not on the elliptical radial coordinate  $\mu$ . Calculating the direct field in the angular coordinates  $\varphi_0 = \pi/2$  and substituting in Eq. 6.4, we obtain

that

$$r = F \sinh \mu = \frac{F}{2} (e^\mu - e^{-\mu}). \quad (6.62)$$

After some manipulations, we can apply the following variables substitution

$$\begin{aligned} Fe^\mu &= \sqrt{r^2 + F^2} + r \\ Fe^{-\mu} &= \sqrt{r^2 + F^2} - r \end{aligned} \quad (6.63)$$

in Eq. 6.58, obtaining

$$E_z^s = 2G \sum_{l=0}^{\infty} ce_{2l} \left( \frac{\pi}{2} - \varphi, q \right) \sum_{n=0}^{\infty} A_{2n}^{(2l)} I_n \left( \frac{k_0(\sqrt{r^2 + F^2} + r)}{2\beta\gamma} \right) K_n \left( \frac{k_0(\sqrt{r^2 + F^2} - r)}{2\beta\gamma} \right). \quad (6.64)$$

that can be directly compared with the expansion in 6.43.

In Fig. 6.6 are shown some examples of the Green function in free space calculated with Eq. 6.43 (black line) and 6.64 (red line). The two curves converge in most of the situations for small values of the summation index  $n$ . A better convergence is obtained for small dimension of the radius and low frequencies.

### 6.2.2 Indirect field (Scattered field)

The indirect component of  $E_z^0$  can be represented as an expansion of Mathieu radial and angular functions

$$E_z^i = 2\pi G \sum_{l=0}^{\infty} M_{2l} ce_{2l} \left( \frac{\pi}{2} - \varphi, q \right) Ce_{2l}(\mu, -q), \quad (6.65)$$

where  $M_{2l}$  is an unknown amplitude. The total field produced by the beam in the elliptical vacuum chamber is, therefore, given by the sum of the direct and indirect field, as following:

$$\begin{aligned} E_z^s + E_z^i &= 2\pi G \sum_{l=0}^{\infty} \frac{(-1)^l A_0^{(2l)}}{p_{2l}} ce_{2l} \left( \frac{\pi}{2} - \varphi, q \right) Fe_{2l}(\mu, -q) \\ &\quad + 2\pi G \sum_{l=0}^{\infty} M_{2l} ce_{2l} \left( \frac{\pi}{2} - \varphi, q \right) Ce_{2l}(\mu, -q). \end{aligned} \quad (6.66)$$

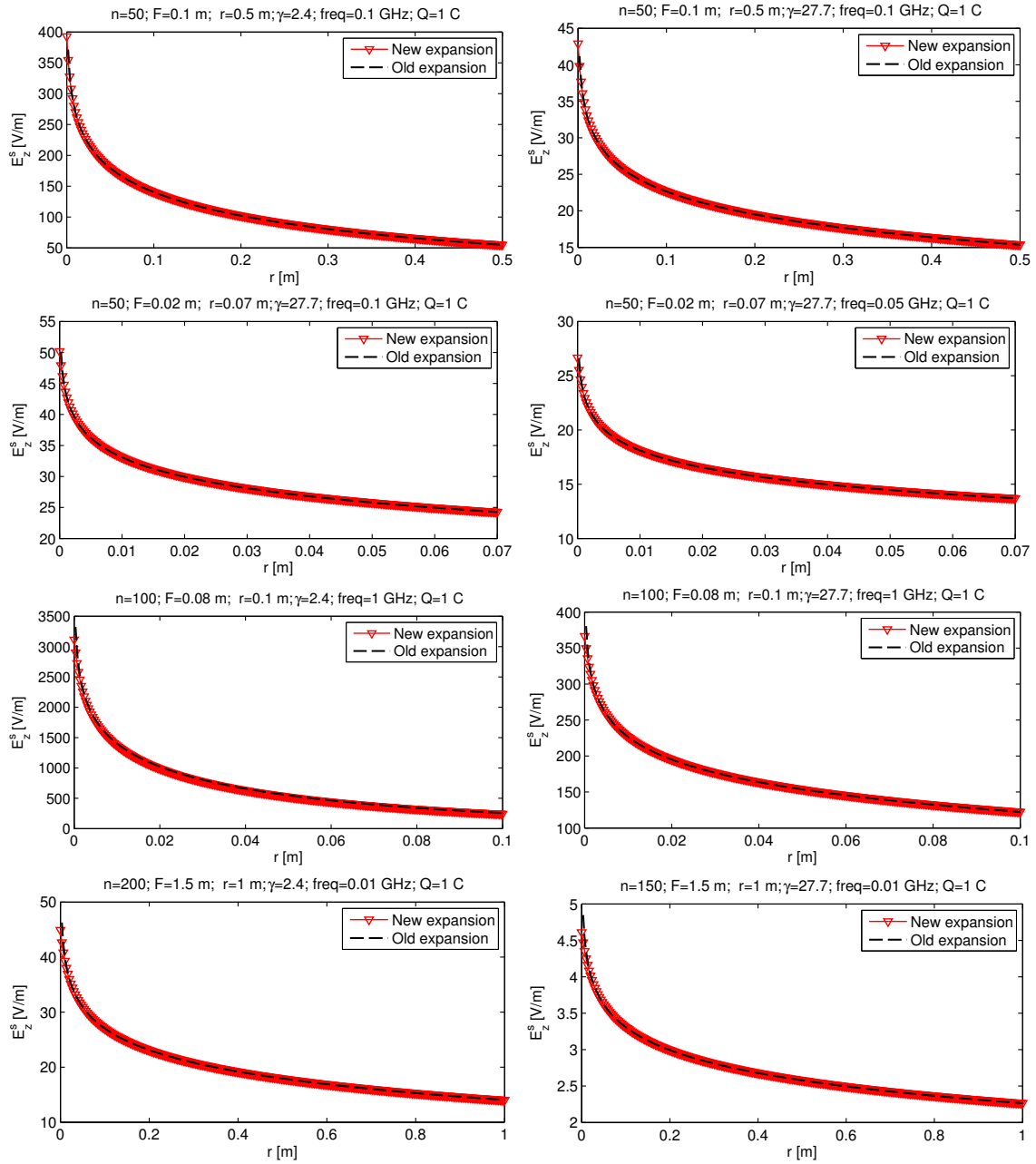


FIGURE 6.6: Green functions (direct component of the source field) in free space calculated with Eq. 6.43 (black line) Eq. 6.64 (red line).

In a generic elliptic waveguide, the previous equation has to satisfy the boundary conditions on the elliptic surface  $\mu = \mu_1$  for every value of  $\varphi$ :

$$\begin{aligned} 2\pi G \sum_{l=0}^{\infty} \frac{(-1)^l A_0^{(2l)}}{p_{2l}} ce_{2l} \left( \frac{\pi}{2} - \varphi, q \right) Fek_{2l}(\mu_1, -q) \\ + 2\pi G \sum_{l=0}^{\infty} M_{2l} ce_{2l} \left( \frac{\pi}{2} - \varphi, q \right) Ce_{2l}(\mu_1, -q) = 0. \end{aligned} \quad (6.67)$$

Being Mathieu's function a complete set of orthogonal functions, Eq. 6.67 must verify

$$\frac{(-1)^l A_0^{(2l)}}{p_{2l}} Fek_{2l}(\mu_1, -q) = -M_{2l} Ce_{2l}(\mu_1, -q), \quad (6.68)$$

or rather

$$M_{2l} = -\frac{(-1)^l A_0^{(2l)}}{p_{2l}} \frac{Fek_{2l}(\mu_1, -q)}{Ce_{2l}(\mu_1, -q)}. \quad (6.69)$$

Knowing the amplitude  $M_{2l}$  allows to calculate the expression of the indirect (scattered) field:

$$E_z^i = -2\pi G \sum_{l=0}^{\infty} \frac{(-1)^l A_0^{(2l)}}{p_{2l}} \frac{Fek_{2l}(\mu_1, -q) Ce_{2l}(\mu, -q)}{Ce_{2l}(\mu_1, -q)} ce_{2l} \left( \frac{\pi}{2} - \varphi, q \right). \quad (6.70)$$

Using the definition of the function  $Fek_{2l}(\mu, -q)$  in Eq. 6.59 we obtain

$$E_z^i = -2G \sum_{l=0}^{\infty} \frac{Ce_{2l}(\mu, -q)}{Ce_{2l}(\mu_1, -q)} ce_{2l} \left( \frac{\pi}{2} - \varphi, q \right) \sum_{n=0}^{\infty} A_{2n}^{(2l)} I_n \left( \frac{k_0 F}{2\beta\gamma} e^{-\mu_1} \right) K_n \left( \frac{k_0 F}{2\beta\gamma} e^{\mu_1} \right), \quad (6.71)$$

that represents the Green function response to the elliptical boundary in elliptical coordinates and separate functions of  $\varphi$  and  $\mu$ .

### 6.2.3 Total field in elliptic coordinates

The total field  $E_z^0$  scattered by a  $\delta$  beam distribution in a vacuum chamber of elliptic cross section is expressed in term of expansion of Mathieu functions  $ce_{2l}(\varphi, -q)$ ,  $Fek_{2l}(\mu, -q)$  and  $Ce_{2l}(\mu, -q)$  for negative values of the eigenvalue  $q$ . The final expansion of the total field is given by

$$E_z^0 = 2\pi G \sum_{l=0}^{\infty} \left( \frac{A_0^{(2l)}}{p_{2l}} \right)^2 ce_{2l}(\varphi, -q) \left( Fek_{2l}(\mu, -q) - \frac{Fek_{2l}(\mu_1, -q) Ce_{2l}(\mu, -q)}{Ce_{2l}(\mu_1, -q)} \right), \quad (6.72)$$

that satisfies the boundary conditions on the contour of the ellipse. In Fig. 6.7 some examples of the total field, calculated as a function of the coordinate  $\varphi$  for a given value of

$\mu$ , are shown. PS machine parameters have been chosen for the calculation of the constant parameter  $G$ : in particular, the parameter  $\gamma = 2.4$  corresponds to the PS injection energy, while  $\gamma = 27.7$  corresponds to top energy. The dimensions of the elliptical waveguide has been chosen to be  $a = 7.3$  cm and  $b = 3.5$  cm, that is the dimension of a standard beam tube of the PS machine. Thanks to the expansion of the function  $Fek_{2l}(\mu, -q)$  in term of modified Bessel function of the first and second kind, Eq. 6.72 converges in all the cases considered for values of the summation index  $n$  smaller that 100. Moreover, a faster convergence is assured for small values of the eigenvalue  $q$ .

## Conclusions

In this chapter, a novel formulation for the field produced by a  $\delta$  beam distribution traveling inside a tube of elliptical cross section, has been determined. The solution, in terms of Mathieu and modified Bessel functions, is rapidly convergent and has been obtained separating the contribution of the Green function, that is the field of the charge generated in free space (direct field) from the contribution of the field scattered by the charge on the elliptical boundary (indirect field). The novel expansion of the direct field, expressed in elliptical coordinates, has been compared with the expansion in circular coordinates, showing very good agreement for different combinations of parameters and summation order. This new result allows a better understanding of the electromagnetic propagation and scattering phenomena that occur in elliptical beam chambers while crossed by a particle beam. Moreover, the total field represents the known term of a system of equations for the calculation of the longitudinal impedance of a step transition between two elliptical beam chambers. The calculation of the primary field in elliptical coordinates an separate function of the elliptical variables, is then a necessary requirement for the step transition impedance calculation, that is shown in the next chapter.

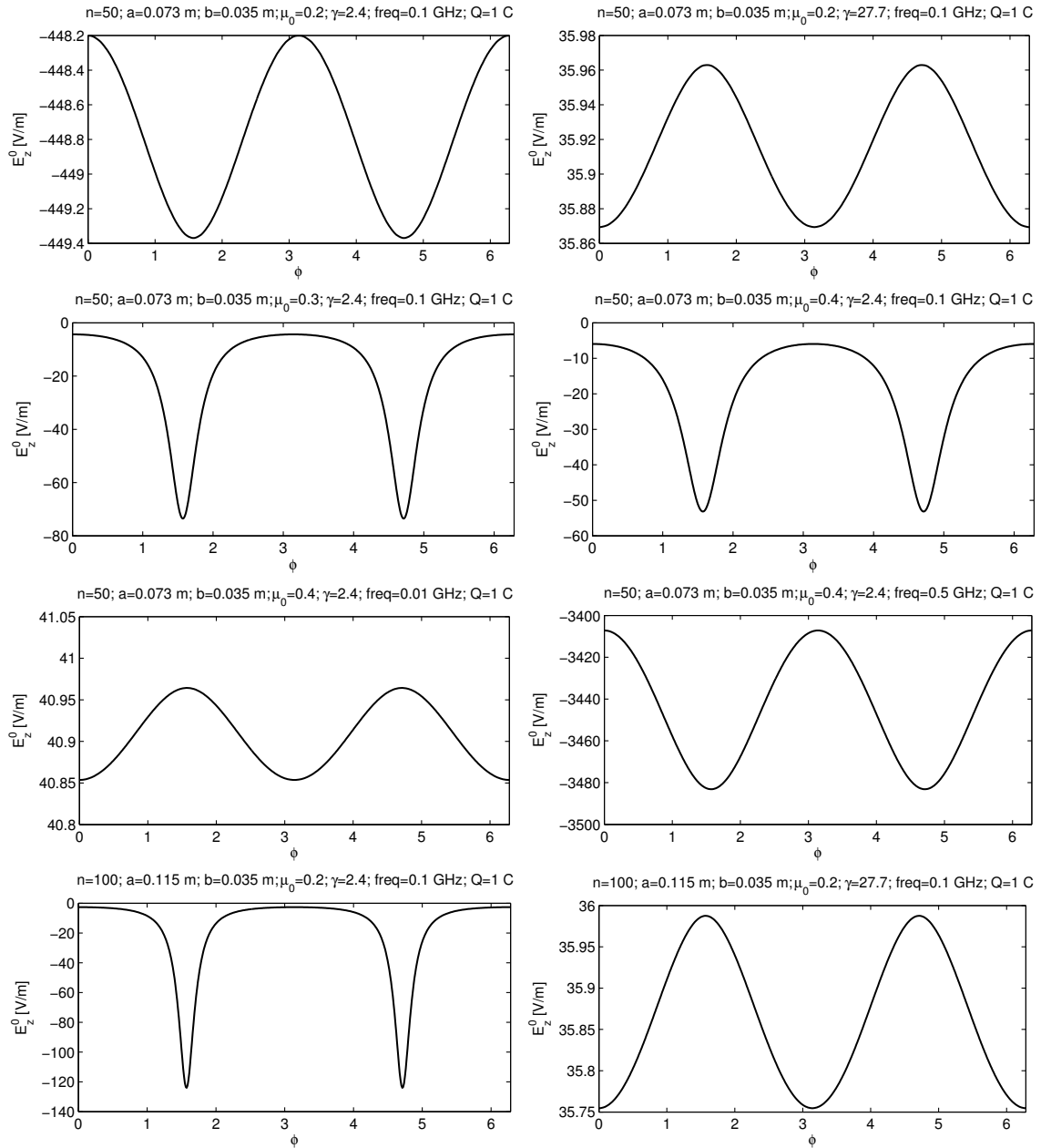


FIGURE 6.7: PS parameters dependency of the primary field calculated in function of the elliptical coordinate  $\varphi$  for a given value of  $\mu_0$ .



## Chapter 7

# Beam coupling impedance of elliptical-elliptical step transitions

### 7.1 Fields and impedance of a circular step transition

Let us consider a particle beam traveling in a tube with circular cross section, encountering an obstacle represented by a step transition to another beam pipe with smaller or larger circular cross section, as shown in Fig. 7.1. When the beam crosses the discontinuity in the vacuum chamber, scattered fields are generated by the sharp edges. This diffracted field is such to restore the boundary condition at the pipe walls, generating an energy loss. Two different effects contribute to the energy loss in the vacuum chamber with step transitions. In the so called *step-out case*, when the charge crosses the discontinuity from a smaller to a larger tube, the primary field has to restore the boundary conditions filling the extra space  $a \leq r \leq b$  between the two pipes, where  $a$  is the radius of the smaller tube and  $b$  the radius of the larger tube. At the same time, the scattered field, generated by

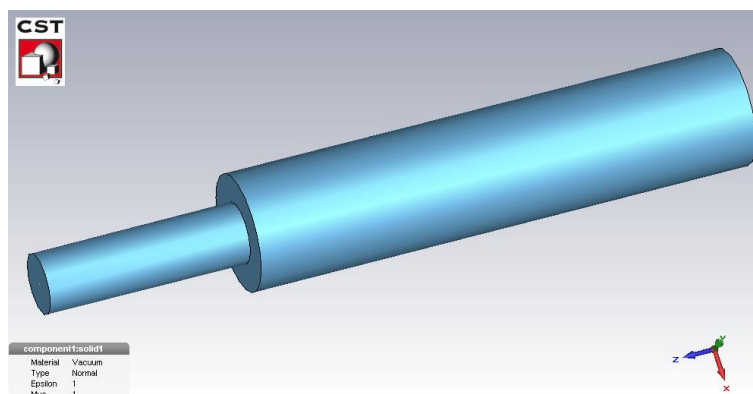


FIGURE 7.1: Step-out discontinuity in a beam pipe.

the radiation phenomena at the sharp edge, propagates into the pipes. Both these effects lead to an energy loss that can be put as [? ]:

$$q^2 k^{out} = U(a < r < b) + E_{rad}, \quad (7.1)$$

where  $q$  is the beam charge,  $k^{out}$  is the loss factor,  $U(a < r < b)$  is the energy necessary to fill the extra region after the discontinuity and  $E_{rad}$  is the energy radiated at the edges that has to restore the boundary conditions. In the *step-in* case, when the charge crosses the discontinuity from a bigger to a smaller tube, the effects that lead to an energy loss can be put as

$$q^2 k^{in} = -U(a < r < b) + E_{rad}, \quad (7.2)$$

where the negative sign is due to a gain of energy with respect to the step-out case. The radiated energy is reflected back with respect to the particle motion without changing its kinetic energy, so it is verified that

$$q^2 k^{in} \approx 0 \quad (7.3)$$

and

$$U(a < r < b) \approx E_{rad}, \quad (7.4)$$

meaning that the energy lost for the radiation process is compensated by the energy gained from the fact that the field has to fill a smaller region. In general, the radiated field  $E_{rad}$  depends by the bunch length of the particle beam. The effects are usually significant only in high frequency ranges, excited by short bunches. Table 7.1 shows that the loss factor in the vacuum chamber is higher in the case of the step out discontinuity, but decreases increasing the length of the bunch. We considered two different case: a step-in transition from a circular cross section of radius  $a = 4$  cm and length 20 cm to a cross section of radius  $b = 2$  cm and length of 50 and the opposite case of a step-out transition. The

$\sigma_b$ [cm]	$k$ [V/pC] Step-in	$k$ [V/pC] Step-out
1	$1.546547 \cdot 10^{-1}$	$-5.203049 \cdot 10^{-1}$
2	$1.471847 \cdot 10^{-1}$	$-1.992717 \cdot 10^{-1}$
3	$1.128623 \cdot 10^{-1}$	$-1.170020 \cdot 10^{-1}$

TABLE 7.1: Comparison between loss factors  $k$  in the step-in and step-out case for different bunch lengths  $\sigma_b$  (values calculated with CST Particle Studio).

sign of the loss factor is here considered positive when the wake potential curve shows a gain of energy and negative in case it shows a loss of energy. In the step-in case the real part of the impedance has an initial negative value (gain of energy), and vanishes at high frequencies above cut-off that, as shown in Fig. 7.2. Just after the beam pipe cut-off, the impedance shows a resonant peak, corresponding to the fundamental mode  $TM_{10}$ , and then reaches a constant asymptotic value for high frequencies. In the step-out case, the

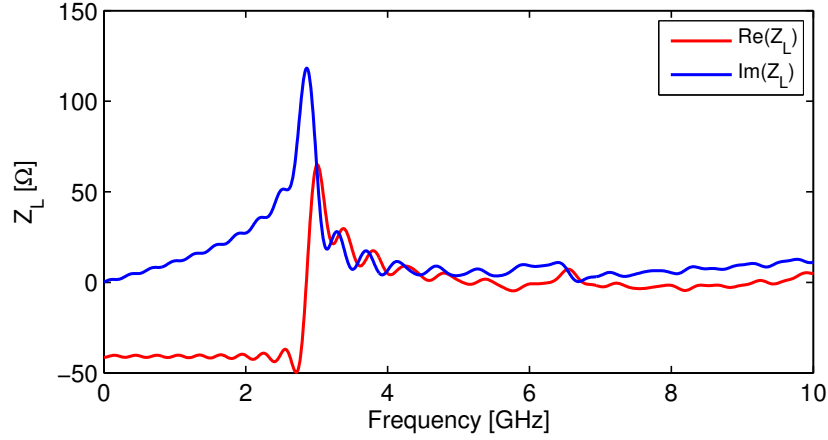


FIGURE 7.2: Longitudinal coupling impedance for a 1 cm length Gaussian bunch passing into a step-in transition calculated with CST Particle Studio.

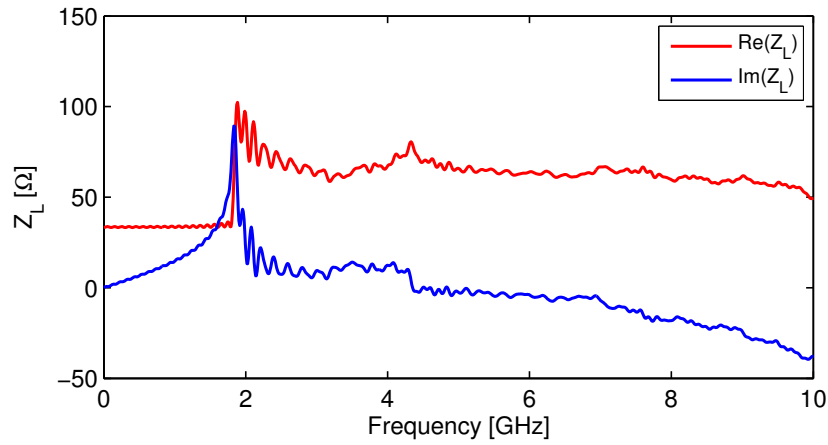


FIGURE 7.3: Longitudinal coupling impedance for a 1 cm length Gaussian bunch passing into a step-out transition calculated with CST Particle Studio.

real part of the impedance has a positive value (loss of energy), as shown in Fig. 7.3. The asymptotic behavior of the real part of the impedance is:

$$Z_L^{in} \simeq 0 \quad (7.5)$$

for the step-in case, and

$$Z_L^{out} \simeq \frac{Z_0}{\pi} \ln \left( \frac{b}{a} \right) \quad (7.6)$$

for the step-out case.

Let us consider now a structure with two symmetric step transitions, as shown in Fig. 7.4. A bunch that loses energy in a step-out transition can regain the same amount of energy passing through a following step-in. Therefore, if a long bunch crosses a pipe enlargement formed by a step-out and step-in sequence with same radii, the total energy loss will be almost zero (see Table 7.2). In Fig. 7.5 the coupling impedance of a step-out and step-in sequence with same radii ( $a=2$  cm,  $b=4$  cm), is shown.

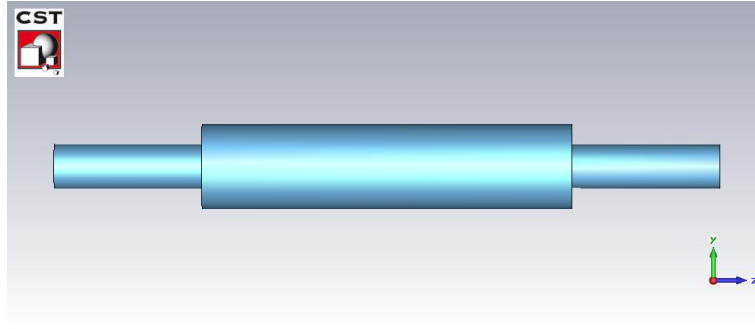


FIGURE 7.4: Symmetric step discontinuity in a beam pipe.

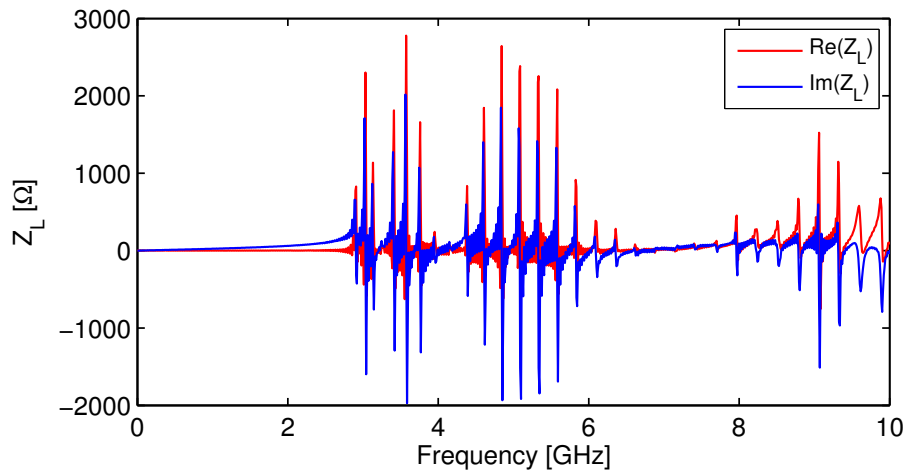


FIGURE 7.5: Longitudinal beam coupling impedance of a symmetric step discontinuity.

TABLE 7.2: Loss factors  $k$  of a structure with two symmetric step transitions calculated with different bunch lengths  $\sigma_b$  with CST Particle Studio.

$\sigma_b$ [cm]	$k$ [V/pC]	Step-out-in
1	$3.909115 \cdot 10^{-1}$	
2	$4.993004 \cdot 10^{-2}$	
3	$3.832365 \cdot 10^{-3}$	

## 7.2 Tapers

Using gradual tapers as the one shown in Fig. 7.6, instead of the abrupt step transitions in particle accelerators tube, the total energy loss may be reduced: long tapers allow to eliminate the sharp edges reducing the radiated energy  $E_{rad}$  to zero. For a point charge we have [75]:

$$k_{taper}^{out} \sim \frac{U(a < r < b)}{q^2} = \frac{1}{2} k_{step}^{out} \quad (7.7)$$

and

$$k_{taper}^{in} \sim -\frac{U(a < r < b)}{q^2} = -\frac{1}{2} k_{step}^{in}. \quad (7.8)$$

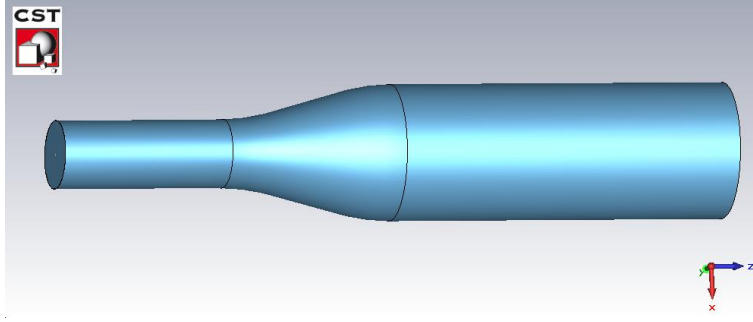


FIGURE 7.6: Step in discontinuity with a gradual smooth taper.

It means that, in the limit of long tapers, the loss factor of a taper-out reaches half the value of the loss factor for a step-out. This is true only for short bunches: for long bunches, when the diffraction effects become negligible, the loss factor tends to be almost the same of the case of the abrupt discontinuity, approaching an asymptotic value corresponding to the case of no radiation. For example, in the 3 cm bunch length case, the whole bunch spectrum lies below the beam pipe cut-off and no radiation occurs. It can be shown that,

TABLE 7.3: Comparison between loss factors  $k$  expressed in V/pC for a bunch with different lengths  $\sigma_b$  passing by an abrupt discontinuity or a smooth one (values calculated with CST Particle Studio).

$\sigma_b$ [cm]	Step-in	Step-out	Taper-in	Taper-out
1	$1.546547 \cdot 10^{-1}$	$-5.203049 \cdot 10^{-1}$	$3.237683 \cdot 10^{-1}$	$-3.684204 \cdot 10^{-1}$
2	$1.471847 \cdot 10^{-1}$	$-1.992717 \cdot 10^{-1}$	$1.751072 \cdot 10^{-1}$	$-1.753412 \cdot 10^{-1}$
3	$1.128623 \cdot 10^{-1}$	$-1.170020 \cdot 10^{-1}$	$1.178151 \cdot 10^{-1}$	$-1.170970 \cdot 10^{-1}$

for a short bunch length, the dependence of the longitudinal loss factor of a one-sided taper on its angle can be approximated by the formula [75]:

$$k = \frac{Z_0 c}{2\sigma\pi^{3/2}} \left[ 1 - \frac{\tilde{\eta}_1}{2} \right] \ln \frac{b}{a}, \quad (7.9)$$

where

$$\tilde{\eta}_1 = \min \left\{ 1, \frac{g\sigma}{(b-a)^2} \right\}. \quad (7.10)$$

The longitudinal beam coupling impedance of a smooth transition with a 10 cm length taper between two circular tubes of radius  $a=2$  cm and  $b=4$  cm, is shown in Fig.7.7. It must be considered, however, that in circular accelerator, a taper-out transition is usually followed by a taper-in. As it can be easily seen, in a structure with long symmetric tapers, total losses are reduced practically to zero:

$$k_{taper}^{out} + k_{taper}^{in} \simeq 0. \quad (7.11)$$

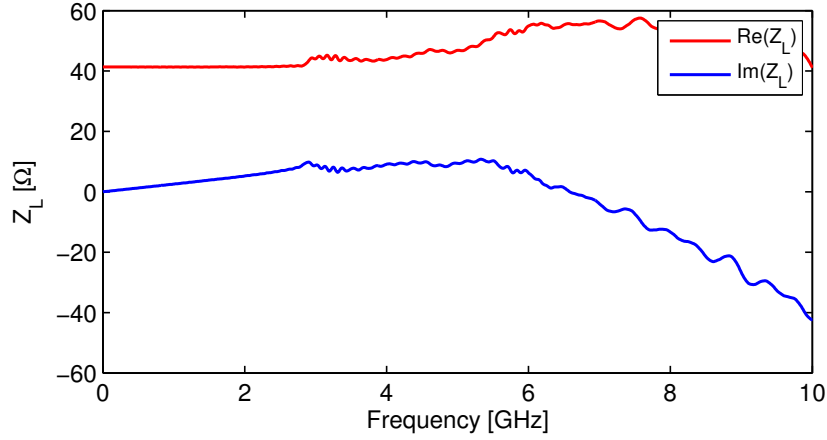


FIGURE 7.7: Longitudinal beam coupling impedance of 10 cm length tapered transition between two circular tubes of radius  $a=2$  cm and  $b=4$  cm, excited by a bunch of  $\sigma=1$  cm.

### 7.3 Simulations with realistic dimensions of the PS pipe

In this section, realistic dimensions of the PS beam pipe and bunch length are taken into account to calculate the impedance of a typical step transition that can be found in the machine. A bunch of 1 cm length travels in a transition between an elliptic beam pipe (major semi-axis 7.3 cm, minor semi-axis 3.5 cm, eccentricity=0.87) of 5 m length and a circular pipe (radius=10 cm) of 1.2 m length. The cut-off frequency of the  $TM_{01}$  mode of the cylindrical pipe is about 1.148 GHz, while the fundamental mode of the elliptical pipe is the even mode  $TE_{11}^c$ , corresponding to a cut-off frequency of 1.22 GHz. In Fig. 7.8 the longitudinal impedance is shown, where one can easily distinguish the cut-off frequency of the circular pipe. If the tube radius were smaller than the major ellipse semi-axis, the cut-off frequency of the step transition would be represented by the even mode  $TM_{01}^c$ , at the frequency of 2.53 GHz. Longitudinal impedance can be determined placing perfect magnetic walls on the XZ and YZ planes of the structure: in this way the force lines of the magnetic field are always perpendicular to the magnetic walls, and the symmetry of the structure allows to reduce by a factor 4 the computation time. This configuration with the beam in the center of symmetry does not allow to excite TE modes, even if, for elliptical waveguide, the even mode  $TE_{11}^c$  is always the fundamental one. The dimensions of the PS circular chamber, that rarely presents a vertical semi-aperture smaller than 10 cm, avoids any high order modes excitation in the range 0-1.14 GHz generated by the transitions.

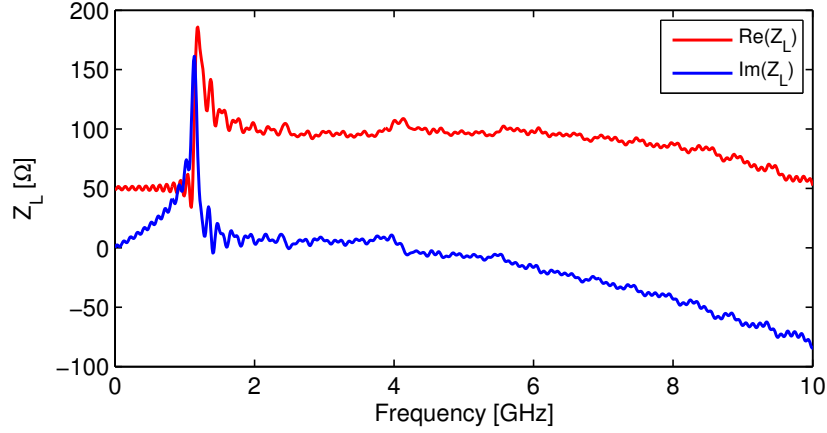


FIGURE 7.8: Longitudinal beam coupling impedance of a step transition between an elliptic beam pipe (major semi-axis 7.3 cm, minor semi-axis 3.5 cm) of and a circular beam pipe (radius=10 cm).

## 7.4 Analytical determination of the impedance of a step transitions between two elliptical beam tubes

In this section we show an analytical method for the evaluation of the longitudinal beam coupling impedance of a step transition between two semi-infinite elliptical waveguides, by means of the mode matching theory [76] [77].

Let us consider a charged particle traveling in the positive direction of the  $z$ -axis of a perfectly conducting vacuum chamber with elliptical cross section. A radiation process will occur because of the discontinuities present near the trajectory of the particle beam. The total diffracted field in the step transition can be described by the superimposition of two terms:

$$E^{tot} = E^{rad} + E^0, \quad (7.12)$$

where  $E^0$  is the field that produced by the charge itself (see Chapter 6) and  $E^{rad}$  is the radiated field from the junction, that is a traveling wave. The sum of this two terms has to satisfy the boundary conditions on the contour and the continuity condition at the interface between the two waveguides.

The field generated by the particle beam, scattered by the discontinuity, will act back on the beam itself, provoking a perturbation on the beam dynamics. This effect can be described by the longitudinal beam coupling impedance, that is defined as [76]

$$Z_L(k) = -\frac{1}{q} \left[ \int_{-\infty}^0 E_{1z}^{rad}(r=0, z) e^{j\frac{kz}{\beta}} dz + \int_0^{+\infty} E_{2z}^{rad}(r=0, z) e^{j\frac{kz}{\beta}} dz \right], \quad (7.13)$$

where  $q$  is the particle charge,  $k = \omega/c$  is the wave number,  $E_{1z}^{rad}$  and  $E_{2z}^{rad}$  are the longitudinal components of the electric field in frequency domain radiated by the step transition

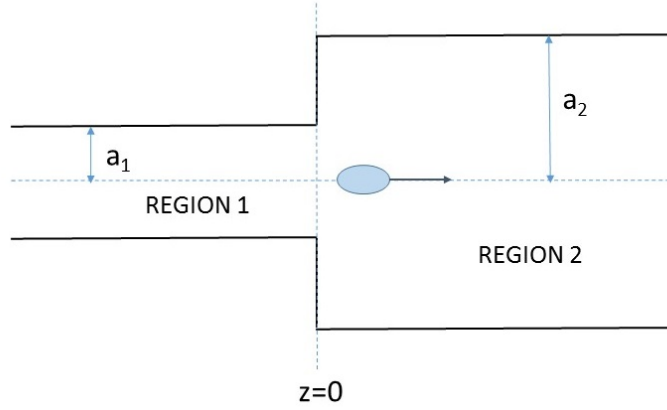


FIGURE 7.9: Step-out transition system between two elliptical waveguides.

in the first and second waveguide. The inverse Fourier transform of the longitudinal impedance describes the longitudinal wake potential

$$W_L(\tau) = \frac{1}{2\pi\epsilon_0 Z_0} \int_{-\infty}^{+\infty} Z_L(k) e^{jck\tau} dk, \quad (7.14)$$

where  $Z_0$  is the characteristic impedance in free space and  $\epsilon_0$  is the permittivity in free space.

The mode matching theory has been chosen to solve the problem. Representing the fields as functional modes allowed to reduce the problem to determine a set of modal amplitudes associated to the modes in the different regions. Using the condition of continuity of the tangential field at the interface, and the orthogonality properties of the modes, we obtain an infinite set of linear equations for the unknown modal amplitudes. Once calculated the modal amplitude of the radiated fields  $E_{1z}^{rad}$  and  $E_{2z}^{rad}$ , we can calculate the coupling impedance of the step transition with Eq. 7.13.

#### 7.4.1 Representation of the fields

Let us consider the geometry shown in Fig. 7.9. In order to calculate the longitudinal impedance for the step transition between two elliptical waveguides, we need to compute the radiated electric field  $E_{1z}^{rad}$  and  $E_{2z}^{rad}$  in the two regions using the mode matching technique. The first step is to expand the unknown fields in the two regions in their respective normal modes. Since the functional form of the normal modes in elliptical waveguide is known, the problem reduces to determine a set of modal amplitudes associated with the fields in the two regions. A particle traveling along the z-axis of an infinite elliptical waveguide may sustain both TE and TM modes. In the elliptical geometry, the source

satisfies both  $x$  and  $y$  specular symmetry; the symmetry with respect to the plane  $y = 0$  is satisfied using the Mathieu functions  $ce(\varphi, q)$  and  $Ce(\mu, q)$ , while the symmetry with respect to the plane  $x = 0$  is satisfied using only even index of the Mathieu functions. The vector modal functions of an elliptical waveguide supporting a TM mode are given by

$$e_{2n}^{(z)}(q_{1,2n,m}^{TM}) = ce_{2n}(\varphi, q_{1,2n,m}^{TM}) Ce_{2n}(\mu, q_{1,2n,m}^{TM}) \quad (7.15)$$

$$h_{2n}^{(z)}(q_{1,2n,m}^{TM}) = 0, \quad (7.16)$$

where  $ce_{2n}(\varphi, q)$  and  $Ce_{2n}(\mu, q)$  are the even angular and radial Mathieu functions and  $q_{1,2n,m}^{TM}$  are the TM eigenvalues in the first and second waveguide, respectively. The vector modal functions of an elliptical waveguide supporting a TE mode are given by

$$e_{2n+2}^{(z)}(q_{1,2n+2,m}^{TE}) = 0 \quad (7.17)$$

$$h_{2n+2}^{(z)}(q_{1,2n+2,m}^{TE}) = se_{2n+2}(\varphi, q_{1,2n+2,m}^{TE}) Se_{2n+2}(\mu, q_{1,2n+2,m}^{TE}), \quad (7.18)$$

where  $se_{2n}(\varphi, q)$  and  $Se_{2n}(\mu, q)$  are the even radial Mathieu functions and  $q_{1,2n+2,m}^{TE}$  are the TE eigenvalues in the first and second waveguide, respectively. The electric and magnetic fields in the two waveguides can be represented by means of the following modal expansions calculated in  $z=0$ :

$$\mathbf{E}_t^{tot} = \begin{cases} \mathbf{E}_{1,t}^0 + \sum_{m=1}^{\infty} \sum_{n=0}^{\infty} \alpha_{12n,m} \mathbf{e}_{2\mathbf{n}}^{(t)}(q_{12n,m}^{TM}) + \sum_{m=1}^{\infty} \sum_{n=0}^{\infty} \beta_{12n+2,m} \mathbf{e}_{2\mathbf{n}}^{(t)}(q_{12n+2,m}^{TE}) \\ \mathbf{E}_{2,t}^0 + \sum_{m=1}^{\infty} \sum_{n=0}^{\infty} \alpha_{22n,m} \mathbf{e}_{2\mathbf{n}}^{(t)}(q_{22n,m}^{TM}) + \sum_{m=1}^{\infty} \sum_{n=0}^{\infty} \beta_{22n+2,m} \mathbf{e}_{2\mathbf{n}}^{(t)}(q_{22n+2,m}^{TE}) \end{cases} \quad (7.19)$$

$$\mathbf{H}_t^{tot} = \begin{cases} \mathbf{H}_{1,t}^0 + \sum_{m=1}^{\infty} \sum_{n=0}^{\infty} \alpha_{12n,m} \mathbf{h}_{2\mathbf{n}}^{(t)}(q_{12n,m}^{TM}) + \sum_{m=1}^{\infty} \sum_{n=0}^{\infty} \beta_{12n+2,m} \mathbf{h}_{2\mathbf{n}}^{(t)}(q_{12n+2,m}^{TE}) \\ \mathbf{H}_{2,t}^0 + \sum_{m=1}^{\infty} \sum_{n=0}^{\infty} \alpha_{22n,m} \mathbf{h}_{2\mathbf{n}}^{(t)}(q_{22n,m}^{TM}) + \sum_{m=1}^{\infty} \sum_{n=0}^{\infty} \beta_{22n+2,m} \mathbf{h}_{2\mathbf{n}}^{(t)}(q_{22n+2,m}^{TE}) \end{cases} \quad (7.20)$$

where  $\mathbf{e}_{2\mathbf{n}}^{(t)}(q_{12n,m}^{TM})$ ,  $\mathbf{e}_{2\mathbf{n}}^{(t)}(q_{22n,m}^{TM})$ ,  $\mathbf{h}_{2\mathbf{n}}^{(t)}(q_{12n+2,m}^{TE})$ ,  $\mathbf{h}_{2\mathbf{n}}^{(t)}(q_{22n+2,m}^{TE})$  are the modal functions and  $\alpha_{12n,m}$ ,  $\alpha_{22n,m}$ ,  $\beta_{12n+2,m}$ ,  $\beta_{22n+2,m}$  are the modal expansion coefficients. The component of the field produced by the charge in the infinite waveguide are given by:

$$\mathbf{E}_t^0 = \begin{cases} 2\pi G \sum_{n=0}^{\infty} \frac{A_0^{(2n)}}{p_{2n}} \{ \mathbf{e}_{2\mathbf{n}}^{(t)} + \mathbf{e}_{1,2\mathbf{n}}^{(t)} \} \\ 2\pi G \sum_{n=0}^{\infty} \frac{A_0^{(2n)}}{p_{2n}} \{ \mathbf{e}_{2\mathbf{n}}^{(t)} + \mathbf{e}_{2,2\mathbf{n}}^{(t)} \} \end{cases} \quad (7.21)$$

$$\mathbf{H}_t^0 = \begin{cases} 2\pi G \sum_{n=0}^{\infty} \frac{A_0^{(2n)}}{p_{2n}} \{ \mathbf{h}_{2\mathbf{n}}^{(t)} + \mathbf{h}_{1,2\mathbf{n}}^{(t)} \} \\ 2\pi G \sum_{n=0}^{\infty} \frac{A_0^{(2n)}}{p_{2n}} \{ \mathbf{h}_{2\mathbf{n}}^{(t)} + \mathbf{h}_{2,2\mathbf{n}}^{(t)} \} \end{cases} \quad (7.22)$$

where  $\mathbf{e}_{2\mathbf{n}}^{(t)}$  and  $\mathbf{h}_{2\mathbf{n}}^{(t)}$  are the modal function associated to the direct field in free space and  $\mathbf{e}_{1,2\mathbf{n}}^{(t)}$  and  $\mathbf{h}_{1,2\mathbf{n}}^{(t)}$  are the modal function associated to the indirect field in the two waveguides. To apply the mode matching technique, we have to impose the conditions of continuity of the tangential component of the electric and magnetic fields at the interface  $z=0$ :

$$\mathbf{E}_t(\varphi, \mu; z = 0^+) = \begin{cases} \mathbf{E}_t(\varphi, \mu; z = 0^-) & \text{in } D_1 \\ 0 & \text{in } D_2 - D_1 \end{cases} \quad (7.23)$$

$$\mathbf{H}_t(\varphi, \mu; z = 0^+) = \mathbf{H}_t(\varphi, \mu; z = 0^-) \quad \text{in } D_1, \quad (7.24)$$

where  $D_1$  and  $D_2$  are the transverse sections of the two waveguides.

#### 7.4.2 Equation 1 (electric field): projection with TM modes

In this section we determine the first equation of the matching system. Let us apply the condition of continuity of the tangential electric field 7.23 at the interface between the two elliptical beam pipe of different cross section:

$$\begin{aligned} \mathbf{E}_{1,t}^0 + \sum_{m=1}^{\infty} \sum_{n=0}^{\infty} \alpha_{12n,m} \mathbf{e}_{2\mathbf{n}}^{(t)}(q_{12n,m}^{TM}) + \sum_{m=1}^{\infty} \sum_{n=0}^{\infty} \beta_{12n+2,m} \mathbf{e}_{2\mathbf{n}}^{(t)}(q_{12n+2,m}^{TE}) = \\ \mathbf{E}_{2,t}^0 + \sum_{m=1}^{\infty} \sum_{n=0}^{\infty} \alpha_{22n,m} \mathbf{e}_{2\mathbf{n}}^{(t)}(q_{22n,m}^{TM}) + \sum_{m=1}^{\infty} \sum_{n=0}^{\infty} \beta_{22n+2,m} \mathbf{e}_{2\mathbf{n}}^{(t)}(q_{22n+2,m}^{TE}). \end{aligned} \quad (7.25)$$

We apply the Ritz-Galerking method to both sides of the previous equation, that consists in scalar multiply for the modal function of second waveguide  $\mathbf{e}_{2\mathbf{r}}^{(t)}(q_{22r,s}^{TM})$  and integrate the two members of the equation in  $D_1$  and  $D_2$ , respectively, obtaining

$$\begin{aligned} \int_{D_1} \mathbf{E}_{1,t}^0 \cdot \mathbf{e}_{2\mathbf{r}}^{(t)}(q_{22r,s}^{TM}) dS + \int_{D_1} \sum_{m=1}^{\infty} \sum_{n=0}^{\infty} \alpha_{12n,m} \mathbf{e}_{2\mathbf{n}}^{(t)}(q_{12n,m}^{TM}) \cdot \mathbf{e}_{2\mathbf{r}}^{(t)}(q_{22r,s}^{TM}) dS + \\ \int_{D_1} \sum_{m=1}^{\infty} \sum_{n=0}^{\infty} \beta_{12n+2,m} \mathbf{e}_{2\mathbf{n}+2}^{(t)}(q_{12n+2,m}^{TE}) \cdot \mathbf{e}_{2\mathbf{r}}^{(t)}(q_{22r,s}^{TM}) dS = \\ \int_{D_2} \mathbf{E}_{2,t}^0 \cdot \mathbf{e}_{2\mathbf{r}}^{(t)}(q_{22r,s}^{TM}) dS + \int_{D_2} \sum_{m=1}^{\infty} \sum_{n=0}^{\infty} \alpha_{22n,m} \mathbf{e}_{2\mathbf{n}}^{(t)}(q_{22n,m}^{TM}) \cdot \mathbf{e}_{2\mathbf{r}}^{(t)}(q_{22r,s}^{TM}) dS + \\ \int_{D_2} \sum_{m=1}^{\infty} \sum_{n=0}^{\infty} \beta_{22n+2,m} \mathbf{e}_{2\mathbf{n}+2}^{(t)}(q_{22n+2,m}^{TE}) \cdot \mathbf{e}_{2\mathbf{r}}^{(t)}(q_{22r,s}^{TM}) dS. \end{aligned} \quad (7.26)$$

We now show how to manipulate the six terms of the first matching equation in order to have a simple form to implement with numerical tools. Let us analyze the second term of the first member of Eq. 7.26. If we consider the following identity (see Appendix A)

$$\frac{1}{(q_r - q_s)} \oint_L \left( q_r V_r \frac{\partial V_s}{\partial n} - q_s V_s \frac{\partial V_r}{\partial n} \right) dl = \int_D \nabla_t V_r \cdot \nabla_t V_s d\varphi d\mu, \quad (7.27)$$

it is verified that

$$\int_{D_1} \mathbf{e}_{2\mathbf{n}}^{(\mathbf{t})} (q_{12n,m}^{TM}) \cdot \mathbf{e}_{2\mathbf{r}}^{(\mathbf{t})} (q_{22r,s}^{TM}) dS = \quad (7.28)$$

$$-\left(\frac{F}{2}\right)^4 \frac{k_{z2,2r,s}^{TM} k_{z1,2n,m}^{TM}}{(q_{12n,m}^{TM} - q_{22r,s}^{TM}) q_{12n,m}^{TM}} \oint_0^{2\pi} \left[ e_{2r}^{(z)} (q_{22r,s}^{TM}) \frac{\partial e_{2n}^{(z)} (q_{12n,m}^{TM})}{\partial \mu} \right]_{\mu=\mu_1} d\varphi.$$

Let us consider now the following identity

$$\int_D \hat{\mathbf{z}} \cdot (\nabla_t U_r \times \nabla_t V_s) dS = - \oint_L U_r \nabla_t V_s \cdot \hat{\mathbf{d}}l = - \oint_L U_r \frac{\partial V_s}{\partial l} dl. \quad (7.29)$$

The third term of the first member of Eq. 7.26 becomes

$$\int_{D_1} \mathbf{e}_{2\mathbf{n}+2}^{(\mathbf{t})} (q_{12n+2,m}^{TE}) \cdot \mathbf{e}_{2\mathbf{r}}^{(\mathbf{t})} (q_{22r,s}^{TM}) dS = \quad (7.30)$$

$$-\left(\frac{F}{2}\right)^4 \frac{Z_0 k_0 k_{z2,2r,s}^{TM}}{q_{12n+2,m}^{TE} q_{22r,s}^{TM}} \oint_0^{2\pi} \left[ h_{2n+2}^{(z)} (q_{12n+2,m}^{TE}) \frac{\partial e_{2r}^{(z)} (q_{22r,s}^{TM})}{\partial \varphi} \right]_{\mu=\mu_1} d\varphi.$$

We analyze now the second term of the second member of Eq. 7.26, that using the identity 7.27 can be written as:

$$\int_{D_2} \mathbf{e}_{2\mathbf{r}}^{(\mathbf{t})} (q_{22r,s}^{TM}) \cdot \mathbf{e}_{2\mathbf{n}}^{(\mathbf{t})} (q_{22n,m}^{TM}) dS \quad (7.31)$$

$$= -\left(\frac{F}{2}\right)^4 \left( \frac{k_{z2,2r,s}^{TM}}{q_{22r,s}^{TM}} \right)^2 \int_{D_2} \nabla_t e_{2r}^{(z)} (q_{22r,s}^{TM}) \cdot \nabla_t e_{2n}^{(z)} (q_{22n,m}^{TM}) dS.$$

We need to consider the following identity

$$\frac{1}{(q_r - q_s)} \oint_L \left( q_r V_r \frac{\partial V_s}{\partial n} - q_s V_s \frac{\partial V_r}{\partial n} \right) dl = \int_D \tilde{\nabla}_t V_r \cdot \tilde{\nabla}_t V_s d\varphi d\mu, \quad (7.32)$$

where the gradients are defined as follow:

$$\tilde{\nabla}_t = \hat{\mu} \frac{\partial}{\partial \mu} + \hat{\varphi} \frac{\partial}{\partial \varphi} = \frac{1}{F \sqrt{\cosh^2 \mu - \cos^2 \varphi}} \left( \hat{\mu} \frac{\partial}{\partial \mu} + \hat{\varphi} \frac{\partial}{\partial \varphi} \right) = \frac{1}{h(\mu, \varphi)} \left( \hat{\mu} \frac{\partial}{\partial \mu} + \hat{\varphi} \frac{\partial}{\partial \varphi} \right). \quad (7.33)$$

For  $n \neq r$  and  $m \neq s$ , that means  $q_{22n,m}^{TM} \neq q_{22r,s}^{TM}$ , the integral in Eq. 7.31 is equal to zero, because the eigenvalue on the elliptic boundary  $\mu = \mu_2$  is zero. If  $n = r$  and  $m = s$ , that means  $q_{22n,m}^{TM} = q_{22r,s}^{TM}$ , if we consider the following identity

$$\int_D \nabla_t V_r \cdot \nabla_t V_s dS = 2q_s \int_D V_r V_s (\cosh 2\mu - \cos 2\varphi) d\varphi d\mu, \quad (7.34)$$

we obtain

$$\int_{D_2} \nabla_t e_{2r}^{(z)}(q_{2r,s}^{TM}) \cdot \nabla_t e_{2r}^{(z)}(q_{2r,s}^{TM}) dS = 2 q_{2r,s}^{TM} \sigma_{2r,s} \quad (7.35)$$

where

$$\sigma_{2r,s} = \int_{D_2} \left[ e_{2r}^{(z)}(q_{2r,s}^{TM}) \right]^2 (\cosh 2\mu - \cos 2\varphi) d\varphi d\mu, \quad (7.36)$$

resulting in an diagonal matrix.

We finally analyze the last term of second member. With some manipulations it can be written as

$$\int_{D_2} \nabla_t e_{2r}^{(z)}(q_{2r,s}^{TM}) \cdot \hat{\mathbf{z}} \times \nabla_t h_{2n+2}^{(z)}(q_{2n+2,m}^{TE}) dS. \quad (7.37)$$

If we apply the identity 7.29, considering the properties of  $e_{2r}^{(z)}(q_{2r,s}^{TM})$  and  $h_{2n+2}^{(z)}(q_{2n+2,m}^{TE})$  on the contour of the ellipse, we obtain that the term is null. As consequence, the second member of Eq. 7.26 is made by the unknown vector  $\alpha_{2r,s}$  multiplied for a known diagonal matrix. Finally, the first matching equation of the system is given by:

$$\begin{aligned} & \int_{D_1} \mathbf{E}_{1,t}^0 \cdot \mathbf{e}_{2r}^{(2t)}(q_{2r,s}^{TM}) dS + \quad (7.38) \\ & - \left(\frac{F}{2}\right)^4 \sum_{n=0}^{\infty} \sum_{m=1}^{\infty} \alpha_{1_{2n,m}} \frac{k_{z_{2,2r,s}}^{TM} k_{z_{1,2n,m}}^{TM}}{(q_{1_{2n,m}}^{TM} - q_{2r,s}^{TM}) q_{1_{2n,m}}^{TM}} \oint_0^{2\pi} e_{2r}^{(z)}(q_{2r,s}^{TM}) \frac{\partial e_{2n}^{(z)}(q_{1_{2n,m}}^{TM})}{\partial \mu} \Big|_{\mu=\mu_1} d\varphi + \\ & - \left(\frac{F}{2}\right)^4 \sum_{n=0}^{\infty} \sum_{m=1}^{\infty} \beta_{1_{2n+2,m}} \frac{k_{z_{2,2r,s}}^{TM} k_0 Z_0}{q_{1_{2n+2,m}}^{TE} q_{2r,s}^{TM}} \oint_0^{2\pi} h_{2n+2}^{(z)}(q_{1_{2n+2,m}}^{TE}) \frac{\partial e_{2r}^{(z)}(q_{2r,s}^{TM})}{\partial \varphi} \Big|_{\mu=\mu_1} d\varphi \\ & = \int_{D_2} \mathbf{E}_{2,t}^0 \cdot \mathbf{e}_{2r}^{(t)}(q_{2r,s}^{TM}) dS - \alpha_{2n,m} \left(\frac{F}{2}\right)^4 \left(\frac{k_{z_{2,2r,s}}^{TM}}{q_{2r,s}^{TM}}\right)^2 2 q_{2r,s}^{TM} \sigma_{2r,s}. \end{aligned}$$

### 7.4.3 Equation 2 (electric field): projection with TE modes

To obtain the second matching equation of the system we apply the Ritz-Galerking method to both sides of Eq. 7.25: we scalar multiply for the modal function of second waveguide

$\widehat{\mathbf{z}} \times \nabla_t h_{2r+2}^{(z)}(q_{2r+2,s}^{TE})$  and integrate in  $D_1$  and  $D_2$ , respectively:

$$\begin{aligned}
& \int_{D_1} \mathbf{E}_{1,t}^0 \cdot \widehat{\mathbf{z}} \times \nabla_t h_{2r+2}^{(z)}(q_{2r+2,s}^{TE}) dS + \\
& \int_{D_1} \sum_{m=1}^{\infty} \sum_{n=0}^{\infty} \alpha_{12n,m} \mathbf{e}_{2\mathbf{n}}^{(t)}(q_{12n,m}^{TM}) \cdot \widehat{\mathbf{z}} \times \nabla_t h_{2r+2}^{(z)}(q_{2r+2,s}^{TE}) dS + \\
& \int_{D_1} \sum_{m=1}^{\infty} \sum_{n=0}^{\infty} \beta_{12n+2,m} \mathbf{e}_{2\mathbf{n}+2}^{(t)}(q_{12n+2,m}^{TE}) \cdot \widehat{\mathbf{z}} \times \nabla_t h_{2r+2}^{(z)}(q_{2r+2,s}^{TE}) dS = \\
& \int_{D_2} \mathbf{E}_{2,t}^0 \cdot \widehat{\mathbf{z}} \times \nabla_t h_{2r+2}^{(z)}(q_{2r+2,s}^{TE}) dS + \\
& \int_{D_2} \sum_{m=1}^{\infty} \sum_{n=0}^{\infty} \alpha_{22n,m} \mathbf{e}_{2\mathbf{n}}^{(t)}(q_{22n,m}^{TM}) \cdot \widehat{\mathbf{z}} \times \nabla_t h_{2r+2}^{(z)}(q_{2r+2,s}^{TE}) dS + \\
& \int_{D_2} \sum_{m=1}^{\infty} \sum_{n=0}^{\infty} \beta_{22n+2,m} \mathbf{e}_{2\mathbf{n}+2}^{(t)}(q_{22n+2,m}^{TE}) \cdot \widehat{\mathbf{z}} \times \nabla_t h_{2r+2}^{(z)}(q_{2r+2,s}^{TE}) dS.
\end{aligned} \tag{7.39}$$

The second term of the first member and the second term of the second member of Eq. 7.39, similarly to Eq. 7.37, are always zero.

Let us analyze now the third term on the first member. If we consider Eq. 7.27, after some manipulation we obtain that

$$\begin{aligned}
& \int_{D_1} \left[ \widehat{\mathbf{z}} \times \nabla_t h_{2n+2}^{(z)}(q_{12n+2,m}^{TE}) \right] \cdot \left[ \widehat{\mathbf{z}} \times \nabla_t h_{2r+2}^{(z)}(q_{2r+2,s}^{TE}) \right] dS = \\
& \frac{q_{12n+2,m}^{TE}}{(q_{12n+2,m}^{TE} - q_{2r+2,s}^{TE})} \oint_0^{2\pi} \left[ h_{2n+2}^{(z)}(q_{12n+2,m}^{TE}) \frac{\partial h_{2r+2}^{(z)}(q_{2r+2,s}^{TE})}{\partial \mu} \right]_{\mu=\mu_1} d\varphi.
\end{aligned} \tag{7.40}$$

Let us consider the third term of the second member: the integral is always zero for  $q_{12n,m}^{TM} \neq q_{12r,s}^{TM}$ , that occurs when  $n \neq m$  and  $r \neq s$ . When  $n = m$  and  $r = s$  we obtain

$$\int_{D_2} \left[ \widehat{\mathbf{z}} \times \nabla_t h_{2r+2}^{(z)}(q_{2r+2,s}^{TE}) \right] \cdot \left[ \widehat{\mathbf{z}} \times \nabla_t h_{2n+2}^{(z)}(q_{22n+2,m}^{TE}) \right] dS = 2q_{2r+2,s}^{TE} \theta_{2r+2,s} \tag{7.41}$$

where

$$\theta_{2r+2,s} = \int_{D_2} \left[ h_{2r+2}^{(z)}(q_{2r+2,s}^{TE}) \right]^2 (\cosh 2\mu - \cos 2\varphi) d\varphi d\mu. \tag{7.42}$$

With some manipulations we obtain the second matching equation of the system:

$$\begin{aligned}
& \int_{D_1} \mathbf{E}_{1,t}^0 \cdot \hat{\mathbf{z}} \times \nabla_t h_{2r+2}^{(z)}(q_{2r+2,s}^{TE}) dS + \tag{7.43} \\
& j \left( \frac{F}{2} \right)^2 \sum_{n=0}^{\infty} \sum_{m=1}^{\infty} \beta_{1_{2n+2},m} \frac{k_0 Z_0}{(q_{1_{2n+2},m}^{TE} - q_{2r+2,s}^{TE})} \oint_0^{2\pi} \left[ h_{2n+2}^{(z)}(q_{1_{2n+2},m}^{TE}) \frac{\partial h_{2r+2}^{(z)}(q_{2r+2,s}^{TE})}{\partial \mu} \right]_{\mu=\mu_1} d\varphi = \\
& \int_{D_2} \mathbf{E}_{2,t}^0 \cdot \hat{\mathbf{z}} \times \nabla_t h_{2r+2}^{(z)}(q_{2r+2,s}^{TE}) dS - j \left( \frac{F}{2} \right)^2 2k_0 Z_0 \theta_{2r+2,s} \beta_{2_{2r+2},s} + \\
& j \left( \frac{F}{2} \right)^2 \sum_{n=0}^{\infty} \sum_{m=1}^{\infty} \alpha_{2_{2n},m} \frac{k_{z2,2n,m}^{TM}}{q_{2_{2n},m}^{TM}} \oint_0^{2\pi} \left[ h_{2r+2}^{(z)}(q_{2r+2,s}^{TE}) \frac{\partial e_{2n}^{(z)}(q_{2_{2n},m}^{TM})}{\partial \varphi} d\varphi \right]_{\mu=\mu_2}.
\end{aligned}$$

#### 7.4.4 Equation 3 (magnetic field): projection with TM modes

Let us apply the condition of continuity of the tangential magnetic field 7.24 at the interface  $z=0$  between the two elliptical beam pipes of different cross section:

$$\begin{aligned}
\mathbf{H}_{1,t}^0 + \sum_{m=1}^{\infty} \sum_{n=0}^{\infty} \alpha_{1_{2n},m} \mathbf{h}_{2\mathbf{n}}^{(\mathbf{t})}(q_{1_{2n},m}^{TM}) + \sum_{m=1}^{\infty} \sum_{n=0}^{\infty} \beta_{1_{2n+2},m} \mathbf{h}_{2\mathbf{n}}^{(\mathbf{t})}(q_{1_{2n+2},m}^{TE}) = \\
\mathbf{H}_{2,t}^0 + \sum_{m=1}^{\infty} \sum_{n=0}^{\infty} \alpha_{2_{2n},m} \mathbf{h}_{2\mathbf{n}}^{(\mathbf{t})}(q_{2_{2n},m}^{TM}) + \sum_{m=1}^{\infty} \sum_{n=0}^{\infty} \beta_{2_{2n+2},m} \mathbf{h}_{2\mathbf{n}}^{(\mathbf{t})}(q_{2_{2n+2},m}^{TE}). \tag{7.44}
\end{aligned}$$

To obtain the third matching equation of the system we apply the Ritz-Galerking method to both sides of Eq. 7.44: we scalar multiply for the modal function of the first waveguide  $\mathbf{h}_{2\mathbf{r}}^{(\mathbf{t})}(q_{1_{2r},s}^{TM})$  and integrate in  $D_1$ :

$$\begin{aligned}
& \int_{D_1} \mathbf{H}_{1,t}^0 \cdot \mathbf{h}_{2\mathbf{r}}^{(\mathbf{t})}(q_{1_{2r},s}^{TM}) dS + \tag{7.45} \\
& \int_{D_1} \sum_{m=1}^{\infty} \sum_{n=0}^{\infty} \alpha_{1_{2n},m} \mathbf{h}_{2\mathbf{n}}^{(\mathbf{t})}(q_{1_{2n},m}^{TM}) \cdot \mathbf{h}_{2\mathbf{r}}^{(\mathbf{t})}(q_{1_{2r},s}^{TM}) : dS + \\
& \int_{D_1} \sum_{m=1}^{\infty} \sum_{n=0}^{\infty} \beta_{1_{2n+2},m} \mathbf{h}_{2\mathbf{n}+2}^{(\mathbf{t})}(q_{1_{2n+2},m}^{TE}) \cdot \mathbf{h}_{2\mathbf{r}}^{(\mathbf{t})}(q_{1_{2r},s}^{TM}) dS = \\
& \int_{D_2} \mathbf{H}_{2,t}^0 \cdot \mathbf{h}_{2\mathbf{r}}^{(\mathbf{t})}(q_{1_{2r},s}^{TM}) dS + \\
& \int_{D_2} \sum_{m=1}^{\infty} \sum_{n=0}^{\infty} \alpha_{2_{2n},m} \mathbf{h}_{2\mathbf{n}}^{(\mathbf{t})}(q_{2_{2n},m}^{TM}) \cdot \mathbf{h}_{2\mathbf{r}}^{(\mathbf{t})}(q_{1_{2r},s}^{TM}) dS + \\
& \int_{D_2} \sum_{m=1}^{\infty} \sum_{n=0}^{\infty} \beta_{2_{2n+2},m} \mathbf{h}_{2\mathbf{n}+2}^{(\mathbf{t})}(q_{2_{2n+2},m}^{TE}) \cdot \mathbf{h}_{2\mathbf{r}}^{(\mathbf{t})}(q_{1_{2r},s}^{TM}) dS
\end{aligned}$$

With some manipulations we obtain

$$\begin{aligned}
& \int_{D_1} \mathbf{H}_{1,t}^0 \cdot \mathbf{h}_{2\mathbf{r}}^{(t)} \left( q_{12r,s}^{TM} \right) dS - \tag{7.46} \\
& \left( \frac{F}{4} \right)^4 \int_{D_1} \sum_{m=1}^{\infty} \sum_{n=0}^{\infty} \frac{k_0^2}{q_{12n,m}^{TM} q_{12r,s}^{TM} Z_0} \alpha_{12n,m} \left[ \nabla_t e_{2n}^{(z)} \left( q_{12n,m}^{TM} \right) \right] \cdot \left[ \nabla_t e_{2r}^{(z)} \left( q_{12r,s}^{TM} \right) \right] dS + \\
& \left( \frac{F}{4} \right)^4 \int_{D_1} \sum_{m=1}^{\infty} \sum_{n=0}^{\infty} \frac{k_{z_1,2n+2,m}^{TE}}{q_{12n+2,m}^{TE}} \frac{k_0}{q_{12r,s}^{TM}} \beta_{12n+2,m} \left[ \nabla_t h_{2n+2}^{(z)} \left( q_{12n+2,m}^{TE} \right) \right] \cdot \left[ \hat{\mathbf{z}} \times \nabla_t e_{2r}^{(z)} \left( q_{12r,s}^{TM} \right) \right] dS = \\
& \int_{D_1} \mathbf{H}_{2,t}^0 \cdot \mathbf{h}_{2\mathbf{r}}^{(t)} \left( q_{12r,s}^{TM} \right) dS - \\
& \left( \frac{F}{4} \right)^4 \int_{D_1} \sum_{m=1}^{\infty} \sum_{n=0}^{\infty} \frac{k_0^2}{q_{12r,s}^{TM} q_{22n,m}^{TM} Z_0} \alpha_{22n,m} \left[ \nabla_t e_{2r}^{(z)} \left( q_{12r,s}^{TM} \right) \right] \cdot \left[ \nabla_t e_{2n}^{(z)} \left( q_{22n,m}^{TM} \right) \right] dS - \\
& \left( \frac{F}{4} \right)^4 \int_{D_1} \sum_{m=1}^{\infty} \sum_{n=0}^{\infty} \frac{k_{z_2,2n+2,m}^{TE}}{q_{22n+2,m}^{TE}} \frac{k_0}{q_{12r,s}^{TM}} \beta_{22n+2,m} \left[ \nabla_t h_{2n+2}^{(z)} \left( q_{22n+2,m}^{TE} \right) \right] \cdot \left[ \hat{\mathbf{z}} \times \nabla_t e_{2r}^{(z)} \left( q_{12r,s}^{TM} \right) \right] dS.
\end{aligned}$$

The third terms of the first and second members are zero because of the properties of electric and magnetic fields on the boundaries.

Let us consider the second term of the first member: the integral is always zero when  $q_{12n,m}^{TM} \neq q_{12r,s}^{TM}$ , that occurs when  $n \neq m$  or  $r \neq s$ . Otherwise the integral is equal to

$$\int_{D_1} \left[ \nabla_t e_{2r}^{(z)} \left( q_{12r,s}^{TM} \right) \right] \cdot \left[ \nabla_t e_{2r}^{(z)} \left( q_{12r,s}^{TM} \right) \right] dS = 2q_{12r,s}^{TM} \vartheta_{2r,s}, \tag{7.47}$$

where

$$\vartheta_{2r,s} = \int_{D_1} \left[ e_{2r}^{(z)} \left( q_{12r,s}^{TM} \right) \right]^2 (\cosh 2\mu - \cos 2\varphi) d\varphi d\mu. \tag{7.48}$$

If we consider Eq. 7.27, after some manipulations the second term of the second member becomes

$$\int_{D_1} \mathbf{h}_{2\mathbf{r}}^{(t)} \left( q_{12r,s}^{TM} \right) \cdot \mathbf{h}_{2\mathbf{n}}^{(t)} \left( q_{22n,m}^{TM} \right) dS = \tag{7.49}$$

$$-\left( \frac{F}{2} \right)^4 \frac{k_0^2}{q_{12r,s}^{TM} \left( q_{12r,s}^{TM} - q_{22n,m}^{TM} \right)} \oint_0^{2\pi} \left[ e_{2n}^{(z)} \left( q_{22n,m}^{TM} \right) \frac{\partial e_{2r}^{(z)} \left( q_{12r,s}^{TM} \right)}{\partial \mu} \right]_{\mu=\mu_1} d\varphi. \tag{7.50}$$

The third matching equation is given by

$$\int_{D_1} \mathbf{H}_{1,t}^0 \cdot \mathbf{h}_{2\mathbf{r}}^{(t)} \left( q_{12r,s}^{TM} \right) dS - \left( \frac{F}{2} \right)^4 \frac{2k_0^2}{Z_0} \alpha_{12r,s} \vartheta_{2r,s} = \tag{7.51}$$

$$\int_{D_1} \mathbf{H}_{2,t}^0 \cdot \mathbf{h}_{2\mathbf{r}}^{(t)} \left( q_{22r,s}^{TM} \right) dS - \\
\left( \frac{F}{2} \right)^4 \frac{k_0^2}{Z_0} \sum_{n=0}^{\infty} \sum_{m=1}^{\infty} \alpha_{22n,m} \frac{1}{q_{12r,s}^{TM} \left( q_{12r,s}^{TM} - q_{22n,m}^{TM} \right)} \oint_0^{2\pi} \left[ e_{2n}^{(z)} \left( q_{22n,m}^{TM} \right) \frac{\partial e_{2r}^{(z)} \left( q_{12r,s}^{TM} \right)}{\partial \varphi} \right]_{\mu=\mu_1} d\varphi.$$

### 7.4.5 Equation 4 (magnetic field): projection with TE modes

To obtain the forth matching equation of the system we apply the Ritz-Galerking method to both sides of Eq. 7.44: we scalar multiply for the modal function of the first waveguide  $\mathbf{h}_{2\mathbf{r}+2}^{(t)}(q_{1_{2\mathbf{r}+2,s}}^{TE})$  and integrate in  $D_1$ . We obtain the following equation:

$$\begin{aligned}
& \int_{D_1} \mathbf{H}_{1,t}^0 \cdot \mathbf{h}_{2\mathbf{r}+2}^{(t)}(q_{1_{2\mathbf{r}+2,s}}^{TE}) dS + \\
& \int_{D_1} \sum_{m=1}^{\infty} \sum_{n=0}^{\infty} \alpha_{1_{2n,m}} \mathbf{h}_{2\mathbf{n}}^{(t)}(q_{1_{2n,m}}^{TM}) \cdot \mathbf{h}_{2\mathbf{r}+2}^{(t)}(q_{1_{2\mathbf{r}+2,s}}^{TE}) dS + \\
& \int_{D_1} \sum_{m=1}^{\infty} \sum_{n=0}^{\infty} \beta_{1_{2n+2,m}} \mathbf{h}_{2\mathbf{n}+2}^{(t)}(q_{1_{2n+2,m}}^{TE}) \cdot \mathbf{h}_{2\mathbf{r}+2}^{(t)}(q_{1_{2\mathbf{r}+2,s}}^{TE}) dS = \\
& \int_{D_1} \mathbf{H}_{2,t}^0 \cdot \mathbf{h}_{2\mathbf{r}+2}^{(t)}(q_{1_{2\mathbf{r}+2,s}}^{TE}) dS + \\
& \int_{D_1} \sum_{m=1}^{\infty} \sum_{n=0}^{\infty} \alpha_{2_{2n,m}} \mathbf{h}_{2\mathbf{n}}^{(t)}(q_{2_{2n,m}}^{TM}) \cdot \mathbf{h}_{2\mathbf{r}+2}^{(t)}(q_{1_{2\mathbf{r}+2,s}}^{TE}) dS + \\
& \int_{D_1} \sum_{m=1}^{\infty} \sum_{n=0}^{\infty} \beta_{2_{2n+2,m}} \mathbf{h}_{2\mathbf{n}+2}^{(t)}(q_{2_{2n+2,m}}^{TE}) \cdot \mathbf{h}_{2\mathbf{r}+2}^{(t)}(q_{1_{2\mathbf{r}+2,s}}^{TE}) dS.
\end{aligned} \tag{7.52}$$

Let us consider the identity 7.29: the second term of the first member is zero, being zero the electric field on the boundary. The integral of the third term of the first member is zero when  $q_{1_{2n+2,m}}^{TE} \neq q_{1_{2\mathbf{r}+2,s}}^{TE}$ , that occurs when  $n \neq m$  or  $r \neq s$ . Otherwise the integral becomes

$$\int_{D_1} \left[ \nabla_t h_{2n+2}^{(z)}(q_{1_{2n+2,m}}^{TE}) \right] \cdot \left[ \nabla_t h_{2\mathbf{r}+2}^{(z)}(q_{1_{2\mathbf{r}+2,s}}^{TE}) \right] dS = 2q_{1_{2\mathbf{r}+2,s}}^{TE} \rho_{2\mathbf{r}+2,s}, \tag{7.53}$$

where

$$\rho_{2\mathbf{r}+2,s} = \int_{D_1} \left[ h_{2\mathbf{r}+2}^{(z)}(q_{1_{2\mathbf{r}+2,s}}^{TE}) \right]^2 (\cosh 2\mu - \cos 2\varphi) d\varphi d\mu. \tag{7.54}$$

If we apply the identity 7.29, the second term of the second member, after some manipulation, becomes

$$\begin{aligned}
& \int_{D_1} \left[ \hat{\mathbf{z}} \times \nabla_t e_{2n}^{(z)}(q_{2_{2n,m}}^{TM}) \right] \cdot \left[ \nabla_t h_{2\mathbf{r}+2}^{(z)}(q_{1_{2\mathbf{r}+2,s}}^{TE}) \right] dS = \\
& \int_0^{2\pi} \left[ e_{2n}^{(z)}(q_{2_{2n,m}}^{TM}) \frac{\partial h_{2\mathbf{r}+2}^{(z)}(q_{1_{2\mathbf{r}+2,s}}^{TE})}{\partial \varphi} \right]_{\mu=\mu_1} d\varphi.
\end{aligned} \tag{7.55}$$

Similarly, applying the identity 7.27, the third term of the second member, becomes

$$\int_{D_1} \left[ \nabla_t h_{2n+2}^{(z)} \left( q_{22n+2,m}^{TE} \right) \right] \cdot \left[ \nabla_t h_{2r+2}^{(z)} \left( q_{12r+2,s}^{TE} \right) \right] dS = \quad (7.56)$$

$$- \frac{1}{q_{22n+2,m}^{TE} - q_{12r+2,s}^{TE}} \oint_0^{2\pi} \left[ q_{12r+2,s}^{TE} h_{2r+2}^{(z)} \left( q_{12r+2,s}^{TE} \right) \frac{\partial h_{2n+2}^{(z)} \left( q_{22n+2,m}^{TE} \right)}{\partial \varphi} \right]_{\mu=\mu_1} d\varphi.$$

Finally, the fourth matching equation can be written as follow

$$\int_{D_1} \mathbf{H}_{1,t}^0 \cdot \mathbf{h}_{2r+2}^{(t)} \left( q_{12r+2,s}^{TE} \right) dS - \left( \frac{F}{2} \right)^4 \left( \frac{k_{z1,2r+2,s}^{TE}}{q_{12r+2,s}^{TE}} \right)^2 2\beta_{12r+2,s} q_{12r+2,s}^{TE} \vartheta_{2r+2,s} = \quad (7.57)$$

$$\int_{D_1} \mathbf{H}_{2,t}^0 \cdot \mathbf{h}_{2r+2}^{(t)} \left( q_{12r+2,s}^{TE} \right) dS +$$

$$\left( \frac{F}{2} \right)^4 \sum_{n=0}^{\infty} \sum_{m=0}^{\infty} \frac{k_0 k_{z1,2r+2,s}^{TE}}{q_{12r+2,s}^{TE} q_{22n,m}^{TM} Z_0} \alpha_{22n,m} \oint_0^{2\pi} \left[ e_{2n}^{(z)} \left( q_{22n,m}^{TM} \right) \frac{\partial h_{2r+2}^{(z)} \left( q_{12r+2,s}^{TE} \right)}{\partial \varphi} \right]_{\mu=\mu_1} d\varphi -$$

$$\left( \frac{F}{2} \right)^4 \sum_{n=0}^{\infty} \sum_{m=1}^{\infty} \frac{k_{z2,2n+2,m}^{TE} k_{z1,2r+2,s}^{TE} \beta_{22n+2,m}}{q_{22n+2,m}^{TE} \left( q_{22n+2,m}^{TE} - q_{12r+2,s}^{TE} \right)} \oint_0^{2\pi} \left[ h_{2r+2}^{(z)} \left( q_{12r+2,s}^{TE} \right) \frac{\partial h_{2n+2}^{(z)} \left( q_{22n+2,m}^{TE} \right)}{\partial \varphi} \right]_{\mu=\mu_1} d\varphi.$$

## 7.5 Known coefficients of the system

### 7.5.1 Equation 1 (electric field)

Let us calculate the known terms of Eq. 7.25: we have to scalar multiply both members of the equation for the modal function of second waveguide  $\mathbf{e}_{2r}^{(t)} \left( q_{22r,s}^{TM} \right)$  and integrate the two members in  $D_1$  and  $D_2$ , respectively. After some manipulations, the known term of the first matching equation is given by

$$\int_{D_1} \mathbf{E}_{1,t}^0 \cdot \mathbf{e}_{2r}^{(t)} \left( q_{22r,s}^{TM} \right) dS - \int_{D_2} \mathbf{E}_{2,t}^0 \cdot \mathbf{e}_{2r}^{(t)} \left( q_{22r,s}^{TM} \right) dS = \quad (7.58)$$

$$= -2\pi G \left( \frac{F}{2} \right)^4 \frac{k_z^{TM} k_{z2,2r,s}^{TM} C e_{2r} \left( q_{22r,s}^{TM}, \mu_1 \right)}{q^{TM} \left( q^{TM} + q_{22r,s}^{TM} \right)} \sum_{n=0}^{\infty} \frac{A_0^{(2n)}}{p_{2n}} \frac{w_{2n}}{C e_{2n} \left( -q^{TM}, \mu_1 \right)} F(2n, 2r, s)$$

where  $w_{2n}$  is a wronskian, given by

$$w_{2n} = F e k_{2n} \left( -q^{TM}, \mu_1 \right) C e'_{2n} \left( -q^{TM}, \mu_1 \right) - C e_{2n} \left( -q^{TM}, \mu_1 \right) F e k'_{2n} \left( -q^{TM}, \mu_1 \right) \quad (7.59)$$

and

$$F(2n, 2r, s) = \int_0^{2\pi} c e_{2n} \left( -q^{TM}, \varphi \right) c e_{2r} \left( q_{22r,s}^{TM}, \varphi \right) d\varphi. \quad (7.60)$$

After some manipulations we can also write a simpler form for the known term of the first matching equation:

$$\begin{aligned} & \int_{D_1} \mathbf{E}_{1,t}^0 \cdot \mathbf{e}_{2r}^{(t)}(q_{2r,s}^{TM}) dS - \int_{D_2} \mathbf{E}_{2,t}^0 \cdot \mathbf{e}_{2r}^{(t)}(q_{2r,s}^{TM}) dS = \quad (7.61) \\ & = -2G \left(\frac{F}{2}\right)^4 \frac{k_z^{TM} k_{z2,2r,s}^{TM} C e_{2r}(q_{2r,s}^{TM}, \mu_1)}{q^{TM} (q^{TM} + q_{2r,s}^{TM})} \sum_{n=0}^{\infty} \frac{(-1)^n c e_{2n}(q^{TM}, 0) C e_{2n}(-q^{TM}, 0)}{C e_{2n}(-q^{TM}, \mu_1)} F(2n, 2r, s) \end{aligned}$$

### 7.5.2 Equation 2 (electric field)

To obtain an explicit expression for the known terms of the second matching equation, we have to scalar multiply both member of Eq. 7.25 for the modal function of second waveguide  $\widehat{\mathbf{z}} \times \nabla_t h_{2r+2}^{(z)}(q_{2r,s}^{TE})$  and integrate the two members in  $D_1$  end  $D_2$ , respectively. After some manipulations, we obtain that the known term of the second matching equation is zero.

### 7.5.3 Equation 3 (magnetic field)

To obtain an explicit formula for the known terms of the third matching equation, we had to scalar multiplied both member of Eq. 7.44 for the modal function of first waveguide  $\mathbf{h}_{2r}^{(t)}(q_{12r,s}^{TM})$ , and integrate both in  $D_1$ . After some manipulations, we obtain that the known term of the third matching equation is given by:

$$\begin{aligned} & \int_{D_1} \mathbf{H}_{1,t}^0 \cdot \mathbf{h}_{2r}^{(t)}(q_{12r,s}^{TM}) dS - \int_{D_1} \mathbf{H}_{2,t}^0 \cdot \mathbf{h}_{2r}^{(t)}(q_{12r,s}^{TM}) dS = \quad (7.62) \\ & = -2\pi G \left(\frac{F}{2}\right)^4 \left(\frac{k_0^2}{Z_0}\right) \frac{C e'_{2r}(q_{12r,s}^{TM}, \mu_1)}{q_{12r,s}^{TM} (q^{TM} + q_{12r,s}^{TM})} \sum_{n=0}^{\infty} \frac{A_0^{(2n)}}{p_{2n}} \frac{g_{2n}}{C e_{2n}(-q^{TM}, \mu_2)} V(2n, 2r, s) \end{aligned}$$

where

$$g_{2n} = F e k_{2n}(-q^{TM}, \mu_1) C e_{2n}(-q^{TM}, \mu_2) - F e k_{2n}(-q^{TM}, \mu_2) C e_{2n}(-q^{TM}, \mu_1) \quad (7.63)$$

and  $V(2n, 2r, s)$  is given by the following integral

$$V(2n, 2r, s) = \int_0^{2\pi} c e_{2n}(-q^{TM}, \varphi) c e_{2r}(q_{12r,s}^{TM}, \varphi) d\varphi. \quad (7.64)$$

### 7.5.4 Equation 4 (magnetic field)

To obtain an explicit formula for the known terms of the fourth matching equation, we have to scalar multiply both member of Eq. 7.39 for the modal function of first waveguide  $\mathbf{h}_{2r+2}^{(t)}(q_{1_{2r+2},s}^{TE})$  and integrate both the two members in  $D_1$ . After some manipulations, we obtain that the known term of the forth matching equation is given by:

$$\begin{aligned} & \int_{D_1} \mathbf{H}_{1,t}^0 \cdot \mathbf{h}_{2r+2}^{(t)}(q_{1_{2r+2},s}^{TE}) dS - \int_{D_1} \mathbf{H}_{2,t}^0 \cdot \mathbf{h}_{2r+2}^{(t)}(q_{1_{2r+2},s}^{TE}) dS = \quad (7.65) \\ & = 2\pi G \left(\frac{F}{2}\right)^4 \frac{k_0 k_{z_{1,2r+2},s}^{TE}}{Z_0 q^{TM} q_{1_{2r+2},s}^{TE}} S e_{2r+2}(q_{1_{2r+2},s}^{TE}, \mu_1) \sum_{n=0}^{\infty} \frac{A_0^{(2n)}}{p_{2n}} \frac{g_{2n}}{C e_{2n}(-q^{TM}, \mu_2)} W(2r+2, s, 2n) \end{aligned}$$

where the integral  $W(2r+2, s, 2n)$  is given by

$$W(2r+2, s, 2n) = \int_0^{2\pi} c e_{2n}(-q^{TM}, \varphi) s e'_{2r+2}(q_{1_{2r+2},s}^{TE}, \varphi) d\varphi. \quad (7.66)$$

### 7.5.5 Mode Matching system summary

#### Equation I

$$2G \frac{k_z^{TM} C e_{2r}(q_{2r,s}^{TM}, \mu_1)}{q^{TM} (q^{TM} + q_{2r,s}^{TM})} \sum_{n=0}^{\infty} \left\{ (-1)^n \frac{c e_{2n}(q^{TM}, 0) C e_{2n}(-q^{TM}, 0)}{C e_{2n}(-q^{TM}, \mu_1)} F(2n, 2r, s) \right\} + \quad (7.67)$$

$$\begin{aligned} & \sum_{n=0}^{\infty} \sum_{m=1}^{\infty} \alpha_{1_{2n},m} \frac{k_{z_{1,2n},m}^{TM}}{(q_{1_{2n},m}^{TM} - q_{2r,s}^{TM}) q_{1_{2n},m}^{TM}} \int_0^{2\pi} e_{2r}^{(z)}(q_{2r,s}^{TM}) \frac{\partial e_{2n}^{(z)}(q_{1_{2n},m}^{TM})}{\partial \mu} \Big|_{\mu=\mu_1} d\varphi + \\ & k_0 Z_0 \sum_{n=0}^{\infty} \sum_{m=1}^{\infty} \beta_{1_{2n+2},m} \frac{1}{q_{1_{2n+2},m}^{TE} q_{2r,s}^{TM}} \int_0^{2\pi} h_{2n+2}^{(z)}(q_{1_{2n+2},m}^{TE}) \frac{\partial e_{2r}^{(z)}(q_{2r,s}^{TM})}{\partial \varphi} \Big|_{\mu=\mu_1} d\varphi \\ & = 2 \alpha_{2r,s} \frac{k_{z_{2,2r},s}^{TM}}{q_{2r,s}^{TM}} \sigma_{2r,s} \end{aligned}$$

#### Equation II

$$\begin{aligned} & \sum_{m=1}^{\infty} \sum_{n=0}^{\infty} \beta_{1_{2n+2},m} \frac{1}{(q_{1_{n+2},m}^{TE} - q_{2r+2,s}^{TE})} \int_0^{2\pi} h_{2n+2}^{(z)}(q_{1_{2n+2},m}^{TE}) \frac{\partial h_{2r+2}^{(z)}(q_{2r+2,s}^{TE})}{\partial \mu} \Big|_{\mu=\mu_1} d\varphi \quad (7.68) \\ & = 2\beta_{2r+2,s} \theta_{2r+2,s} \end{aligned}$$

**Equation III**

$$\begin{aligned}
& -2\pi G \frac{C e'_{2r} \left( q_{12r,s}^{TM}, \mu_1 \right)}{q_{12r,s}^{TM} \left( q_{12r,s}^{TM} + q_{12r,s}^{TM} \right)} \sum_{n=0}^{\infty} \left\{ \frac{A_0^{(2n)}}{p_{2n}} \frac{g_{2n}}{C e_{2n} \left( -q^{TM}, \mu_2 \right)} V \left( 2n, 2r, s \right) \right\} - \quad (7.69) \\
& \sum_{n=0}^{\infty} \sum_{m=1}^{\infty} \alpha_{22n,m} \frac{1}{q_{12r,s}^{TM} \left( q_{12r,s}^{TM} - q_{22n,m}^{TM} \right)} \oint_0^{2\pi} e_{2n}^{(z)} \left( q_{22n,m}^{TM} \right) \frac{\partial e_{2r}^{(z)} \left( q_{12r,s}^{TM} \right)}{\partial \mu} \Big|_{\mu=\mu_1} d\varphi \\
& = 2\alpha_{12r,s} \vartheta_{2r,s}
\end{aligned}$$

**Equation IV**

$$\begin{aligned}
& 2G \frac{k_0}{Z_0} \frac{S e_{2r+2} \left( q_{12r+2,s}^{TE}, \mu_1 \right)}{q_{12r+2,s}^{TE} q_{12r+2,s}^{TE}} \sum_{n=0}^{\infty} \left\{ \frac{A_0^{(2n)}}{p_{2n}} \frac{g_{2n}}{C e_{2n} \left( -q^{TM}, \mu_2 \right)} W \left( 2n, 2r+2, s \right) \right\} - \quad (7.70) \\
& \frac{k_0}{Z_0} \sum_{m=1}^{\infty} \sum_{n=0}^{\infty} \alpha_{22n,m} \frac{1}{q_{12r+2,s}^{TE} q_{22n,m}^{TM}} \oint_0^{2\pi} e_{2n}^{(z)} \left( q_{22n,m}^{TM} \right) \frac{\partial h_{2r+2}^{(z)} \left( q_{12r+2,s}^{TE} \right)}{\partial \varphi} \Big|_{\mu=\mu_1} d\varphi + \\
& \sum_{n=0}^{\infty} \sum_{m=1}^{\infty} \beta_{22n+2,m} \frac{k_{z_2,2n+2,m}^{TE}}{q_{22n+2,m}^{TE} \left( q_{22n+2,m}^{TE} - q_{12r+2,s}^{TE} \right)} \oint_0^{2\pi} h_{2r+2}^{(z)} \left( q_{12r+2,s}^{TE} \right) \frac{\partial h_{2n+2}^{(z)} \left( q_{12n+2,m}^{TE} \right)}{\partial \mu} \Big|_{\mu=\mu_1} d\varphi \\
& = 2 \beta_{12r+2,s} \frac{k_{z_1,2r+2,s}^{TE}}{q_{12r+2,s}^{TE}} \rho_{2r+2,s}
\end{aligned}$$

The matching system could be summarized as follow:

$$\begin{cases} F + T_1 \alpha_1 + S_1 \beta_1 = D_1 \alpha_2 \\ S_2 \beta_1 = D_2 \beta_2 \\ V + D_3 \alpha_1 = P_3 \alpha_2 \\ W + D_4 \beta_1 = P_4 \alpha_2 + Q_4 \beta_2 \end{cases} \quad (7.71)$$

where

- $T_1, S_1, S_2, P_3, P_4, Q_4$  are tensors of dimension  $(n \times m) \times (r \times s)$ ;
- $F, W, V$ , are known vectors of dimension  $(r \times s) \times 1$ ;
- $D_1, D_2, D_3, D_4$ , are diagonal matrices of dimension  $(r \times s) \times (r \times s)$ ;
- $\alpha_1, \alpha_2, \beta_1, \beta_2$ , are unknown vectors of dimension  $(n \times m) \times 1$ .

## 7.6 Longitudinal coupling impedance calculation

Solving the system of four equations we obtain the four modal amplitudes  $\alpha_{12n,m}$ ,  $\alpha_{22n,m}$ ,  $\beta_{12n+2,m}$ ,  $\beta_{22n+2,m}$  of the electromagnetic field scattered by the step discontinuity. Once obtained the amplitudes, we can calculate, in the center of the elliptic tube, the radiated field in the two regions as

$$E_z^{rad}(\omega; z) = \begin{cases} \sum_{n=0}^{\infty} \sum_{m=1}^{\infty} \alpha_{12n,m} c e_{2n}\left(\frac{\pi}{2}, q_{12n,m}^{TM}\right) C e_{2n}(0, q_{12n,m}^{TM}) \exp\left[j\left(\omega t + z\sqrt{k_0^2 - k_{12n,m}^2}\right)\right] \\ \sum_{n=0}^{\infty} \sum_{m=1}^{\infty} a_{22n,m} c e_{2n}\left(\frac{\pi}{2}, q_{22n,m}^{TM}\right) C e_{2n}(0, q_{22n,m}^{TM}) \exp\left[j\left(\omega t - z\sqrt{k_0^2 - k_{22n,m}^2}\right)\right] \end{cases} \quad (7.72)$$

To calculate the longitudinal coupling impedance, we can substitute the above identity in Eq. 7.13. We obtain (dependency from the variables  $\varphi$  and  $\mu$  has been omitted)

$$Z_L(k) = -\frac{1}{q} \int_{-\infty}^0 \sum_{n=0}^{\infty} \sum_{m=1}^{\infty} \alpha_{12n,m} c e_{2n}\left(q_{12n,m}^{TM}\right) C e_{2n}\left(q_{12n,m}^{TM}\right) \exp\left[jz\left(\frac{k_0}{\beta} + \sqrt{k_0^2 - k_{12n,m}^2}\right)\right] dz - \quad (7.73)$$

$$+\frac{1}{q} \int_0^{\infty} \sum_{n=0}^{\infty} \sum_{m=1}^{\infty} a_{22n,m} c e_{2n}\left(q_{22n,m}^{TM}\right) C e_{2n}\left(q_{22n,m}^{TM}\right) \exp\left[jz\left(\frac{k_0}{\beta} - \sqrt{k_0^2 - k_{22n,m}^2}\right)\right] dz,$$

where  $q$  is the particle charge. Let us suppose that propagation constant presents a small negative imaginary part  $k_z = \beta - j\alpha$ . With some manipulations, the first integral of the coupling impedance equation becomes:

$$\lim_{\alpha \rightarrow 0} \int_{-\infty}^0 \sum_{n=0}^{\infty} \sum_{m=1}^{\infty} a_{12n,m} c e_{2n}\left(q_{12n,m}^{TM}\right) C e_{2n}\left(q_{12n,m}^{TM}\right) \exp\left[jz\left(\frac{k_0}{\beta} + \sqrt{k_0^2 - k_{12n,m}^2} - j\alpha\right)\right] dz = \quad (7.74)$$

$$\sum_{n=0}^{\infty} \sum_{m=1}^{\infty} a_{12n,m} \frac{c e_{2n}\left(q_{12n,m}^{TM}\right) C e_{2n}\left(q_{12n,m}^{TM}\right)}{j\left(\frac{k_0}{\beta} + \sqrt{k_0^2 - k_{12n,m}^2}\right)}.$$

Similarly, the second integral becomes

$$\lim_{\alpha \rightarrow 0} \int_0^{\infty} \sum_{n=0}^{\infty} \sum_{m=1}^{\infty} a_{22n,m} c e_{2n}\left(q_{22n,m}^{TM}\right) C e_{2n}\left(q_{22n,m}^{TM}\right) \exp\left[jz\left(\frac{k_0}{\beta} - \sqrt{k_0^2 - k_{22n,m}^2} + j\alpha\right)\right] dz = \quad (7.75)$$

$$\sum_{n=0}^{\infty} \sum_{m=1}^{\infty} a_{22n,m} \frac{c e_{2n}\left(q_{22n,m}^{TM}\right) C e_{2n}\left(q_{22n,m}^{TM}\right)}{j\left(\frac{k_0}{\beta} - \sqrt{k_0^2 - k_{22n,m}^2}\right)}.$$

Finally we obtain a simple expression that allows to calculate the longitudinal beam coupling impedance of a step transition between two co-focal elliptical waveguides:

$$Z_L(k) = - \sum_{n=0}^{\infty} \sum_{m=1}^{\infty} \alpha_{1_{2n,m}} \frac{ce_{2n}\left(\frac{\pi}{2}, q_{1_{2n,m}}^{TM}\right) Ce_{2n}\left(0, q_{1_{2n,m}}^{TM}\right) \left[\frac{k_0}{\beta} - \sqrt{(k_0^2 - k_{1_{2n,m}}^2)}\right]}{jq \left[\left(\frac{k_0}{\beta}\right)^2 - k_0^2 + k_{1_{2n,m}}^2\right]} \quad (7.76)$$

$$- \sum_{n=0}^{\infty} \sum_{m=1}^{\infty} \alpha_{2_{2n,m}} \frac{ce_{2n}\left(\frac{\pi}{2}, q_{2_{2n,m}}^{TM}\right) Ce_{2n}\left(0, q_{2_{2n,m}}^{TM}\right) \left[\frac{k_0}{\beta} + \sqrt{(k_0^2 - k_{2_{2n,m}}^2)}\right]}{jq \left[\left(\frac{k_0}{\beta}\right)^2 - k_0^2 + k_{2_{2n,m}}^2\right]}.$$

Equation 7.76 allows a fast calculation of the longitudinal beam coupling impedance, due to the rapidly convergence Mathieu functions.

## Conclusions

In this chapter we determined an analytical formula for the longitudinal beam coupling impedance of a step transition between two beam chambers of elliptical cross-section. This type of problem, involving two separate regions, was addressed with the *mode matching* method. The radiated field from the discontinuity has been expressed as the product of a modal function for a modal coefficient. Imposing the condition on continuity of the tangential electric and magnetic fields at the interface, a set of linear equations for the unknown modal coefficients is obtained. The problem reduces in determining a set of modal amplitudes associated with the field expansions in the two regions, where the novel field expansion calculated in Chapter 6 represents the known coefficients of the system. The amplitudes of the radiated electric field in the two regions are calculated solving the four equations system, and the longitudinal impedance is calculated with the Fourier transform of the field itself. The formula for the longitudinal beam coupling impedance of the elliptical step transition is provided. Nevertheless, further numerical studies on matrix truncation are in progress, in order to provide an efficient method of calculation of the impedance that can be used in addition or in substitution to electromagnetic simulations.

# Conclusions

In this thesis work we developed the longitudinal and transverse beam coupling impedance model of the CERN Proton Synchrotron (PS), in the framework of the LHC Injector Upgrade (LIU) project. The knowledge of the coupling impedance models, such as the impedance of some critical elements, allows a better understanding of the instability threshold of the machine, and helps predicting the effects of the current increase planned for the upgrade program. The two coupling impedance models have been determined with beam based measurements and simulations of machine devices. Eleven injection and extraction kicker magnets with different geometries, several types of RF cavities and mechanical components of the chamber (vacuum pumps, valves, flanges, bellows) have been examined. Finally, the impedances of the devices have been summed together, obtaining the total impedance (longitudinal and transverse) as a function of frequency, representing the impedance model (longitudinal and transverse) of the machine. For the longitudinal case, beam based measurements of the incoherent quadrupolar synchrotron frequency shift as a function of beam intensity have been carried out at the beginning of 2012. The longitudinal impedance of  $Z(p)/p = 18.4 \pm 2.2 \Omega$  is in agreement with measurements performed on the machine about 10 years ago. An analysis of several contributors to the impedance resulted in excellent agreement with the measurement, explaining almost the 90% of the measured longitudinal impedance. This accurate model developed for the longitudinal broadband impedance can be used to for beam dynamics simulations of the machine. In order to determine the transverse impedance model, beam based measurements of the tune shift as a function of beam intensity have been carried out at the beginning of 2012 and in 2014, after the machine shut down. The measured vertical impedance at zero chromaticity is  $8.2 \text{ M}\Omega/\text{m}$  at injection energy and  $2.2 \text{ M}\Omega/\text{m}$  at extraction energy. The difference in the two measurements can be explained by the effect of the indirect space charge. A scan of the imaginary part of the vertical impedance with chromaticity has been performed, revealing an increasing trend for all the sets of measurements. This result could suggest the presence of undefined machine elements introducing a low frequency resonance not detected so far. The impedance model obtained with simulation is in fairly good agreement with the measured values, and justifies, for example, about the

65% of the vertical impedance obtained with tune shift measurements at the energy of 2 GeV. Measurements of the PS beam spectrum and shape have been performed with RF instrumentation, both in the single and in the multi-bunch case. This campaign allowed to obtain a reference for impedance resonance modes of the machine devices, considered potentially dangerous for the instabilities: resonances falling inside the beam spectrum can be a source of heating and power losses and, therefore, need to be identified.

Beam coupling impedance studies, that included simulation, RF measurements and theoretical calculations, have been performed for three new devices, before their installation in the machine in 2013-2014. This studies helped to understand the contribution of these elements to the longitudinal and transverse impedance budget. The impedance studies for the dummy septum, a radiation protection passive device installed in section 16 of the PS, followed-up all mechanical design stages. Due to impedance and heating related issues revealed by the study, the insertion of sliding contacts for high order modes damping has been proposed and accepted in the final design of the installed device. Bench measurements took place in order to test the performance of the sliding contacts before installation. The dummy septum is currently working in the machine under nominal operation beam conditions without impedance related issues. Impedance studies have been carried out for the new longitudinal damper loaded with Finemet®, comparing simulations and bench measurements. The device was designed to reduce the impact of coupled bunch instability in the PS, and it is currently installed in the straight section 01. As last, the impedance of the new PS beam position monitor has been studied. The device, that was designed as a stripline pickup, is currently installed in straight section 72 and has been used for the tune shift measurements described in Chapter 3.

In the second part of this thesis work, a novel formulation of the field produced by a  $\delta$  beam distribution traveling inside a tube of elliptical cross section, has been determined. The solution, in the form of Mathieu and Bessel functions, is rapidly convergent and has been obtained separating the contribution of the Green function generated in free space (primary field) and the field scattered by the charge on the elliptical boundary (indirect field). The novel expansion of the longitudinal electric field is expressed in elliptical coordinates and in separate functions of the elliptic variables. The new expansion of the Green function in elliptical coordinates has been compared with the formula in circular coordinates, showing very good agreement for different combinations of parameters and summation orders. These new results allow a better understanding of the electromagnetic propagation and scattering phenomena that occur in elliptical beam chambers while crossed by a particle field.

In this frame, considering the high number of step transitions between circular and elliptical waveguide currently present in the PS, a novel analytical formula for the evaluation of the longitudinal beam coupling impedance of a step transition between two semi-infinite elliptical waveguides, by means of the mode matching theory, has also been developed.

---

The diffracted field from the junction has been expressed as the product of a modal function for a modal coefficient; imposing the condition on continuity of the tangential electric and magnetic fields at the interface, we obtained a set of linear equations for the unknown modal coefficients. Solving the matching system, where the primary field expressed with the new expansion represents the known term, allows to calculate the longitudinal beam coupling impedance of the step transition. The analytic formula to compute the longitudinal beam coupling impedance of the step transition is provided. Further numerical studies on matrix truncation are in progress, in order to provide an efficient method of calculation of the impedance that can be used in addition or in substitution to electromagnetic simulations.



# Appendix A

## Simil-Green formula

The starting formula is the following:

$$\nabla_t \cdot (\hat{z} \times (U_r \nabla_t V_s)) \quad (\text{A.1})$$

where we apply the rule of mixed product  $\nabla \cdot (A \times B) = B \cdot \nabla \times A - A \cdot \nabla \times B$ .

Being  $\nabla_t \times \hat{z} = 0$ , we obtain:

$$\nabla_t \cdot (\hat{z} \times (U_r \nabla_t V_s)) = U_r \nabla_t V_s \cdot \nabla_t \times \hat{z} - \hat{z} \cdot \nabla_t \times U_r \nabla_t V_s = -\hat{z} \cdot \nabla_t \times U_r \nabla_t V_s. \quad (\text{A.2})$$

We consider now the following identity:

$$\nabla \times (\Phi A) = \nabla \Phi \times A + \Phi \nabla \times A. \quad (\text{A.3})$$

We have that:

$$\nabla_t \cdot (\hat{z} \times (U_r \nabla_t V_s)) = -\hat{z} \cdot \nabla_t \times U_r \nabla_t V_s = -\hat{z} \cdot [\nabla_t U_r \times \nabla_t V_s + U_r \nabla_t \times \nabla_t V_s] = -\hat{z} \cdot (\nabla_t U_r \times \nabla_t V_s).$$

That leads to

$$\int_s \nabla_t \cdot (\hat{z} \times (U_r \nabla_t V_s)) dS = - \int_s \hat{z} \cdot \nabla_t \times U_r \nabla_t V_s dS = - \int_s \hat{z} \cdot (\nabla_t U_r \times \nabla_t V_s) dS \quad (\text{A.4})$$

If we consider the following rule  $\nabla \cdot (\Phi A) = \Phi \nabla \cdot A + \nabla \Phi \cdot A$  we can verify the following identity:

$\nabla_t \cdot [V_s (\hat{z} \times \nabla_t U_r)] = V_s \nabla_t \cdot (\hat{z} \times \nabla_t U_r) + \nabla_t V_s \cdot (\hat{z} \times \nabla_t U_r)$ . Being the first term of the second member zero:

$$\nabla_t \cdot [V_s (\hat{z} \times \nabla_t U_r)] = \nabla_t V_s \cdot (\hat{z} \times \nabla_t U_r) = \hat{z} \cdot \nabla_t U_r \times \nabla_t V_s,$$

then

$$\int_s \nabla_t \cdot (\hat{z} \times (U_r \nabla_t V_s)) dS = - \int_s \hat{z} \cdot (\nabla_t U_r \times \nabla_t V_s) dS = - \int_s \nabla_t V_s \cdot (\hat{z} \times \nabla_t U_r) dS^*$$

We apply the diverge theorem in two dimensions at the integer at the first member:

$$\int_s \nabla_t \cdot (\hat{z} \times (U_r \nabla_t V_s)) dS = \oint_l \hat{n} \cdot [\hat{z} \times (U_r \nabla_t V_s)] dl = \oint_l U_r \nabla_t V_s \cdot (\hat{n} \times \hat{z}) dl = \oint_l U_r \nabla_t V_s d\vec{l} = \oint_l U_r \frac{\partial V_s}{\partial t} dl$$

We obtain that:

$$\int_s \hat{z} \cdot (\nabla_t U_r \times \nabla_t V_s) dS = - \oint_l U_r \frac{\partial V_s}{\partial t} dl$$

Solving the integer by parts, and being  $U_r V_s = 0$  between 0 and  $2\pi$ , we obtain:

$$\oint_l U_r \frac{\partial V_s}{\partial t} dl = - \oint V_s \frac{\partial U_r}{\partial t} dl$$

To conclude we demonstrated the following identity:

$$\int_s \hat{z} \cdot (\nabla_t U_r \times \nabla_t V_s) dS = - \oint_l U_r \frac{\partial V_s}{\partial t} dl = \oint V_s \frac{\partial U_r}{\partial t} dl. \quad (\text{A.5})$$

## Appendix B

# Primary field components

### Direct field components

$$e_{2n}^{(z)}(-q^{TM}) = ce_{2n}(-q^{TM}, \phi) Fek_{2n}(-q^{TM}, \mu) \quad (\text{B.1})$$

$$h_{2n}^{(z)}(-q^{TM}) = 0 \quad (\text{B.2})$$

$$\mathbf{e}_{2n}^{(t)}(-q^{TM}) = \frac{jk_z^{TM} F^2}{-4q^{TM}} \nabla_t e_{2n}^{(z)}(-q^{TM}) \quad (\text{B.3})$$

$$\mathbf{h}_{2n}^{(t)}(-q^{TM}) = -\frac{jk_0 F^2}{-4q^{TM}} \hat{\mathbf{z}} \times \nabla_t e_{2n}^{(z)}(-q^{TM}) \quad (\text{B.4})$$

### Indirect field components, waveguide I $z < 0$

$$e_{12n}^{(z)}(-q^{TM}) = -\frac{ce_{2n}(-q^{TM}, \phi) Ce_{2n}(-q^{TM}, \mu)}{Ce_{2n}(-q^{TM}, \mu_1)} Fek_{2n}(-q^{TM}, \mu_1) \quad (\text{B.5})$$

$$h_{12n}^{(z)}(-q^{TM}) = 0 \quad (\text{B.6})$$

$$\mathbf{e}_{12n}^{(t)}(-q^{TM}) = \frac{jk_z^{TM} F^2}{-4q^{TM}} \nabla_t e_{12n}^{(z)}(-q^{TM}) \quad (\text{B.7})$$

$$\mathbf{h}_{12n}^{(t)}(-q^{TM}) = -\frac{jk_0 F^2}{-4q^{TM}} \hat{\mathbf{z}} \times \nabla_t e_{12n}^{(z)}(-q^{TM}) \quad (\text{B.8})$$

### Indirect field components, waveguide II $z > 0$

$$e_{22n}^{(z)}(-q^{TM}) = -\frac{ce_{2n}(-q^{TM}, \phi) Ce_{2n}(-q^{TM}, \mu)}{Ce_{2n}(-q^{TM}, \mu_2)} Fek_{2n}(-q^{TM}, \mu_2) \quad (\text{B.9})$$

$$h_{22n}^{(z)}(-q^{TM}) = 0 \quad (\text{B.10})$$

$$\mathbf{e}_{2\mathbf{2n}}^{(t)}(-q^{TM}) = -\frac{jk_z^{TM}F^2}{-4q^{TM}}\nabla_t e_{2\mathbf{2n}}^{(z)}(-q^{TM}) \quad (\text{B.11})$$

$$\mathbf{h}_{2\mathbf{2n}}^{(t)}(-q^{TM}) = -\frac{jk_0F^2}{-4q^{TM}}\hat{\mathbf{z}}\times\nabla_t e_{2\mathbf{2n}}^{(z)}(-q^{TM}) \quad (\text{B.12})$$

## Appendix C

# Scattered field components

Waveguide I,  $z < 0$  (TM modes)

$$e_{2n}^{(z)} \left( q_{12n,m}^{TM} \right) = c e_{2n} \left( q_{12n,m}^{TM} \right) C e_{2n} \left( q_{12n,m}^{TM} \right) \quad (C.1)$$

$$h_{2n}^{(z)} \left( q_{12n,m}^{TM} \right) = 0 \quad (C.2)$$

$$\mathbf{e}_{2\mathbf{n}}^{(t)} \left( q_{12n,m}^{TM} \right) = \frac{jk_{z1,2n,m}^E F^2}{4q_{12n,m}^{TM}} \nabla_t e_{2n}^{(z)} \left( q_{12n,m}^{TM} \right) \quad (C.3)$$

$$\mathbf{h}_{2\mathbf{n}}^{(t)} \left( q_{12n,m}^{TM} \right) = -\frac{jk_0 F^2}{4q_{12n,m}^{TM} Z_0} \hat{\mathbf{z}} \times \nabla_t e_{2n}^{(z)} \left( q_{12n,m}^{TM} \right) \quad (C.4)$$

Waveguide II,  $z > 0$  (TM modes)

$$e_{2n}^{(z)} \left( q_{22n,m}^{TM} \right) = c e_{2n} \left( q_{22n,m}^{TM} \right) C e_{2n} \left( q_{22n,m}^{TM} \right) \quad (C.5)$$

$$h_{2n}^{(z)} \left( q_{22n,m}^{TM} \right) = 0 \quad (C.6)$$

$$\mathbf{e}_{2\mathbf{n}}^{(t)} \left( q_{22n,m}^{TM} \right) = -\frac{jk_{z2,2n,m}^{TM} F^2}{4q_{22n,m}^{TM}} \nabla_t e_{2n}^{(z)} \left( q_{22n,m}^{TM} \right) \quad (C.7)$$

$$\mathbf{h}_{2\mathbf{n}}^{(t)} \left( q_{22n,m}^{TM} \right) = -\frac{jk_0 F^2}{4q_{22n,m}^{TM} Z_0} \hat{\mathbf{z}} \times \nabla_t e_{2n}^{(z)} \left( q_{22n,m}^{TM} \right) \quad (C.8)$$

Waveguide I,  $z < 0$  (TE modes)

$$e_{2n+2}^{(z)} \left( q_{12n+2,m}^{TE} \right) = 0 \quad (C.9)$$

$$h_{2n+2}^{(z)} \left( q_{12n+2,m}^{TE} \right) = s e_{2n+2} \left( q_{12n+2,m}^{TE} \right) S e_{2n+2} \left( q_{12n+2,m}^{TE} \right) \quad (C.10)$$

$$\mathbf{e}_{2\mathbf{n}+2}^{(t)} \left( q_{12n+2,m}^{TE} \right) = \frac{jk_0 F^2 Z_0}{4q_{12n+2,m}^{TE}} \hat{\mathbf{z}} \times \nabla_t h_{2n+2}^{(z)} \left( q_{12n+2,m}^{TE} \right) \quad (\text{C.11})$$

$$\mathbf{h}_{2\mathbf{n}+2}^{(t)} \left( q_{12n+2,m}^{TE} \right) = \frac{jk_{z_1,2n+2,m}^{TE} F^2}{4q_{12n+2,m}^{TE}} \nabla_t h_{2n+2}^{(z)} \left( q_{12n+2,m}^{TE} \right) \quad (\text{C.12})$$

### Waveguide II, $z > 0$ (TE modes)

$$e_{2n+2}^{(z)} \left( q_{22n+2,m}^{TE} \right) = 0 \quad (\text{C.13})$$

$$h_{2n+2}^{(z)} \left( q_{22n+2,m}^{TE} \right) = s e_{2n+2} \left( q_{22n+2,m}^{TE} \right) S e_{2n+2} \left( q_{22n+2,m}^{TE} \right) \quad (\text{C.14})$$

$$\mathbf{e}_{2\mathbf{n}+2}^{(t)} \left( q_{22n+2,m}^{TE} \right) = \frac{jk_0 F^2 Z_0}{4q_{22n+2,m}^{TE}} \hat{\mathbf{z}} \times \nabla_t h_{2n+2}^{(z)} \left( q_{22n+2,m}^{TE} \right) \quad (\text{C.15})$$

$$\mathbf{h}_{2\mathbf{n}+2}^{(t)} \left( q_{22n+2,m}^{TE} \right) = -\frac{jk_{z_2,2n+2,m}^{TE} F^2}{4q_{22n+2,m}^{TE}} \nabla_t h_{2n+2}^{(z)} \left( q_{22n+2,m}^{TE} \right) \quad (\text{C.16})$$

## *Acknowledgements*

At the end of my work it is a pleasure to thank those who made this thesis possible.

This journey has begun at the end of 2011, when I was just graduated and resulted winner of La Sapienza PhD scholarship. I was just starting to look for a PhD thesis project when Mauro Migliorati asked me to join him in his research activity on impedances and collective effects at CERN. I owe my deepest gratitude to Mauro for this great opportunity, for the trust he placed in me, for his careful and patient guidance. Mauro became more of a mentor and a friend to me, than a professor.

I would like to thank Benoit Salvant, my CERN supervisor, for the time he devoted to me with patience and accessibility and for the knowledge he tried to convey to me. I learned a lot from him and his guide was essential for my thesis activity. It was a pleasure to work and interact with him.

I can never be thankful enough to Prof. Vittorio Vaccaro for giving me the possibility to profit from his valuable experience and intuition. He introduced me to the complex world of Mathieu functions, he taught me how to manipulate Maxwell equations, sharing with me his multidisciplinary knowledge, encouraging and inspiring me with his kind words.

I am indebted with my university coordinator, Prof. Luigi Palumbo, for always making himself available with support and valuable advices.

I am also grateful to Simone Gilardoni for supporting and guiding my activity and for sharing with me his deep knowledge of the PS machine. He gave me the possibility of participating in measurements, surveys, workshops where I could learn and share my work. He always listened my ideas and suggestions and I have always appreciated his honesty and openness.

I would also like to thank Elias Metral, for giving me the possibility to join the HSC section. I have always appreciated his strong team attitude, and his great experience and suggestions were invaluable for my work.

For their kind help and support in my activities involving the PS machine, I would like to thank Heiko Damerou, Michele Morvillo, Massimo Giovannozzi, Guido Sterbini. They never hesitated in giving me their full support and help when I needed.

For their support in the RF and electromagnetics computation field and for their constant availability I would like to thank Alessandro D'Elia, Giovanni De Michele, Carlo Zannini and Luca Ficcadenti.

I am grateful to all the people who spent their time in the CERN control room with me, in particular Raymond Wasef and the PS operators.

I am also grateful to the CERN Impedance team, where I could share my results and my doubts, always receiving kind and useful feedbacks and support.

A special thanks goes to Nicolò Biancacci. In the past three years his tutoring and encouragement have been essential for the success of my thesis project. During (almost) ten

years of friendship we shared difficulties, concerns about the future, but also professional and personal fulfillments. His enthusiasm in research was contagious and motivational for me and I really wish our path would cross again in the future.

I would like to warmly thank Chiara, Cinzia, Alessia, Vincenzo, Vasim for their friendship and for the nice moments we have spent together.

Thanks to Pietro, for accompanying me in this journey we started together three years ago, and for supporting me in my everyday life.

To close, thanks to my parents, for infusing in me the love and passion for science and research.

# Bibliography

- [1] V. G. Vaccaro. Longitudinal instability of a coasting beam above transition, due to the action of lumped discontinuities. Technical Report CERN-ISR-RF-66-35. ISR-RF-66-35, CERN, Geneva, Nov 1966.
- [2] L. Palumbo, V.G. Vaccaro, and M. Zobov. Wake fields and impedance. (LNF-94-041-P), Sep 1994.
- [3] R. L. Gluckstern. *Analytic methods for calculating coupling impedances*. CERN, Geneva, 2000.
- [4] N. Biancacci. *Improved techniques of impedance calculation and localization in particle accelerators*. PhD thesis, Rome, La Sapienza, Apr 2014.
- [5] A. Hofmann. Beam instabilities. Technical report, 2005.
- [6] S. Gilardoni and D. Manglunki, editors. *Fifty years of the CERN Proton Synchrotron*. CERN, 2011.
- [7] M. J. Barnes et al. Injection and extraction magnets: septa. . CERN Accelerator School CAS 2009, Bruges, 16-25 June 2009.
- [8] M. J. Barnes et al. Injection and extraction magnets: kicker magnets. . CERN Accelerator School CAS 2009, Bruges, 16-25 June 2009.
- [9] M.J. Barnes, O.E. Berrig, A. Beuret, J. Borburgh, P. Bourquin, et al. The CERN PS multi-turn extraction based on beam splitting in stable islands of transverse phase space: Design report. (CERN-2006-011), 2006.
- [10] R. Garoby. LHC proton beams in the PS Complex: status and plans. 2004.
- [11] R. Garoby, D. G. Grier, et al. The PS 40 MHz bunching cavity. (CERN-PS-97-039-RF), Jun 1997.
- [12] D. G. Grier, E. Jensen, et al. The PS 80 MHz cavities. (CERN-PS-98-021-RF):3 p, Jun 1998.

- 
- [13] Grier D. The PS 10 MHz cavity and power amplifier. Technical report, CERN PS/RF Note, 2002-073.
- [14] D. Boussard. The PS 200 MHz RF system: present situation and future prospects. Technical Report CERN-SPS-ARF-78-6, 1978.
- [15] H. Damerau, M. Morvillo, et al. Controlled longitudinal emittance blow-up in the CERN PS. In *Proceedings of PAC07, Albuquerque, New Mexico, USA*, 2007.
- [16] M. Van Rooij, J. P. Bertuzzi, M. Brouet, A. Burlet, C. Burnside, and A. and Petty L. Gavaggio, R. and Oncet. The Vacuum Upgrade of the CERN PS and PS Booster. 1995.
- [17] M. Migliorati, H. Damerau, S. Gilardoni, S. Hancock, L. Palumbo, and S. Persichelli. Beam-Wall Interaction in the CERN Proton Synchrotron for LHC Upgrade. *Phys. Rev. Spec. Top. Accel. Beams*, 16:031001. 22 p, Oct 2012.
- [18] R. Cappi. RF bypass on the proton synchrotron vacuum chamber flanges. (CERN-PS-89-22-PA), 1989.
- [19] A Faugier. Les brides de chambre a vide du PS. Technical Report CERN-PS-OP-NOTE-77-4, 1977.
- [20] A. Faltens and H. Umstatter. Longitudinal coupling impedances at insulated PS vacuum chamber flanges. Technical Report CERN-MPS-LIN-Note-74-5, 1974.
- [21] J. Bento, F. Caspers, and A. Mostacci. Coupling impedance measurements with the coaxial wire method on the CPS RF bypass. Technical Report CERN-PS-RF-NOTE-2002-217, 2002.
- [22] M. Mathieu. Le raccord a vide demontables du SPS. Technical report, CERN SPS/SME/76-3, 1976.
- [23] R. Garoby, H. Damerau, S. Gilardoni, B. Goddard, K. Hanke, A. Lombardi, D. Manglunki, M. Meddahi, B. Mikulec, E. Ponce, L. and Shaposhnikova, R. Steerenberg, and M. Vretenar. Status and Plans for the Upgrade of the LHC Injectors. (CERN-ATS-2013-059), May 2013.
- [24] S. Gilardoni, S. Bart Pedersen, C. Bertone, N. Biancacci, A. Blas, S. Damjanovic, D. Bodart, J. Borburgh, P. Chiggiato, H. Damerau, J. Devine, T. Dobers, M. Paoluzzi, S. Persichelli, et al. The PS Upgrade Program: Recent Advances. (CERN-ACC-2013-0162), May 2013.
- [25] <http://hilumilhc.web.cern.ch/>.

- [26] O. Bruning, P. Collier, P. Lebrun, S. Myers, R. Ostojic, J. Poole, and P. Proudlock. *LHC Design Report, Volume I*. CERN, Geneva, 2004.
- [27] G. Apollinari, O. Bruning, and L. Rossi. High Luminosity LHC Project Description. Technical Report CERN-ACC-2014-0321, CERN, Geneva, Dec 2014.
- [28] S. Aumon. *High Intensity Beam Issues in the CERN Proton Synchrotron*. PhD thesis, EPFL, Lausanne, May 2012.
- [29] F. J. Sacherer. Transverse bunched-beam instabilities. Technical Report CERN-PS-BR-76-21, CERN, Geneva, Nov 1976.
- [30] M. Gasior and R. Jones. The principle and first results of betatron tune measurement by direct diode detection. Technical Report LHC-Project-Report-853. CERN-LHC-Project-Report-853, CERN, Geneva, Aug 2005.
- [31] A.W. Chao. *Physics of Collective Beam Instabilities in High Energy Accelerators*. JohnWiley and Sons, 1993.
- [32] A. Huschauer. *Working point and resonance studies at the CERN Proton Synchrotron*. PhD thesis, Vienna, Tech. U., Sep 2012.
- [33] S. Persichelli, M. Migliorati, N. Biancacci, S. Gilardoni, E. Metral, and B. Salvant. The Proton Synchrotron transverse impedance model. Technical Report CERN-ACC-2014-0114, CERN, Geneva, Jun 2014.
- [34] N. Mounet. News on the 2D wall impedance theory. In *HB 2010, Morschach, Switzerland*, 2010.
- [35] <https://www.cst.com>.
- [36] H. Tsutsui. Longitudinal impedances of some simplified ferrite kicker magnet models. (CERN-SL-2000-050-AP), Jun 2000.
- [37] C. Zannini, N. Mounet, B. Salvant, E. Metral, and G. Rumolo. Electromagnetic simulations of simple models of ferrite loaded kickers. (CERN-BE-Note-2010-006), Jun 2010.
- [38] Y. H. Chin. User's guide for ABCI version 8.7: Azimuthal Beam Cavity Interaction. Technical Report CERN-SL-94-02-AP, CERN, Geneva, Feb 1994.
- [39] R. Losito. 80 MHz cavity. Technical report, CERN PS/RF Note 96-14, 1996.
- [40] D. Boussard et al. Observation of microwave longitudinal instabilities in the CPS. In *Proc. of PAC79*, page 3568, 1979.

- [41] D. Boussard et al. Mesures d'impedance longitudinale de chambre a vide au PS. CERN PS-OP-LR/Note 80-16, CERN, Geneva, Switzerland, 1980.
- [42] H. Damerau, S. Gilardoni, S. Hancock, M. Migliorati, L. Palumbo, and S. Persichelli. Evaluation of the broadband longitudinal impedance of the CERN PS. (CERN-ATS-Note-2012-064 MD), Aug 2012.
- [43] J. L. Laclare. Bunched beam coherent instabilities. 1987.
- [44] A. Chao and M. Tigner. *Handbook of Accelerator Physics and Engineering*. World Scientific, Singapore, 1999.
- [45] S. Persichelli, M. Migliorati, O. Berrig, J. Herbst, J. Kuczerowski, M. Giovannozzi, and B. Salvant. Impedance studies of the dummy septum for CERN PS multi-turn extraction. Technical Report CERN-ACC-2014-0118, CERN, Geneva, Jun 2014.
- [46] C. Bertone, J. Borburgh, S. Persichelli, et al. Studies and implementation of the PS dummy septum to mitigate irradiation of magnetic septum in straight section 16. Technical Report CERN-ACC-2014-0043, CERN, Geneva, Apr 2014.
- [47] S. Persichelli. Trapped modes in a dummy extraction septum for CERN Proton Synchrotron. *Il Nuovo Cimento*, 4:365–372, Sep 2014.
- [48] [http://www.3ds.com/products\\_services/catia/](http://www.3ds.com/products_services/catia/).
- [49] C. Zannini, K. Li, and G. Rumolo. Effects of an Asymmetric Chamber on the Beam Coupling Impedance. (CERN-ATS-2012-081), May 2012.
- [50] H. Damerau, S. Hancock, et al. Longitudinal Coupled-Bunch Instabilities in the CERN PS. (CERN-AB-2007-051):4 p, 2007.
- [51] H. Damerau, Hancock, et al. Longitudinal Coupled-Bunch Oscillation Studies in the CERN PS. (CERN-ACC-2013-0205):3 p, May 2013.
- [52] S. Bartalucci et al. Analysis of methods for controlling multibunch instabilities in DAFNE. *Part. Accel.*, 48(LNF-93-067-P):213–237. 27 p, Oct 1993.
- [53] B. Salvant, O. Aberle, G. Arduini, R. Assmann, V. Baglin, M. Barnes, W. Bartmann, P. Baudrenghien, O. Berrig, S. Persichelli, et al. Update on Beam Induced RF Heating in the LHC. (CERN-ACC-2013-0041), May 2013.
- [54] A. Mostacci, L. Palumbo, B. Spataro, and F. Caspers. RF coupling impedance measurements versus simulations. 2005.
- [55] M. Paoluzzi, M. Haase, et al. Studies on a wideband, solid-state driven RF system for the CERN PS Booster. (CERN-ATS-2012-113):3 p, May 2012.

- [56] M. Paoluzzi and H. Damerau. Design of the PS longitudinal damper. Sep 2013.
- [57] <http://www.hitachimetals.com/product/amorphous/>.
- [58] S. Persichelli, M. Migliorati, M. Paoluzzi, and B. Salvant. Impedance studies for the PS Finemet loaded longitudinal damper. Technical Report CERN-ACC-2014-0113, CERN, Geneva, Jun 2014.
- [59] S. Persichelli, M. Paoluzzi, M. Migliorati, and B. Salvant. Finemet cavity impedance studies. (CERN-ACC-NOTE-2013-0033), Nov 2013.
- [60] <https://indico.cern.ch/event/332863/contribution/1/material/slides/1.pdf>.
- [61] N. King-Yuen. Impedances of stripline beam-position monitors. *Particle Accelerators*, 23:93–102, 1998.
- [62] M. Abramowitz and I. Stegun. *Handbook of Mathematical Functions with Formulas, Graphs, and Mathematical Tables*. Dover, New York, 1964.
- [63] J.C. Wiltse. *Graphs and tables of the Mathieu functions and their first derivatives*. AuthorHouse, Bloomington, IN, 2012.
- [64] M. Bibby and A. Peterson. *Accurate Computation of Mathieu Functions*. Morgan & Claypool Publishers, 2013.
- [65] H. Wilson and R. Scharstein. Computing elliptic membrane high frequencies by Mathieu and Galerkin methods. *Journal of Engineering Mathematics*, 57(1):41–55, 2007.
- [66] S. Zhang and Y. Shen. Eigenmode sequence for an elliptical waveguide with arbitrary ellipticity. *Microwave Theory and Techniques, IEEE Transactions on*, 43(1):227–230, 1995.
- [67] J. Gutierrez-Vega et al. Mathieu functions, a visual approach. *American Journal of Physics*, 71(3):233, 2003.
- [68] N.W. McLachlan. *Theory and application of Mathieu functions*. Clarendon Press, Oxford, 1951.
- [69] J. Gutierrez-Vega et al. Free oscillations in an elliptic membrane. *Rev. Mex. Fis.*, 45(6):613, 1999.
- [70] D.A. Goldberg, L.J. Laslett, and R.A. Rimmer. Modes of elliptical waveguides; a correction. Mar 1990.
- [71] J.P. Kinzer and I.G. Wilson. Some results on cylindrical cavity resonators. Technical report, BELL system technical Journal, 1947.

- 
- [72] B. Chen, Morris. P., and J. Zhou. Visualization of special eigenmode shape of a vibrating elliptical membrane. *SIAM Review*, 36(3):453–469, 1994.
- [73] A. Mostacci. *Beam-Wall interaction in the LHC liner*. PhD thesis, 2001.
- [74] N. Mounet. *The LHC Transverse Coupled-Bunch Instability*. PhD thesis, EPFL, Lausanne, Mar 2012.
- [75] L. Palumbo, V. Vaccaro, and G. Wustefeld. Coupling impedance in a circular particle accelerator, a particular case: Circular beam, elliptic chamber. *IEEE Transactions on Nuclear Science*, 31(4):1011 – 1020, 1984.
- [76] D. Davino et al. Longitudinal coupling impedance of an abrupt junction in a vacuum chamber. *Il Nuovo Cimento*, 112(A)(2):1401–1429, 1999.
- [77] S. A. Kheifets and S. A. Heifets. Radiation of a charge in a perfectly conducting cylindrical pipe with a jump in its cross section. (SLAC-PUB-3965):36 p, May 1986.